NUMERICAL AND EXPERIMENTAL INVESTIGATION OF PITCHING/PLUNGING AIRFOILS IN HOVER

A THESIS SUBMITTED TO
THE GRADUATE SCHOOL OF NATURAL AND APPLIED SCIENCES
OF
MIDDLE EAST TECHNICAL UNIVERSITY

BY

HASAN HIZLI

IN PARTIAL FULFILLMENT OF THE REQUIREMENTS
FOR
THE DEGREE OF MASTER OF SCIENCE
IN
AEROSPACE ENGINEERING

DECEMBER 2012

Approval of the thesis:

NUMERICAL AND EXPERIMENTAL INVESTIGATION OF PITCHING/PLUNGING AIRFOILS IN HOVER

submitted by **HASAN HIZLI** in partial fulfillment of the requirements for the degree of **Master of Science in Aerospace Engineering Department, Middle East Technical University** by,

Prof. Dr. Canan ÖZGEN _____
Dean, Graduate School of **Natural and Applied Sciences**

Prof. Dr. Ozan TEKİNALP _____
Head of Department, **Aerospace Engineering**

Assoc. Prof. Dr. Dilek Funda KURTULUŞ _____
Supervisor, **Aerospace Engineering Dept., METU**

Examining Committee Members:

Prof. Dr. İsmail Hakkı TUNCER _____
Aerospace Engineering Dept., METU

Assoc. Prof. Dr. Dilek Funda KURTULUŞ _____
Aerospace Engineering Dept., METU

Assoc. Prof. Dr. Oğuz UZOL _____
Aerospace Engineering Dept., METU

Asst. Prof. Dr. Kürşad Melih GÜLEREN _____
Dept. of Aeronautical Engineering, UTAA

Asst. Prof. Dr. Mustafa KAYA _____
Dept. of Flight Training, UTAA

Date: 10.12.2012

I hereby declare that all information in this document has been obtained and presented in accordance with academic rules and ethical conduct. I also declare that, as required by these rules and conduct, I have fully cited and referenced all material and results that are not original to this work.

Name, Last Name : Hasan HIZLI

Signature :

ABSTRACT

NUMERICAL AND EXPERIMENTAL INVESTIGATION OF PITCHING/PLUNGING AIRFOILS IN HOVER

Hızlı, Hasan
M.Sc., Department of Aerospace Engineering
Supervisor: Assoc. Prof. Dr. Dilek Funda Kurtuluş

December 2012, 132 pages

In this thesis, results of the numerical and experimental study corresponding to four airfoils, namely SD7003, NACA0012, 10% thick elliptical, 10% thick flat plate, undergoing sinusoidal pure pitch, pure plunge and combined pitch-plunge types of hovering motion are presented. A number of cases are investigated consisting of different pitching and plunging amplitudes. The study aims to provide a better understanding of the aerodynamics phenomena and the vortex topology of flapping wings in motion for application to micro air vehicle (MAV) designs, to investigate the effect of pitching and plunging amplitudes on the different modes of hovering motion and to compare the numerical and experimental results for validation of the newly built experimental setup with the numerical simulations by means of the instantaneous flow topologies. The unsteady, incompressible Navier-Stokes equations are solved for the extensive numerical simulation of the flow field around the airfoils whereas the instantaneous velocity field data of the flow are acquired by the Particle Image Velocimetry (PIV) measurements. An agreement between the numerical and experimental results of the investigated test cases is observed in terms

of the instantaneous vortex structure of the flow. Among the studied cases, the highest mean lift coefficient is obtained from pitching-plunging ($\alpha_a=30^o$, $x_a=0.01\ m$) SD7003 airfoil while the lowest is obtained from purely plunging ($x_a=0.02\ m$) 10% thick flat plate airfoil. Moreover, pitching-plunging ($\alpha_a=30^o$, $x_a=0.02\ m$) SD7003 airfoil gives the lowest mean drag coefficient whereas pitching-plunging ($\alpha_a=45^o$, $x_a=0.01\ m$) 10% thick elliptical airfoil gives the highest.

Keywords: Flapping Airfoils, Hovering, Micro Air Vehicles, Particle Image Velocimetry (PIV).

ÖZ

HAVADA ASILI KONUMDA YUNUSLAMA/DALMA HAREKETİ YAPAN KANAT KESİTLERİNİN SAYISAL VE DENEYSEL OLARAK İNCELENMESİ

Hızlı, Hasan

Yüksek Lisans, Havacılık ve Uzay Mühendisliği Bölümü

Tez Yöneticisi: Doç. Dr. Dilek Funda Kurtuluş

Aralık 2012, 132 sayfa

Bu tezde, sinüs biçimli sade yunuslama, sade dalma ve kombine yunuslama-dalma türlerinde havada asılı kalma hareketi yapan dört kanat kesitine, yani SD7003, NACA0012, %10 kalınlıkta eliptik ve %10 kalınlıkta düz plakaya ait sayısal ve deneysel çalışmanın sonuçları sunulmaktadır. Farklı yunuslama ve dalma genliklerini içeren birçok durum incelenmiştir. Bu çalışma, mikro hava araçlarının (MHA) tasarımına uygulanması için hareket halindeki çırpan kanatların aerodinamiğinin ve girdap topolojisinin daha iyi anlaşılmasını, yunuslama ve dalma genliklerinin havada asılı kalma hareketinin farklı modları üzerindeki etkilerinin incelenmesini ve yeni kurulan deney düzeneğinin sayısal benzetimler ile doğrulanması için sayısal ve deneysel sonuçları anlık akış topolojileri aracılığıyla karşılaştırmayı amaçlamaktadır. Kanat kesitlerinin etrafındaki akış alanının sayısal modellemesi için daimi olmayan, sıkıştırılamaz Navier-Stokes denklemleri çözülürken akışın anlık hız alanı verileri ise Parçacık İmge Hızölçer (PİH) ölçümleri ile elde edilmiştir. Akışın anlık girdap yapısı açısından incelenen durumların sayısal ve deneysel sonuçları arasında bir uyuşma olduğu gözlemleniştir. İncelenen durumlar arasında, en düşük ortalama kaldırma

kuvveti katsayısı sade dalma hareketi ($x_a=0.02\ m$) yapan %10 kalınlıkta düz plaka kanat kesitinden elde edilirken, en yükseği ise yunuslama-dalma hareketi ($\alpha_a=30^o$, $x_a=0.01\ m$) yapan SD7003 kanat kesitinden elde edilmiştir. Bunun yanında, yunuslama-dalma hareketi ($\alpha_a=30^o$, $x_a=0.02\ m$) yapan SD7003 kanat kesiti en düşük ortalama sürtünme kuvveti katsayısını verirken, yunuslama-dalma hareketi ($\alpha_a=45^o$, $x_a=0.01\ m$) yapan %10 kalınlıkta eliptik kanat kesiti ise en yükseğini vermiştir.

Anahtar Kelimeler: Çırpan Kanat Kesitleri, Havada Asılı Kalma, Mikro Hava Araçları, Parçacık İmge Hızölçer (PİH).

to the proprietor of everything...

ACKNOWLEDGMENTS

I would like to express my deepest appreciation to my supervisor Assoc. Prof. Dr. Dilek Funda Kurtuluş for all the opportunities she provided to me to realize this study. I am extremely grateful and indebted to her for her expert, sincere and valuable guidance, criticism and encouragements extended to me through the research. I owe too much to her.

I would like to specially thank to jury members Prof. Dr. İsmail Hakkı Tuncer, Assoc. Prof. Dr. Oğuz Uzol, Asst. Prof. Dr. Kürşad Melih Güleren and Asst. Prof. Dr. Mustafa Kaya for reviewing my thesis.

I am indebted to the technical assistance of Oğuz Durmaz. I am grateful to Erkan Günaydınoğlu and in particular to Çağrı Gezgüç for sharing their knowledge about CFD tricks with me. I would also like to place on record my sense of gratitude to all my precious friends who, in one or another way, influenced on my decisions and have lent their helping hands to me during the hard times.

Last, but not least, I owe my sincere and earnest thankfulness to my mother for her unceasing encouragement and support. If she did not support me in all stages of my life, I would not be here. Thank God that I have her. I also thank to my father.

This thesis was supported by TÜBİTAK 105M230 Career Project.

TABLE OF CONTENTS

LIST OF TABLES

TABLES

LIST OF FIGURES

FIGURES

NOMENCLATURE

ABBREVIATIONS

2-D	Two-Dimensional
3-D	Three-Dimensional
BC	Boundary Condition
CCW	Counterclockwise
CFD	Computational Fluid Dynamics
CW	Clockwise
LDV	Laser Doppler Anemometry
LE	Leading Edge
LEV	Leading Edge Vortex
MAV	Micro Air Vehicle
PIV	Particle Image Velocimetry
TE	Trailing Edge
TEV	Trailing Edge Vortex

SYMBOLS

c	Chord length [m]
C_L	Lift coefficient per unit span
C_D	Drag coefficient per unit span
C_M	Moment coefficient per unit span
C_p	Pressure coefficient
f	Frequency of the motion [Hz]
k	Reduced frequency
Re	Reynolds number
t	Time variable [s]
T	Period of the motion [s]

t/T	Non-dimensional time variable
U_{ref}	Reference velocity [m/s]
$u(t)$	Axial velocity in the horizontal direction [m/s]
$v(t)$	Axial velocity in the vertical direction [m/s]
w	Angular frequency ($w = 2\pi f$)
x_a	Horizontal plunging amplitude [m]
y_a	Vertical plunging amplitude [m]

GREEK LETTERS

α_a	Pitching amplitude [radian]
μ	Dynamic viscosity of the fluid [kg/m·s]
υ	Kinematic viscosity of the fluid [m^2/s]
ω	Vorticity [1/s]
$\omega(t)$	Angular velocity [radian/s]

CHAPTER 1

INTRODUCTION

1.1 Background Information

For thousands of years, flight of different species of insects and birds fascinates the human being with the magic behind it [1]. It is believed by a great number of scientists and biologists that flying mechanically with flapping wings to create lift and thrust for various aims like maneuvering and transportation is very complex and hard to achieve. To give an example, when the maximum roll rate of a typical aerobatic aircraft is about 420 degrees per second, a barn swallow can reach a roll rate of 5000 degrees per second [2]. However, it is not impossible to fly with flapping wings at all. In order to be able to create vehicles flying or swimming as professional as animals, there are many ongoing researches, a great majority of them are for military purposes, related to the investigation of different kinds of flapping motion, mainly forward flapping flight and hovering, by means of extensive numerical and experimental studies nowadays ([3] - [5]).

Being technologically and scientifically developed, engineers have started to understand the secrets behind the flapping motion of natural flyers and then to design and build small flying vehicles imitating the nature for various aims. Recently, Micro Air Vehicles (MAVs), Autonomous Underwater Vehicles (AUVs) and more artily, Nano Air Vehicles (NAVs) are being developed by numerical means and then being tested in an experimental environment in order to achieve the aims of flapping flight that animals easily do and by this means to meet mainly the military needs such as

surveillance and reconnaissance [6]. These vehicles may take the advantages of flapping flight in order to obtain better performances compared to the traditional methods [7].

MAVs, which are defined as small flying air vehicles having a maximum dimension of 15 cm and a maximum weight of 90 grams by the Defense Advanced Research Projects Agency (DARPA) [8], are the ones that excite the substantial attention of engineering community in this field. There is an increasing need of MAVs, especially for military applications, due to the advantages they have over conventional aircrafts such as high maneuverability, high efficiency, acquiring real time data, low radar cross-section area, low noise level, forestry and wildlife surveying and so on ([8], [9]).

MAVs may have fixed, rotary and flapping wing configurations [10]. But flapping wing MAVs are believed to have better aerodynamical and propulsive performances than fixed and rotary wing MAVs at low Reynolds number flights [12]. At low Reynolds numbers (typically in the order of 10^3 to 10^5), the aerodynamic performance of fixed wing MAVs drops dramatically due to high viscous drag and flow separation, causes loss of lift [11]. Flapping wing MAVs try to solve this problem occurring at low Reynolds numbers by getting the advantage of highly vertical flow fields generated at the leading and trailing edges of the wings to form low pressure regions that may be used for lift and thrust generation [13]. Apparently, there is one more disadvantage of fixed wing MAVs: hovering. Due to the structural limitations, fixed wing MAVs cannot hover, which is a significant problem especially in a confined space [14]. Flapping wing MAVs have also advantages over rotary wing MAVs in term of maneuverability and near-wall locomotion [10].

Apart from the studies about application of flapping wings to design of MAVs, there are many areas of research about flapping wings such as aerodynamic flutter, unsteady aerodynamics phenomena of cyclically flapping helicopter rotor blades, blade-vortex interaction for preventing noise in rotorcrafts, decay of wake vortices for minimizing their hazards on aircrafts and so on [7].

1.2 Present Approach

The current study is based on the numerical simulation and experimental visualization of constant frequency, sinusoidal pure pitch, pure plunge and combined pitch-plunge motions of four different airfoils, SD7003, NACA0012, 10% thick elliptical and 10% thick flat plate, in hover, i.e. without any free stream velocity. During the study, instead of using a complex and sophisticated model, a simplified model is used due to the need to obtain quicker results and the limitations of the experimental setup. The numerical and experimental studies are mainly performed in 2-D for all cases considered. However, 3-D numerical simulations are also performed for the baseline test cases in order to investigate the three-dimensional effects for these cases.

By this means, the unsteady, incompressible and constant property Navier-Stokes equations are solved for the numerical simulation of the studied cases. Experimental visualization of each test case is done by Particle Image Velocimetry (PIV) method. The results obtained from these two studies are then analyzed, interpreted and compared with each other in order to explain the observed phenomena.

1.3 Major Objectives

The major objectives of the present study are:

- to investigate the unsteady flapping motion of four different airfoils, namely SD7003, NACA0012, 10% thick elliptical and 10% thick flat plate, undergoing sinusoidal pure pitch, pure plunge and combined pitch-plunge motions in hover in order to provide a better understanding of the aerodynamics phenomena and the vortex topology of these unsteady flapping motions by means of the numerical and experimental studies;

- to investigate the effects of pitching and plunging amplitudes on the constant frequency sinusoidal hovering motions of previously mentioned airfoils;

- to investigate the effects of domain resolution difference between the CFD simulations and PIV visualizations and three-dimensional effects;

- to explore the hovering cases from which the highest mean lift coefficient and the lowest mean drag coefficient are obtained;

- to build an experimental setup in order to investigate the low frequency flapping motion studies in hover mode for different test cases; and

- to validate the experimental setup with the numerical simulations, the methodology followed for which have been verified previously within the scope of the studies of NATO AVT-149 - Micro Air Vehicle Unsteady Aerodynamics Task Group ([5], [14]).

1.4 Outline of the Thesis

In order to meet the objectives stated above, this thesis is divided into six chapters. In Chapter I, some background information related to the concerned topic and the major objectives of this thesis are given. Chapter II reviews some previous works corresponding to the aerodynamics of flapping wings. In chapter III, the detailed explanation of the numerical methodology followed is given. Also in this chapter, kinematics of the hovering motions under investigation and the test cases investigated in the present study are given. Chapter IV includes the description of the experimental setup, the description of the Particle Image Velocimetry (PIV) measurements and the experimental procedure carried out. Chapter V discusses all the results obtained from the numerical simulations and PIV measurements of the baseline test cases. Chapter VI presents the general conclusions and future recommendations that could be done further on this study.

CHAPTER 2

LITERATURE SURVEY

This chapter is devoted to the review of some of the studies performed about the flapping wing motion in recent years by means of numerical, analytical and experimental approaches. The literature survey conducted is aimed to provide a scientific basis for understanding the aerodynamics of the flapping wing motion. To achieve this aim, the present chapter is divided into three main sections. In the first section, the studies corresponding to numerical and analytical approaches are given. Then, the studies by means of experimental approaches are given in the second section. And in the last section, some of the comparative studies corresponding to the comparison of the numerical and experimental approaches are presented.

2.1 Numerical and Analytical Approaches

The available literature has a great variety of documented research about the numerical and analytical study of flapping motion for various aims. Some of these studies are discussed in this section.

The two independent studies of Knoller [15] and Betz [16] are known to be the earliest studies related to the flapping flight. They pointed out that the flapping motion of an airfoil in forward flight generates an effective angle of attack resulting to the airfoil to generate an aerodynamic force having lift, drag and thrust components. This flow phenomenon is known as the Knoller-Betz effect. After a decade, Katzmayr [17] experimentally verified this effect by performing a set of

wind tunnel tests in a sinusoidally oscillating free stream to measure the thrust generated by the airfoil in motion. In those years, Birnbaum [18] developed a solution methodology for the incompressible flow past flapping airfoils and investigate the conditions resulting to flutter and thrust generation. He also defined the similarity parameter reduced frequency, defined as the rate of flapping velocity to the free stream velocity, for the first time.

In the following decade, Theodorsen [19] suggested an analytical method to investigate the unsteady lift and moments on oscillating airfoils by making inviscid and incompressible flow assumptions. A few years later, von Kármán and Burgers [20] made the first theoretical explanation of drag and thrust production of plunging airfoils based on the wake vortices.

The advances in science and technology accelerated the researches regarding to the flapping flight. Jones and Platzer [21] numerically studied the flow over single foils using a time-dependent, 2-D panel code coupled with a boundary layer algorithm. They noted that decreasing the reduced frequency and increasing the amplitude of the motion while keeping the Strouhal number constant increases the propulsive efficiency of the flapping motion.

Isogai et al. [22] studied the effect dynamic stall phenomena on the propulsive efficiency and thrust of an airfoil undergoing combined pitch-plunge motion using a Navier-Stokes solver for various cases having different phase differences and reduced frequencies. They obtained the highest propulsive efficiency when the phase difference is 90^o, pitching leads plunging, and the reduced frequency is at an optimum value such that there is no flow separation observed.

Wang [23] numerically studied the flapping motion of a 2-D elliptical wing in forward flight, which simulates the flight of a dragonfly, to select an optimal frequency by solving the vorticity-stream function form of Navier-Stokes equations. As a result, he observed that the optimal frequency obtained was very close to that obtained from the 3-D analysis of Hall et al. [24]. In a following study, Wang [25]

followed the same numerical solution methodology used in his early study to investigate the elliptical airfoil having 12.5% thickness to chord ratio undergoing a figure-of-eight type hovering motion. He concluded that lift enough to support the insect's weight could be produced by 2-D sinusoidal hovering motion of the wing.

Sun and Du [26] studied the lift and power requirements of eight different insect species undergoing a hovering flight numerically by solving the Navier-Stokes equations. They investigated insect's wings whose spans were ranging from 2 mm (fruit fly) to 52 mm (hawkmoth) at Reynolds numbers ranging from 75 to 3850. As a result of the study, they found that a midstroke angle of attack in the range of 25^{o} to 45^{o} is enough to produce a mean lift force equal to the insect's weight.

In another study, the effect of Reynolds number, amplitude of the stroke, midstroke angle of attack, duration of wing rotation and timing of rotation on the force coefficients of a flapping fruit fly wing having flat plate cross section was analyzed by Wu and Sun [27] for Reynolds numbers ranging from 20 to 1800. Wu and Sun [28] also performed 3-D numerical simulations of the bumblebee wings in hovering and forward flight cases in order to investigate the aerodynamic forces and power requirements of them. They observed that at hovering and low-speed forward flight cases, the vertical force was produced during both the upstroke and downstroke and was contributed by wing lift whereas it was produced mainly during the downstroke and was contributed by both wing lift and wing drag at medium and high speed forward flight cases. Moreover, it was observed that the thrust was mainly produced during the upstroke and was contributed by wing drag. It was also concluded that during low to medium forward flight and hovering cases, the power requirements were similar whereas it was relatively large at high speed forward flight case.

Tuncer and Kaya [29] performed a numerical study to show that the flapping airfoils in biplane configuration can produce 20% to 40% more thrust than a single flapping airfoil. In a following study, Kaya et al. [30] performed a study to optimize the flapping motion parameters such as pitching and plunging motion amplitudes, phase shift between two motion and frequency of the motion. They acquired the numerical

solutions by solving the Navier-Stokes equations on moving and deforming overset grids. They observed that the efficiency of biplane configuration could be further increased by flying at Strouhal numbers between 0.17 and 0.25. Tuncer and Kaya [31] also performed a study on the numerical optimization of the amplitude of the flapping motion and the phase shift between pitching and plunging motion for maximizing the thrust and the efficiency of a single flapping airfoil undergoing a sinusoidal combined pitch-plunge motion. They concluded that high values of thrust and efficiency of single flapping airfoils could be obtained by preventing the formation of the large scale Leading Edge Vortices (LEVs).

The effect of vertical translation amplitude and Reynolds number on an SD7003 airfoil undergoing figure-of-eight type hovering motion was studied by Günaydınoğlu and Kurtuluş ([32], [33]). The incompressible, two-dimensional, constant property Navier-Stokes equations were solved for the numerical simulation of the problem. From the results of the numerical simulations performed, it was observed that vortices became stronger as the vertical translation amplitude increased. On the other hand, the increase of the vertical translation amplitude did not make the mean lift coefficient values to increase too. They figured out that the most efficient value of the mean lift coefficient was obtained when the vertical translation amplitude was equal to 0.5.

In their other studies, Günaydınoğlu and Kurtuluş ([34] - [36]) studied the effect of Reynolds number, flapping kinematics, reduced frequency and airfoil geometry on the aerodynamics of a flapping airfoil undergoing pure plunge and combined pitch-plunge motions in forward flight by solving URANS equations on deforming grids. They observed that the lift was mainly produced by the dynamic stall of the airfoil at Reynolds numbers ranging from 10^4 to 6×10^4. They also noted that geometry of the airfoil and reduced frequency affects the strength and duration of the leading edge vortex generated.

2.2 Experimental Approaches

By the help of the technological improvements in science and technology, scientist started to analyze the physics of flapping flight experimentally by using comprehensive techniques such as Particle Image Velocimetry (PIV), Digital Particle Image Velocimetry (DPIV), Laser Doppler Velocimetry (LDV) and so on.

In 1981, Maxworthy [37] investigated the flapping motions of insects in forward flight and in hover conditions. He studied the hovering motion in four categories such as the normal hovering, where the wing stroke plane is nearly horizontal, the clap-fling mechanism, discovered and named by Weis-Fogh [38] and studied in detail by Lighthill [39], inclined wing stroke plane and vertical wing stroke plane, discussed in some detail by Maxworthy [40] and Ellington [41].

Freymuth [42] experimentally studied the combined pitch-plunge motion of a thin flat plate having rounded edges in hover. His main aim was to investigate the thrust generation mechanism of this unsteady motion for Reynolds numbers of between 340 and 1700. He defined three different hovering modes for his study such as normal hovering, water-trading and oblique mode. The experiments were performed by a flow field visualization method so called titanium-tetra-chloride method. He used pitot tubes to measure the thrust coefficient. He concluded that reverse Kármán Vortex Street observed in normal hovering motions was more powerful than other two hovering modes resulting to the production of larger thrust coefficient values.

In another study, Koochesfahani [43] investigated the vortex patterns in the wake of the NACA0012 airfoil undergoing a pitching motion at small amplitudes. Experiments were performed in a low-speed water channel using a single-channel, frequency-shifted LDV system. As a result of this study, it was concluded that frequency, amplitude and shape of the motion significantly affects the structure of the vortices behind the oscillating airfoil. Furthermore, existence of an axial flow

was observed in the core regions of the wake vortices. From the results obtained, it was noticed that the magnitude of this axial flow increases linearly as frequency and amplitude of the motion increases.

The experimental investigation of four important parameters, namely the position of the rotational axis, the rotational speed, the angle of attack of the stroke and the length of the stroke, affecting the aerodynamic performance of a wing profile undergoing a combined pitch-plunge motion was performed by Dickinson [44]. During the experiments, a dynamically scaled aluminum wing model having a thickness of 2%, a span of 0.15 m and a chord of 0.05 m was used in an aquarium filled with 54% sucrose solution. The flow is seeded with aluminum particles and flow phenomenon was recorded by a video tape. In another study, Dickinson et al. [45] performed an experimental study in a mineral oil tank using dynamically scaled 3-D mechanical model of a dragonfly equipped with a 2-D force transducer for the investigation of the interaction of delayed stall, rotational circulation and wake capture at Reynolds number of about 136. Flow visualizations were done by DPIV method. They concluded that rotational circulation and wake capture were responsible for the peaks observed in the rotational lift history.

Anderson et al [46] performed some tests to measure the forces and to visualize the flow around a harmonically oscillating foil at zero average angle of attack. They figured out that optimum thrust was produced at different conditions such as Strouhal numbers of between 0.25 and 0.4, maximum angle of attack values of between 15^{o} and 25^{o}, large amplitudes of heave motion-to-chord ratio.

A comprehensive experimental study on the wake characteristics of sinusoidally plunging NACA0012 airfoil for a range of free stream velocities, frequencies and plunging amplitudes is conducted by Lai and Platzer [47]. In this study, water tunnel flow visualization experiments were performed to measure the stream-wise velocity field downstream of the airfoil for a total of 54 test cases using a single-component LDV system. It is concluded from the dye visualizations performed that when the non-dimensional plunging velocity (kh), the ratio of maximum plunging velocity to

free stream velocity, is less than 0.2, thrust-producing vortex formations are observed behind the airfoil whereas drag-producing vortex formations are observed when it exceeds 0.4. Moreover, an increase in the thrust coefficient is observed as *kh* increases and it becomes positive for values of *kh* greater than 0.36.

2-D biomimetic, flapping-pitching wings were studied by Singh et al. [48] experimentally using laser sheet visualization method. The Reynolds number was about 15000 during the study. A CCD camera was used to capture the instantaneous flow field images. The flow was seeded by vaporizing a mineral oil into a dense fog for the visualization of the test section. Results showed that thrust values of all studied wings decreased at high frequencies.

Schouveiler et al. [49] experimentally studied the propulsive performance of an aquatic propulsion system revealed from the thunniform swimming mode, which tuna and shark perform. It is explained as "*thunniform swimming depends on a large, lunate tail that is joined to the rest of the body via a narrow peduncle. Whilst the tail flicks backwards and forwards, so propelling the animal, the rest of the body hardly moves sideways.*" in Ref. [50]. By this study, they aimed to investigate the effects of Strouhal number and angle of attack on the thrust and the hydro-mechanical efficiency. The flapping motion considered was a combined pitch-plunge motion. The experiments were performed at a fixed value of Reynolds number and of the plunging amplitude for a variety of test cases. They identified a flapping motion parameter range where the thrust and the hydro-mechanical efficiency values are high enough to be used in a propulsion system.

Lehmann et al. [51] performed a set of experiments using a 3-D DPIV system in order to investigate the clap-fling motion of the dynamically scaled mechanical model of small fruit fly in the Reynolds number range of 100 to 200. In a later study, the effect of vertical translation amplitude on the aerodynamic forces and moments was investigated by Lehmann and Pick [52]. The experimental model used was a dynamically scaled electromechanical fruit fly wing performing a clap-fling mechanism. The experiments were performed for 17 different hovering motion cases

differing only in vertical plunging amplitude. The frequency, geometric angle of attack and horizontal plunging amplitude of the motion were identical for each case. They figured out that the pitching moments are independent from the vertical force whereas the mean pitching moment increases nearly 21% with the clap-fling mechanism of the airfoil. It was also concluded that the forces produced does not affect the vertical for augmentation mainly due to the wing rotation at the reversals and wake capture mechanisms.

Instantaneous 3-D velocity field data around a dynamically scaled robotic flapping wing was measured by Poelma et al [53]. They performed 3-D Stereoscopic PIV experiments in a mineral oil tank at a Reynolds number of about 256. Impulsive start and simplified flapping motion cases were studied. Instantaneous 3-D velocity field data around a flapping wing was measured quantitatively for the first time in this study. They used this data then to predict lift and drag values. Flow visualizations were found similar to those reported in recent papers in terms of leading edge vortex structure. Yet, they observed stable pair of counter clockwise rotating vortices instead of a single strand of vorticity as reported in recently published papers.

Tian et al. [54] performed PIV measurements on the flight of lesser short-nosed fruit bats in an enclosed flight cage to understand the kinematics of the motion of these animals during straight and turning flights in a Reynolds number range of 10^4 to 10^5. The flow is seeded using a fog generator. They took high speed stereo images and measured the wake velocity field behind the bat. Results showed that wing motion was quite complex, including a sharp retraction of the wing during the upstroke and a broad sweep of the fully extended wing during the downstroke, at relatively slow flight speeds. Moreover, flight of the bat was oscillatory and in a synchronized fashion with the movement of the wing in both the horizontal and vertical planes.

Daichin et al. [55] experimentally studied the near-wake flow of a NACA0012 airfoil located above the water surface to investigate the effect of free surface on the vortex structure behind the airfoil. Experiments were performed in a small-scale wind/wave tunnel having a test-section of 1.7 m × 0.4 m × 0.4 m for different ride height values

between the airfoil and the water surface at a Reynolds number of about 3.5×10^3. Instantaneous velocity field data were acquired by PIV measurements. The results showed that the flow structure behind the airfoil was strongly influenced by the change in the ride height. It was noted that as the ride height decreases, an upstream shifting of the separation point from the airfoil surface was observed.

Ol [56] experimentally investigated the unsteady aerodynamics of an oscillating SD7003 airfoil using a 2-component (pitch and plunge, arbitrary waveform and phase) electric rig in a free-surface water tunnel. Flow was seeded with dye injection and PIV measurements are done to collect the velocity field data. He investigated a parameter space of Reynolds number and reduced frequency for a flapping motion having unequal pitching and plunging frequencies and for a linear ramp motion. He found that Reynolds number has not a significant effect on the investigated cases. He also noticed that as the reduced frequency increases the persistence of the newly starting vortex near the trailing edge of the airfoil increases too.

An experimental study for characterizing the evolution of the unsteady vortex structures behind a root-fixed flapping wing to provide useful information for the development of Nano Air Vehicles (NAVs) was performed by Hu et al. [57]. The experiments were carried out in a low-speed wind tunnel using a miniaturized piezoelectric wing having a chord length of 12.7 mm. Phase-locked and time-averaged velocity field measurements were done by a DPIV system. The Reynolds number and Strouhal number of the studied cases were 1200 and 0.33, respectively. The results showed that the half of the flapping wing close to the root was drag producing whereas the other half of the flapping wing was thrust producing. In addition, it was concluded that the flapping wing would also produce lift if it was mounted initially with a positive angle of attack.

Recent advances in the experimental and numerical studies of unsteady flapping motion with applications to Micro Air Vehicle designs were also analyzed and presented by Platzer and Jones in Ref. [58].

2.3 Comparative Studies: Numerical vs. Experimental Approaches

There are many researches in the available literature related to the comparison of numerical and experimental studies conducted for the investigation of flapping wing motion for various aims. This particular section discusses some of these studies.

In one of their study, Jones et al. [59] conducted a low speed water tunnel flow visualizations using a two-color dye together with the LDV method and numerical simulations using an unsteady panel code to investigate the wake structures behind the oscillatory plunging airfoils. In this study, comparisons were made between the numerical and experimental wake structures produced. It was observed that the vortex locations obtained from the experiments show similarities with those obtained from the numerical study for low amplitude motions whereas for motions having large amplitudes and frequencies, the results of two studies were differed from each other. On the other hand, in terms of wake characteristics, the experimental and numerical results were agreed well with each other in high frequency motions too.

In another study of them, Jones et al. [60] investigated the Knoller-Betz or Katzmayr effect, known as the ability of a sinusoidally plunging airfoil to produce thrust [17], numerically and experimentally. They conducted water tunnel experiments for the visualization of the flow. Water-soluble food coloring was used for the flow visualizations while the instantaneous flow field data were acquired by the LDV technique. Numerical simulations were performed using a previously developed inviscid unsteady panel code utilizing a nonlinear wake model. Vorticity structures and instantaneous velocity profiles in the wake were then compared. As a result of comparisons made, a good agreement was obtained between the experimental and numerical studies over a wide range of reduced frequencies and Strouhal numbers. They also observed deflected vortex patterns resulting to an increase in both the average thrust and average lift at Strouhal numbers greater than 1.0. This phenomenon was observed in both the experimental and numerical results.

The investigation of flapping propulsion in ground effect was performed by Jones et al. [61] by means of experimental and numerical studies. The main aim of the study was to show that significant performance advantages are gained by flying in ground effect in terms of thrust and efficiency. To achieve this aim, a high aspect-ratio bi-plane wing model was designed and then tested both qualitatively and quantitatively. Experiments were performed in a low speed water tunnel. The flow was visualized with a smoke-wire. Instantaneous flow measurements were done by the LDV method while thrust measurements were done directly. The numerical simulations were performed using a 2-D unsteady inviscid panel code with a deforming wake model and a 2-D unsteady compressible Navier-Stokes solver with a three-block deforming grid. The results of these two studies were then compared in terms of thrust values and wake structures produced by the motion in consideration. As a result of the study, a strong Reynolds number dependence of the flow was observed.

Moreover, Wang et al. [62] performed a detailed study of a sinusoidally pitching, about its span-wise axis, and plunging, along a horizontal stroke plane, generic wing in hover to investigate the unsteady flow phenomena and compare the 2-D numerical computations with the 3-D experiments for a variety of test cases corresponding to flapping motion kinematics. Fourth-order finite difference scheme of Navier-Stokes equations in vorticity-stream function formulation were solved for the 2-D numerical simulation of the flow around a thin airfoil having an elliptical cross-section. The 3-D experimental visualization of the flow over a dynamically scaled robotic fly was done using a DPIV system. Lift and drag forces of this wing model were calculated by measuring the perpendicular shear forces exerted on the wing surface by a 2-D force sensor located at the base of one arm of the wing model. The working fluid was oil seeded with air forced through a ceramic water filter stone. As a result of the study, 2-D and 3-D aerodynamic forces were found to be very close to each other for advanced and symmetrical rotation cases whereas in delayed rotation case, they differed from each other by means of a phase shift between the computed and the measured lift.

In a comprehensive study of her, Kurtuluş [63] conducted a study on the hovering motion of a symmetrical NACA0012 airfoil in order to investigate the aerodynamic phenomena and vortex topology during the different phases of the flapping motion by means of numerical, experimental and analytical studies. The 2-D numerical simulations were performed for numerical visualization of the experiments, identification of the vortices generated, and calculation of the aerodynamic force coefficients using a Direct Numerical Simulation (DNS) code. The experiments were carried out in a water tank of 1.5 m × 1.0 m × 1.0 m in size using two different ways of visualization methods: laser sheet visualizations and PIV measurements. Results of the numerical and experimental studies were then analyzed and compared with each other in order to understand the physics of vortex formations during the different phases of the considered hovering motion and investigate the unsteady effects generated as a result of these vortices on the airfoil by means of aerodynamic force coefficients and pressure distribution. Being the last aim of this study, an analytical model was developed with the Duhamel Integral and using Wagner and Küssner functions. The model developed was found good enough for the angles of attack up to 30^o in terms of aerodynamic force coefficients calculated. Yet, it was found to be poor for giving the correct results for higher angles of attack values mainly due to the lack of ability of the model developed for the consideration of the interactions of the vortices.

An experimental and numerical investigation of the flow around a sinusoidally plunging NACA0012 airfoil was investigated by Perçin et al. [64] at a Reynolds number of about 5000 for different values of reduced frequency and amplitude of the motion. Flow visualizations were done by electrolytic precipitation method while the instantaneous velocity field data was acquired by DPIV measurements. Commercial CFD software Fluent was used for the numerical simulation of the experiments. As a result of the experiments and numerical simulations, it was found that propulsive efficiency and thrust coefficient was affected by the interaction of the leading edge and the trailing edge vortices. Moreover, in case of a sharp leading edge, the strength of the leading edge vortex increased resulting to a more energetic wake.

Ol et al. [65] conducted water tunnel experiments using a PIV system and compared the results obtained with 2-D viscous vortex particle method computations to investigate pitching motion of a flat-plate with rounded edges in forward flight. They concluded that the strength of the LEV decreases and a CCW rotating TEV is produced as the pitching rate increases. They noticed that the location of the pivot point strongly affects the size and formation of the LEV. They obtained similar results from the experiments and numerical studies in terms of vorticity fields at Reynolds number of 10000. Computing the lift numerically for Reynolds numbers of 100 and 1000, they found that it is directly proportional to the pitching rate during the upstroke. The results of this study was also included and compared with other studies in Ref. [5].

More recently, Hızlı and Kurtuluş [66] performed numerical and experimental studies on SD7003 and NACA0012 airfoils undergoing a sinusoidally pure pitching and pure plunging motions in hover in order to investigate the aerodynamics phenomena and vortex topology of these airfoils and to observe the performance of the newly built experimental setup for future applications. 2-D, unsteady, incompressible and constant property Navier-Stokes equations were solved over a C-type moving grid for the numerical visualization of the flow field. The experimental visualizations were performed in a small-scale water tank by using the PIV technique. The flow was seeded with silver coated hollow glass sphere particles. Their study emphasized that an agreement between the numerical and experimental results was obtained in terms of vortex formations behind the airfoils. In their previous study, Hızlı and Kurtuluş [67] studied the unsteady aerodynamics of purely pitching SD7003, NACA0012, 10% thick elliptical and 10% thick flat plate by means of experimental and numerical studies in hover. They analyzed and compared the results of each case in terms of velocity magnitudes in the horizontal and vertical directions and vortices. It was observed that the experimental results agreed well with the numerical results. A comparison of the numerically calculated mean aerodynamic force coefficients of the studied cases was also made.

CHAPTER 3

NUMERICAL METHOD

The entire study consists of the investigation of three different hovering types of flapping motion, namely pure pitch, pure plunge and combined pitch-plunge, of four different airfoils having a chord length of 0.06 m, namely SD7003, NACA0012, 10% thick elliptical and 10% thick flat plate, performed at very low Reynolds numbers (ranging from 98 to 1126) where the flow is assumed to be fully laminar. Therefore, the numerical results are acquired by solving the unsteady, incompressible and constant property Navier-Stokes equations. For all studied cases, the computations are performed at zero free stream velocity since the hovering case of flapping motion is under investigation. In the present study, commercially available CFD package program Fluent v6.3.26 is chosen as the numerical tool and used on moving 2-D and 3-D grids with finite-volume methods [68].

3.1 Governing Equations

The governing equations of hovering motion are the incompressible and constant property Navier-Stokes equations as stated before. Throughout the study, the mass of the airfoil is neglected and therefore, the body force term is dropped from the governing equations [14]. Then, the Navier-Stokes equations with the continuity equation are given as follows;

$$\frac{\partial}{\partial x_i} U_i = 0 \tag{3.1.1}$$

$$\frac{\partial}{\partial t} U_i + \frac{\partial}{\partial x_j} U_j U_i = -\frac{1}{\rho}\frac{\partial p}{\partial x_i} + \upsilon \frac{\partial^2}{\partial x_j^2} U_i \tag{3.1.2}$$

where x_i is the i^{th} component of the position vector, U_i is the velocity component in i^{th} direction, t is the time variable, ρ is the density of the flow, p is the pressure and υ is the kinematic viscosity of the flow.

3.2 Flow Field Description

In the present study, due to the nature of the simulation, the transient (or unsteady) calculations are carried out on moving 2-D and 3-D computational grids by the pressure-based finite volume solver for the computation of 4000 iterations with a time step size of 0.025 s, which allows a full simulation of 100 seconds of flapping motion, i.e. 10 periods of flapping motion. First order implicit temporal discretization, second order upwind spatial discretization and SIMPLE (Semi-Implicit Method for Pressure-Linked Equations) algorithm for pressure-velocity coupling for all studied cases are used by Fluent [69]. Moreover, the working fluid is chosen as water for all studied cases in order to be consistent with the experiments. The thermo-physical properties of the working fluid water at ambient conditions of 20^{o}C are specified in Table 3.2.1 [70].

Table 3.2.1 Thermo-physical properties of the working fluid water.

Property	**Unit**	**Value**
Temperature (T)	[^{o}C]	20
Density (ρ)	[kg/m^3]	998.2
Dynamic Viscosity (μ)	[kg/m·s]	1.003×10^{-3}
Kinematic Viscosity (υ)	[m^2/s]	1.004×10^{-6}

3.3 Computational Grid and Boundary Conditions

In the present study, the desired modes of hovering motion are implemented by moving the whole computational grid domain since the free stream velocity is zero in hovering flight [71]. In other words, the computational grid translates/rotates along/around the coordinate system according to the desired flapping motion definitions. For this, a C-type structured 2-D grid domain having 128000 quadrilateral cell elements (fine grid domain) generated in commercial grid generation software Gambit 2.4.6 is used. There are 256 grid points on the airfoil surface. 20 grid points normal to the flow direction is placed in order to resolve the boundary layer. The first normal grid point is located at 10^{-6} m from the airfoil surface. The boundaries of the computational grid are at 12 chords in downside direction, 8 chords in upside direction and 9 chords in downstream and upstream directions (see Figure 3.3.1).

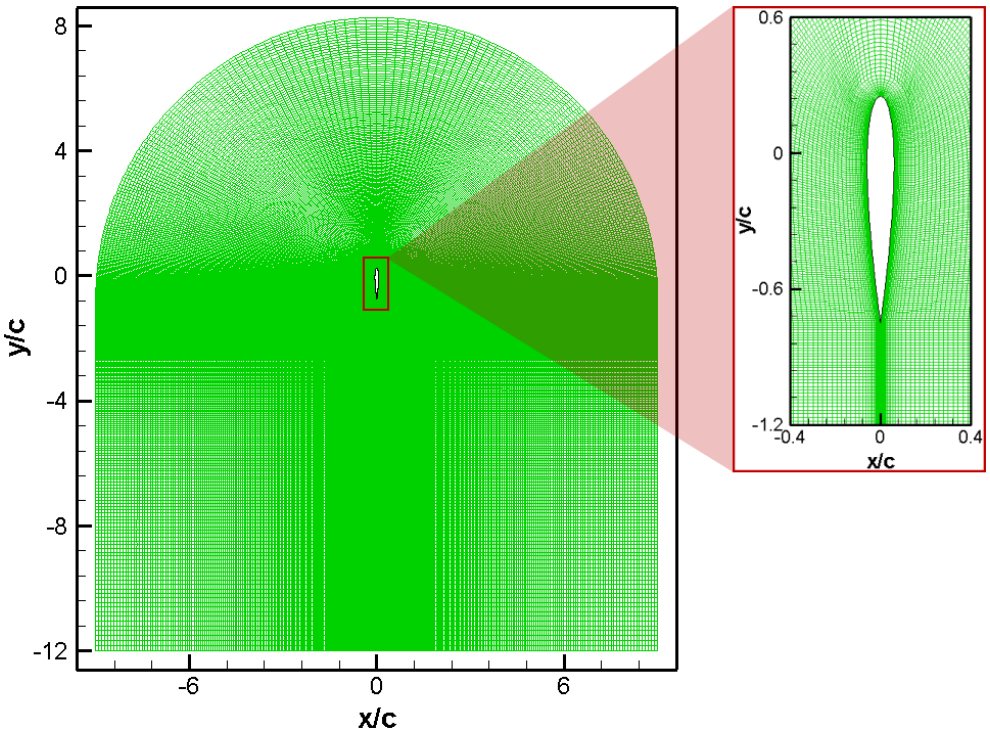

Figure 3.3.1 2-D fine computational grid domain (left) and its distribution around the NACA0012 airfoil (right).

In addition, a C-type 2-D grid domain having 7384 quadrilateral cell elements (coarse grid domain) is also constructed for SD7003 and NACA0012 airfoils in order to study the effect of domain resolution difference between the CFD and PIV calculations. The number of elements used to construct this grid domain is decided such that they are close enough to the number of elements existing in the velocity field of the PIV visualizations, 7326 (99 × 74) in the present study. In this grid domain, the airfoil surface has 104 grid points. The boundary layer is resolved by placing 8 grid points normal to the flow direction. The first normal grid point is located at 10^{-4} m from the airfoil surface. The sizes of the boundaries of the coarse computational grid are the same with the fine grid domain previously mentioned. A schematic illustration of the coarse grid domain is given in Figure 3.3.2 below.

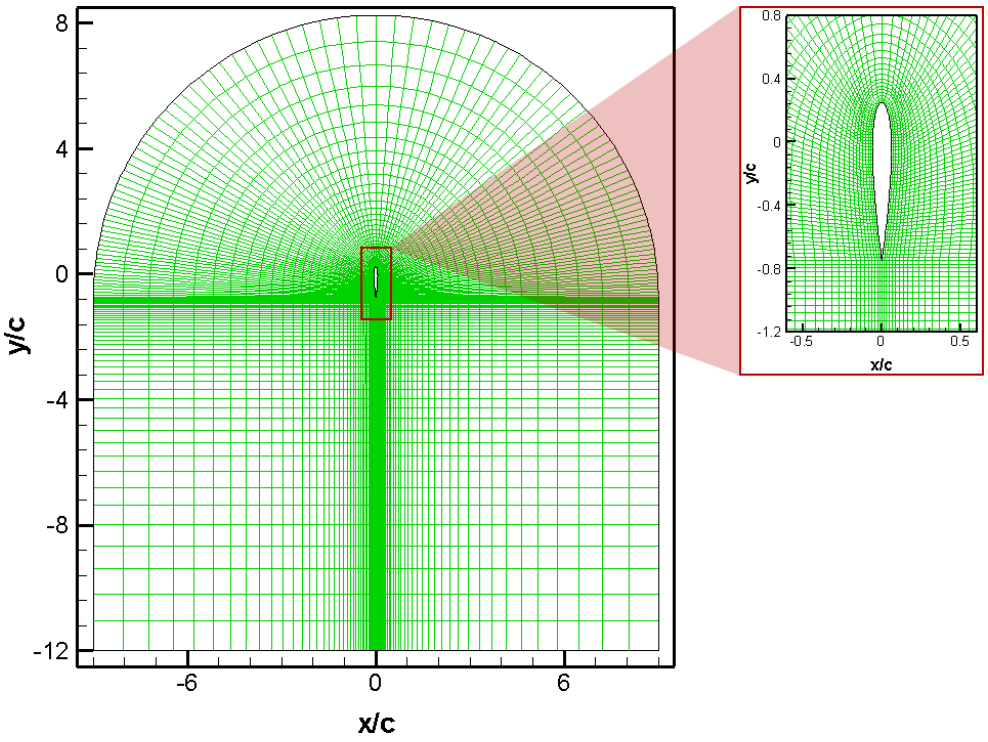

Figure 3.3.2 2-D coarse computational grid domain (left) and its distribution around the NACA0012 airfoil (right).

The outer boundaries of the 2-D grid domains are defined as the pressure outlet boundary condition. The standard air pressure is assumed to be the far-field pressure [63]. Moreover, no-slip wall boundary condition is implemented on the airfoil

surface. Any boundary condition is not applied on the wake of the airfoil. The fine and coarse grid domains for all airfoils considered are similar to the domains shown in Figure 3.3.1 and Figure 3.3.2, respectively. Hence these grid domains are representative for all airfoils.

In order to study the three-dimensional effects for the baseline cases, a 3-D computational grid domain for wing models having SD7003 and NACA0012 airfoil is also constructed using 1850000 tetrahedral/hybrid cell elements. The size of the grid domain is identical with the size of the water tank used in the experiments, i.e. 0.8 m × 0.4 m × 0.4 m. The wing models used in this domain have a chord length of 0.06 m and a span of 0.13 m, which is the part of the wing model under water during the experiments. As in the case of 2-D grid domains, wing surface is set to have no-slip wall boundary condition. The outer boundaries of the 3-D grid domain are defined in such a way that the computational grid domain simulates the water tank used in the experiments. In other words, pressure outlet boundary condition is applied in upper side of the outer boundary and no-slip wall boundary condition is applied in all other sides of the outer boundary.

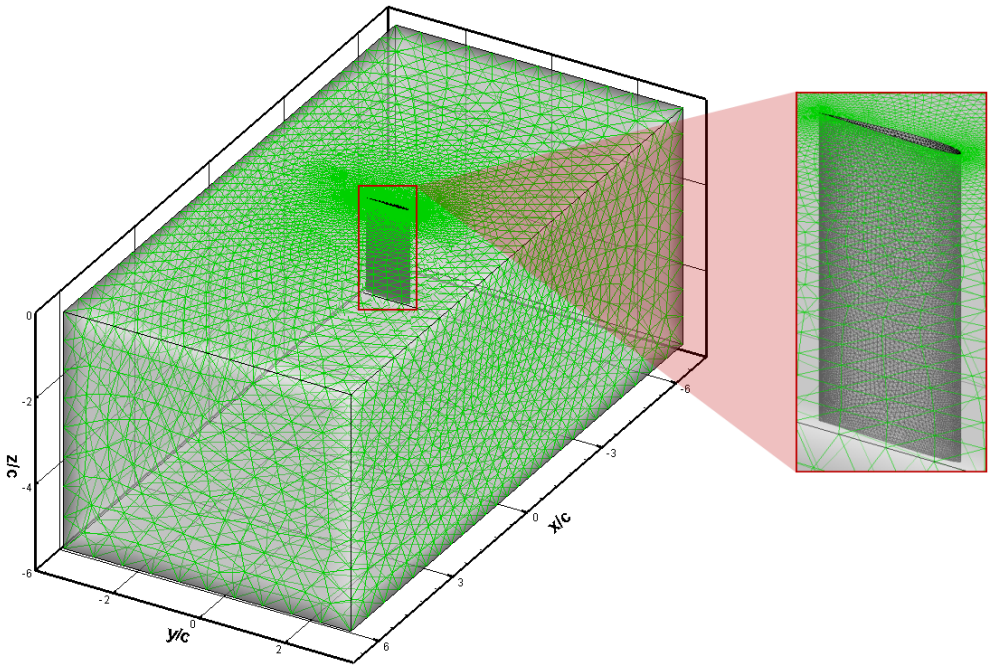

Figure 3.3.3 3-D computational grid domain (left) and its distribution around the wing model having SD7003 airfoil (right).

3.4 Grid and Time-step Refinement Studies

For all studied 2-D cases, in order to obtain grid and time-step independent numerical solutions, grid and time-step refinement studies are carried out. The refinement studies are carried out for 2-D fine grid domain cases only. In Figure 3.4.1, the results of grid and time-step refinement studies for purely pitching NACA0012 airfoil in terms of lift and drag coefficient distributions over three periods of motion are shown. It should be noted that the refinement studies are carried out for each type of hovering motion considered. Yet, only the results of the purely pitching ($\alpha_a=30^o$) NACA0012 airfoil are presented since the results of the refinement studies of each studied case are found to be very similar with each other.

For the grid independency study, three C-type 2-D structured grid domains having 63000, 128000 and 246000 cell elements are considered. As it can be seen in Figure 3.4.1 (top), similar results are obtained from each grid domain in terms of C_L and C_D variations. In terms of vortex field generated and aerodynamic force and moment coefficients calculated, similar results are obtained from grids having 128000 and 246000 cell elements. However, it is observed that the vortices diffuse quicker and some discrepancies in convergence histories of aerodynamic force and moment coefficients occur in case of grid having 63000 cell elements. As a result of grid independence test, a grid having 128000 cell elements is chosen to be sufficiently fine to have grid independent solution.

The time-step independency study is performed for four different time-step size (Δt) values such as 0.05 s, 0.025 s, 0.02 s and 0.0125 s, corresponding to 200, 400, 500 and 800 time-steps, respectively, over one period (T) of motion. As it can be seen in Figure 3.4.1 (bottom), very similar C_L and C_D distributions are obtained from the cases having time-step sizes of 0.025 s, 0.02 s and 0.0125 s. Considering also the CPU time spent for the calculations, 400 time-steps over one period of motion is found to be enough to be used for further studies.

The numerical studies are carried out on a quad-core personal computer having an AMD processor of 3.4 GHz of CPU speed and 8 GB of RAM. It is observed that the CPU time spent for the grids having different number of cell elements is moderately close to each other but it varies for the cases having different time-step sizes while the grid sizes are the same. The CPU time spent for calculations played an important role for choosing the time-step for further studies. It is observed that about 8 hours of CPU time is spent for the calculation of 4000 iterations for a grid domain having 128000 elements and $T/\Delta t$=400. On the other hand, it is about 10 hours for a grid domain having 128000 elements and $T/\Delta t$=500.

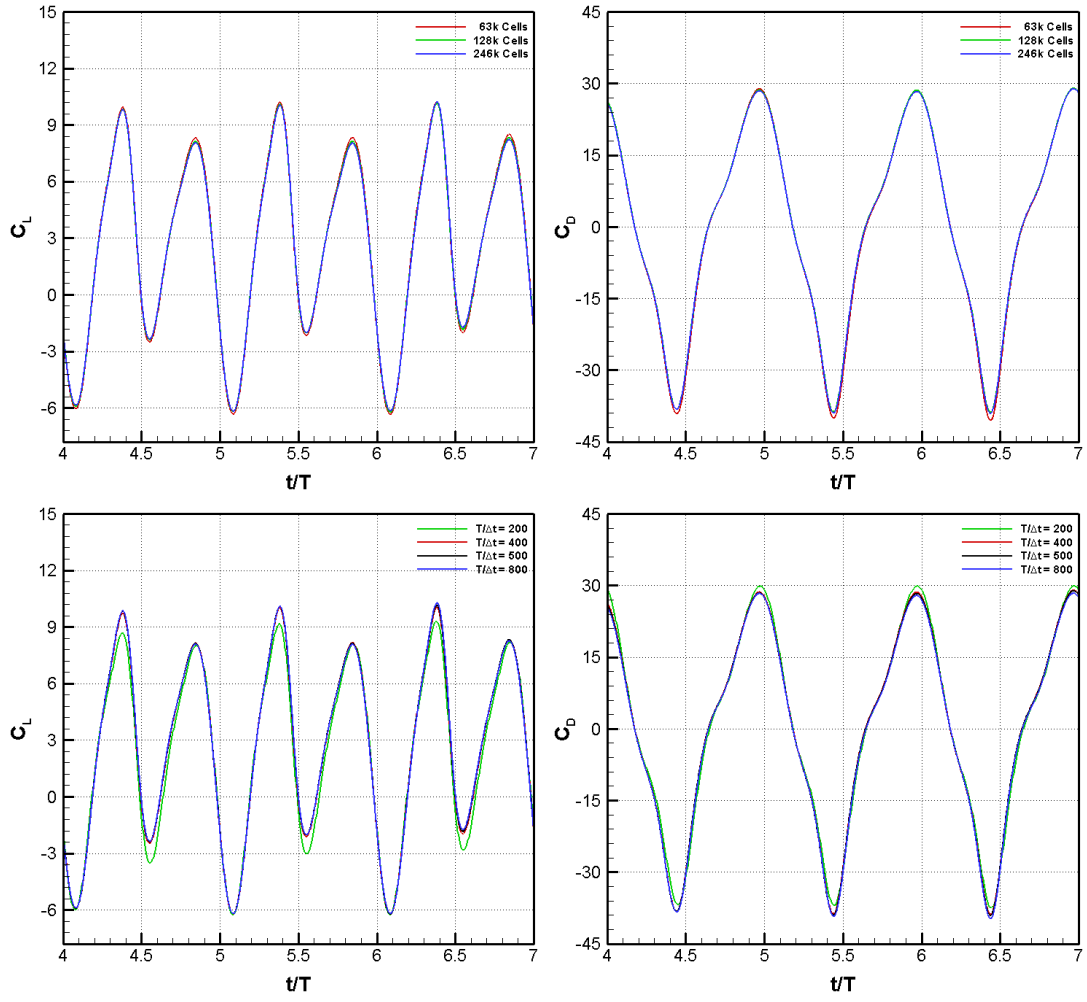

Figure 3.4.1 Time histories of lift and drag coefficients with different grids (top) and with different time-steps (bottom) for purely pitching ($\alpha_a=30^o$; $k=3.8$) NACA0012 airfoil over three periods of motion.

3.5 Hovering Kinematics

Hovering motion is defined as the flapping motion where there is no free stream velocity exist [63]. The present study is related to the investigation of three different modes of hovering motion, namely pure pitch, pure plunge and combined pitch-plunge. The first one, pure pitch motion, is defined as the rotational motion around a pivot point. In this study, the pivot point is chosen to be the quarter-chord location of the airfoil from its leading edge [72]. The axial displacement of the pivot point is zero in this case. Pure plunge motion is defined as the translational motion of the airfoil in the horizontal direction (*x*-direction) [66]. In this case, the angular displacement of the pivot point is zero. And combined pitch-plunge motion is defined as the motion composed of the superposition of the rotational motion around the pivot point and the translational motion in the horizontal direction [42].

Each investigated hovering motion is divided into four temporal regions. The first and third regions correspond to the first and second half of the downstroke, respectively. On the other hand, the second and the fourth regions represent the first and second half of the upstroke, respectively. Figure 3.5.1 shows the schematic description of the each hovering motion considered in one period.

Pure pitch, pure plunge and combined pitch-plunge motions investigated in the present study are described with the following sets of equations, respectively:

$$\begin{pmatrix} x(t) \\ y(t) \\ \alpha(t) \end{pmatrix} = \begin{pmatrix} 0 \\ 0 \\ \alpha_a \sin(wt) \end{pmatrix} \tag{3.5.1}$$

$$\begin{pmatrix} x(t) \\ y(t) \\ \alpha(t) \end{pmatrix} = \begin{pmatrix} x_a \sin(wt) \\ 0 \\ 0 \end{pmatrix} \tag{3.5.2}$$

$$\begin{pmatrix} x(t) \\ y(t) \\ \alpha(t) \end{pmatrix} = \begin{pmatrix} x_a \sin(wt) \\ 0 \\ \alpha_a \sin(wt) \end{pmatrix} \tag{3.5.3}$$

In the above equations, *x(t)* is the instantaneous horizontal position of the airfoil, *y(t)* is the instantaneous vertical position of the airfoil, *α(t)* is the pitch angle variation with respect to the pivot point. x_a is the horizontal plunging amplitude in meters, α_a is the pitching amplitude in radians. *w* is the angular frequency, $w=2\pi f$, where *f* is the frequency of the sinusoidal oscillation, and *t* is the time variable.

In this study, *f* is chosen as 0.1 Hz; x_a is chosen as 0.01 m, 0.02 m and 0.03 m; and α_a is chosen as π/18, π/6 and π/4 radians, i.e. 10^o, 30^o and 45^o, respectively.

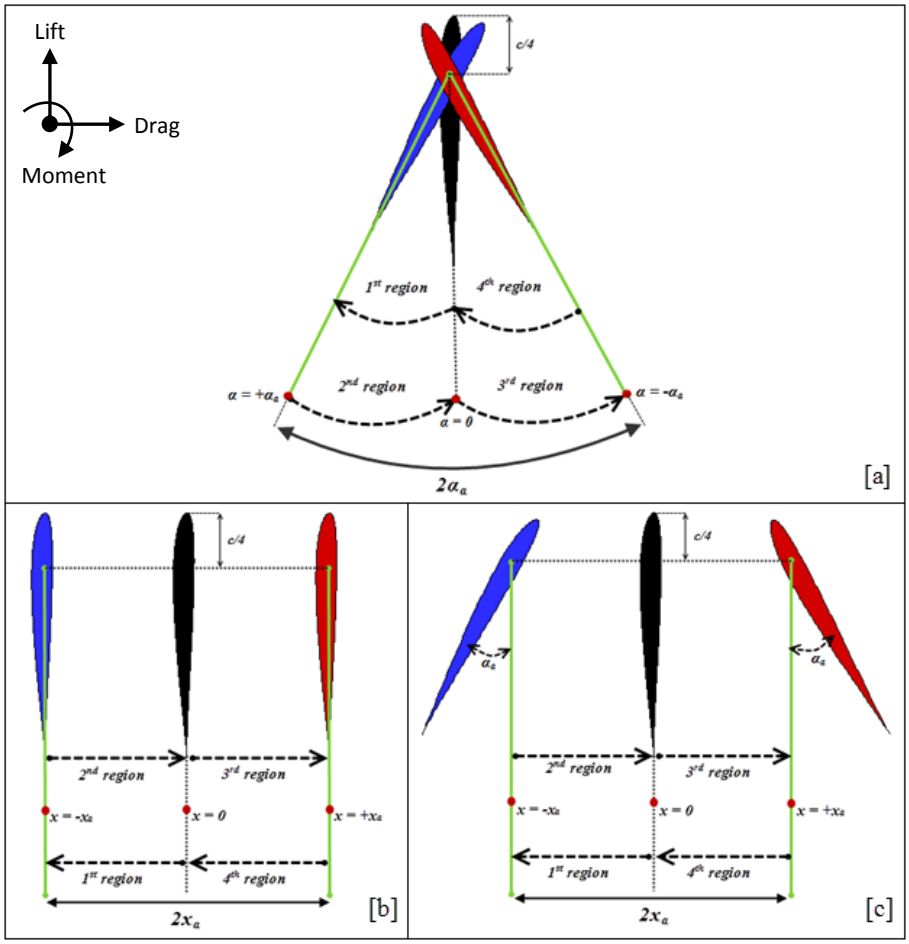

Figure 3.5.1 Schematic description of the investigated hovering motion cases: [a] pure pitch motion, [b] pure plunge motion, [c] combined pitch-plunge motion.

The axial velocity in the horizontal direction (*x*-direction), *u(t)*, the axial velocity in the vertical direction (*y*-direction), *v(t)*, and the angular velocity, *ω(t)*, with respect to the pivot point, are then defined as the time derivatives of *x(t)*, *y(t)* and *α(t)*, respectively. For all studied cases, since there is no translational motion in the vertical direction, axial velocity in this direction is zero. The axial and the angular velocities for pure pitch, pure plunge and combined pitch-plunge type of hovering motion cases are defined by the following sets of equations, respectively:

$$\begin{pmatrix} u(t) \\ v(t) \\ \omega(t) \end{pmatrix} = \begin{pmatrix} 0 \\ 0 \\ \alpha_a w \cos(wt) \end{pmatrix} \tag{3.5.4}$$

$$\begin{pmatrix} u(t) \\ v(t) \\ \omega(t) \end{pmatrix} = \begin{pmatrix} x_a w \cos(wt) \\ 0 \\ 0 \end{pmatrix} \tag{3.5.5}$$

$$\begin{pmatrix} u(t) \\ v(t) \\ \omega(t) \end{pmatrix} = \begin{pmatrix} x_a w \cos(wt) \\ 0 \\ \alpha_a w \cos(wt) \end{pmatrix} \tag{3.5.6}$$

The prescribed modes of hovering motion are implemented to the CFD solver via User Defined Functions (UDFs). The axial and the rotational velocities of the airfoil around its quarter-chord location are the inputs of the UDF subroutine [69].

3.6 Significant Non-Dimensional Parameters

Reynolds number (*Re*) and reduced frequency (*k*), which have significant importance regarding to the flow dynamics, are two non-dimensional similarity parameters commonly used in flapping wing aerodynamics [14]. The ratio of the inertial forces to the viscous forces in fluid flow is represented by Reynolds number. On the other hand, the residence time of a fluid particle travelling over the chord of the airfoil compared to the period of flapping motion is described by reduced frequency [7].

Definitions of the Reynolds number and the reduced frequency are given by the following equations, respectively:

$$Re = \frac{U_{ref} \cdot c}{\upsilon} \tag{3.6.1}$$

$$k = \frac{w \cdot c}{2U_{ref}} \tag{3.6.2}$$

In the above equations, υ is the kinematic viscosity of the fluid, 1.004×10^{-6} m^2/s for water, c represents the chord length of the airfoil, 0.06 m. w is the angular frequency, $w=2\pi f$, and U_{ref} is the reference velocity.

In hovering flight, since there is no free stream velocity exists, the reference velocity U_{ref} is defined, in the present study, as the maximum velocity at the leading edge of the airfoil and it is given by the following equation ([14]):

$$U_{ref} = \sqrt{\dot{x}(t)^2 + \dot{y}(t)^2 + \left(\frac{\dot{\alpha}(t) \cdot c}{4}\right)^2}\Bigg|_{max} \tag{3.6.3}$$

From the above equation, the reference velocity U_{ref} for pure pitch, pure plunge and combined pitch-plunge motions is then obtained as seen in Table 3.6.1.

Table 3.6.1 The reference velocity definitions for the investigated cases.

	Pure Pitch	**Pure Plunge**	**Combined Pitch-Plunge**
$\boldsymbol{U_{ref}}$ **[m/s]**	$w \cdot \frac{c}{4} \cdot \alpha_a$	$w \cdot x_a$	$w\sqrt{{x_a}^2 + \left(\frac{c}{4} \cdot \alpha_a\right)^2}$

The reference velocity, Reynolds number (*Re*) and reduced frequency (*k*) values of investigated test cases are given in Table C.3, in Appendix B section of the thesis.

3.7 Definition of the Vorticity

In this study, vorticity, which describes the local rotational motion of a fluid particle, is defined as the curl of the velocity field. The vorticity is expressed by the following equation [63]:

$$\vec{\omega} = \vec{\nabla} \times \vec{U} \tag{3.7.1}$$

In the above equation, U represents the velocity vector.

In the present study, since all discussions are made based on the 2-D results obtained, only z-component of the vorticity vector is interested. Knowing this fact and carrying out the cross product operation, the vorticity takes the following form:

$$\vec{\omega} = \vec{\omega_z} = \left[\frac{\partial v}{\partial x} - \frac{\partial u}{\partial y} \right] \cdot \vec{k} \tag{3.7.2}$$

3.8 Calculation of the Aerodynamic Force and Moment Coefficients

To quantify the flow characteristics, in the present study, lift, drag and moment coefficient per unit span calculations are done numerically according to the following equations, respectively:

$$C_L = \frac{L}{1/2 \cdot \rho_\infty \cdot U_{ref}{}^2 \cdot c} \tag{3.8.1}$$

$$C_D = \frac{D}{1/2 \cdot \rho_\infty \cdot U_{ref}{}^2 \cdot c} \tag{3.8.2}$$

$$C_M = \frac{M}{1/2 \cdot \rho_\infty \cdot U_{ref}{}^2 \cdot c^2} \tag{3.8.3}$$

In the above equations, ρ_∞ stands for the density of the flow, 998.2 kg/m^3 for water. c is the chord length of the airfoil. L, D and M represent the lift force, drag force and moment created by the lift and drag forces at the pitching axis, respectively. It should be noted that the lift forces, drag forces and moments are calculated with respect to the axis orientation represented in Figure 3.5.1.

Mean aerodynamic force and moment coefficients are then calculated as the time average of instantaneous values over the one period of motion. In the present study, these coefficients are calculated for the sixth period of the motion, where the impulsive effects of the motion have been observed to disappear and periodical motions are obtained ([63], [66]). Mean aerodynamic force and moment coefficients are calculated by the following equations, respectively:

$$\overline{C_L} = \frac{1}{T}\int_T^{t+T} C_L(t)dt \tag{3.8.4}$$

$$\overline{C_D} = \frac{1}{T}\int_T^{t+T} C_D(t)dt \tag{3.8.5}$$

$$\overline{C_M} = \frac{1}{T}\int_T^{t+T} C_M(t)dt \tag{3.8.6}$$

3.9 Calculation of the Total Force

For the cases investigated, the instantaneous total forces are calculated numerically as the sum of the pressure and shear forces exerted on the airfoil [63]:

$$\overline{F}_{total} = \overline{F}_{pressure} + \overline{F}_{shear} \tag{3.9.1}$$

3.10 Test Cases

Test cases investigated in the present study, which are composed of four different airfoils, namely SD7003, NACA0012, 10% thick elliptical and 10% flat plate, undergoing three different modes of hovering motion, pure pitch, pure plunge and combined pitch-plunge having different pitching and plunging amplitudes, are tabulated in the following table. Since the present study is mostly focused on the flapping motion of the SD7003 and NACA0012 airfoils, low amplitude cases of other two airfoils are not studied.

Table 3.10.1 Test cases investigated during the study.

Motion \ Airfoil	SD7003	NACA0012	10% Thick Elliptical	10% Thick Flat Plate
Pure Pitch	$\alpha_a = 10°$	$\alpha_a = 10°$	-	-
	$\alpha_a = 30°$	$\alpha_a = 30°$	$\alpha_a = 30°$	$\alpha_a = 30°$
	$\alpha_a = 45°$	$\alpha_a = 45°$	$\alpha_a = 45°$	$\alpha_a = 45°$
Pure Plunge	$x_a = 0.01\ m$	$x_a = 0.01\ m$	$x_a = 0.01\ m$	$x_a = 0.01\ m$
	$x_a = 0.02\ m$	$x_a = 0.02\ m$	$x_a = 0.02\ m$	$x_a = 0.02\ m$
	$x_a = 0.03\ m$	$x_a = 0.03\ m$	-	-
Combined Pitch-Plunge	$\alpha_a = 10°$ $x_a = 0.01\ m$	$\alpha_a = 10°$ $x_a = 0.01\ m$	-	-
	$\alpha_a = 10°$ $x_a = 0.02\ m$	$\alpha_a = 10°$ $x_a = 0.02\ m$	-	
	$\alpha_a = 30°$ $x_a = 0.01\ m$	$\alpha_a = 30°$ $x_a = 0.01\ m$	$\alpha_a = 30°$ $x_a = 0.01\ m$	
	$\alpha_a = 30°$ $x_a = 0.02\ m$	$\alpha_a = 30°$ $x_a = 0.02\ m$	$\alpha_a = 30°$ $x_a = 0.02\ m$	
	$\alpha_a = 45°$ $x_a = 0.01\ m$	$\alpha_a = 45°$ $x_a = 0.01\ m$	$\alpha_a = 45°$ $x_a = 0.01\ m$	
	$\alpha_a = 45°$ $x_a = 0.02\ m$	$\alpha_a = 45°$ $x_a = 0.02\ m$	$\alpha_a = 45°$ $x_a = 0.02\ m$	

Among the above mentioned test cases, six baseline test cases corresponding to the pure pitch, pure plunge and combined pitch-plunge motions having two different pitching and/or plunging amplitudes are chosen in order to analyze these baseline test cases in more detail. It is mainly aimed to investigate the three-dimensional effects and the effects of domain resolution difference between the CFD simulations and PIV visualizations by these baseline cases. The baseline studies are decided to be carried out for SD7003 and NACA0012 airfoils only since these airfoils are more commonly used in the flapping motion related researches in the literature. In Figure 3.10.1, the parameter space considered and baseline test cases decided, denoted by blue triangles, are given. The reduced frequency, *k*, and Reynolds number, *Re*, values corresponding to each test case are also shown in this figure.

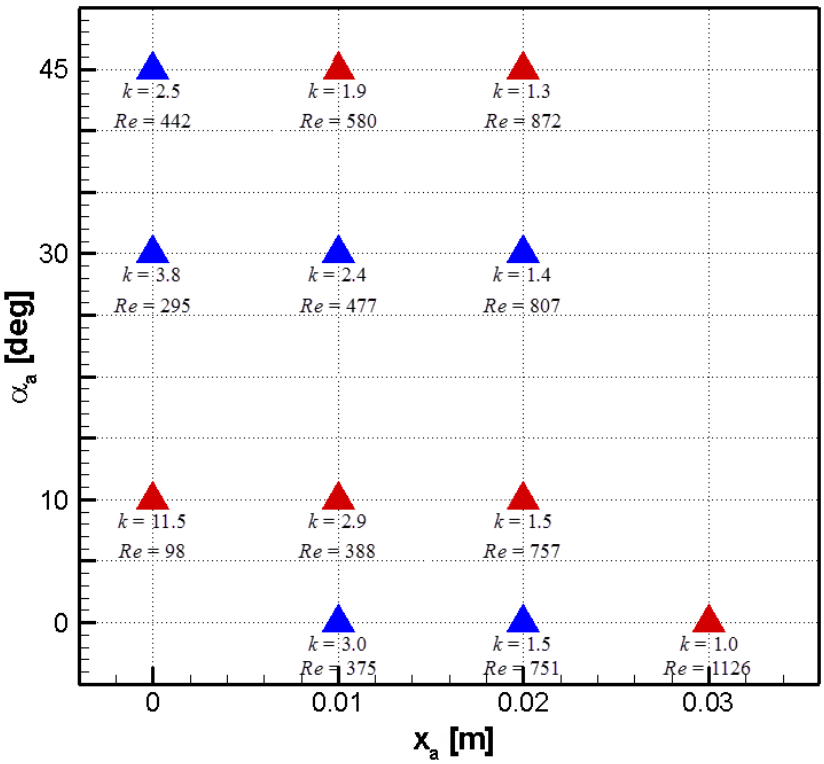

Figure 3.10.1 The parameter space considered and baseline test cases, denoted by blue triangles.

CHAPTER 4

EXPERIMENTAL METHOD

In the literature, different experimental techniques are used in order to collect the instantaneous velocity field data of the flow around a rigid body. Hot-Wire, Laser Doppler Velocimetry (LDV) and Particle Image Velocimetry (PIV) are the ones that are most commonly used for this purpose. However, it can be a time consuming and difficult work to gather the time dependent velocity field by Hot-Wire and LDV in an experiment since these methods are lack of the ability of measuring the whole velocity field simultaneously [73]. PIV, a laser-based, non-intrusive velocity measurement method, is a better alternative over others and capable of measuring the instantaneous velocity field in steady and unsteady flows [72]. Therefore, in the present study, PIV technique is chosen to be used for performing the instantaneous flow field measurements of the flow around the aforementioned airfoils undergoing sinusoidal pure pitch, pure plunge and combined pitch-plunge motions in hover.

4.1 Experimental Setup

The experimental setup used throughout the present study mainly consists of a small-scale water tank filled with water, a computer controlled positioning system allowing the translational and the rotational motions of the wing model and a PIV system composed of a dual-pulse laser and a CCD camera. The schematic illustration of the experimental setup used in the present study is shown in Figure 4.1.1.

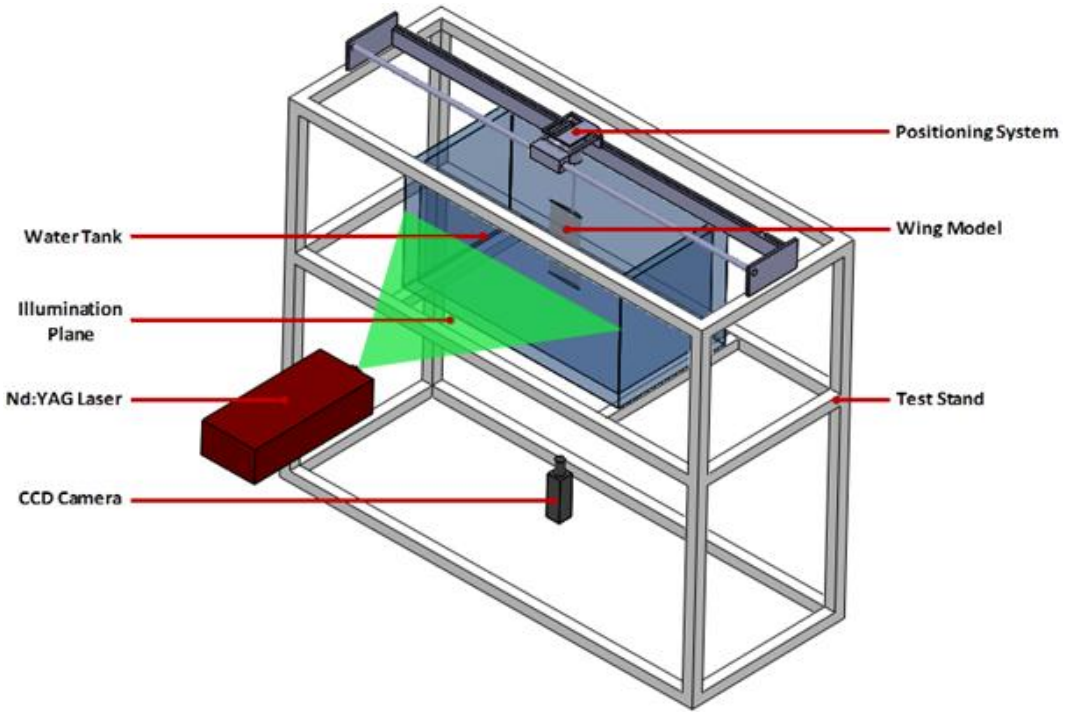

Figure 4.1.1 The schematic illustration of the experimental setup.

4.1.1 Wing Models Considered

Four different rectangular wing models having SD7003, NACA0012, 10% thick elliptical and 10% thick flat plate airfoils made of transparent Plexiglas material are used in the experimental part of the thesis in order to be consistent with the numerical studies (see Figure 4.1.2). The wing models considered have a chord length of 0.06 m and span of 0.25 m. The edges of the wing model having flat plate airfoil are rounded in order not to have massive flow separations around it [67].

The center of rotation of each wing model is fixed at the quarter chord location, from their leading edges, in order to match with the numerical studies. Moreover, the test section, i.e. the illuminated plane, is located at the half of the span that is inside the water for all experiments carried out. In the present study, the span that is inside the water is 0.13 m for each investigated wing model. Hence, the laser sheet crosses the each wing model at 0.065 m from the water surface.

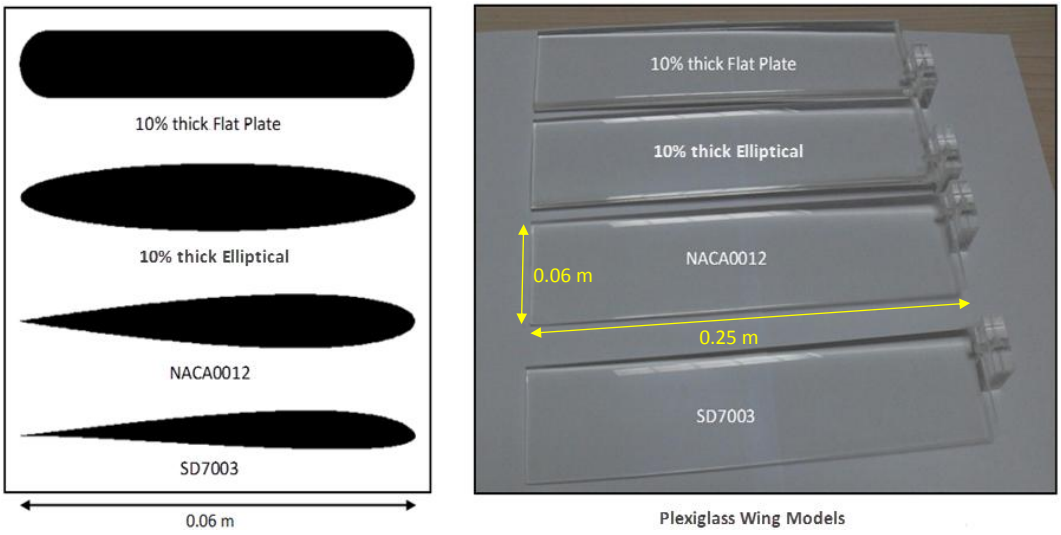

Figure 4.1.2 Wing models with different airfoils considered.

4.1.2 The Water Tank

The experiments are carried out in a small-scale water tank in the Aerodynamics Laboratory at the Department of Aerospace Engineering of METU. This is a 0.8 m × 0.4 m × 0.4 m (length × width × height) water tank made of transparent Plexiglas material. The water tank is filled with purified water in order not to have unwanted particles inside the water during the experiments. Purification process is carried out by filtering the tap water mechanically with a water purifying equipment.

4.1.3 Definition of the Flow

The experiments for all studied cases, described in detail in Section 3.5, are carried out in zero free stream velocity due to the nature of the hovering motion. This means that a steady flow in the water tank should be achieved at the beginning of each experiment. In order to guarantee this, for each investigated case, a minimum of fifteen minutes is waited before starting to the following experiment [63]. Afterwards, the flow in the water tank is observed whether it is steady or not.

4.1.4 The Positioning System

A positioning system is placed on top of the water tank to give the intended motion to the wing models. The schematic illustration of the positioning system is shown in Figure 4.1.3. The system is capable of controlling and logging the motion of the wing models in real-time through a PC installed Data Acquisition Board (DAQ Board) and MATLAB/Simulink™ software. DAQ Board serves as the signal acquisition and command generation electronics onboard the PC. Encoder signals, motor driving logic and commands are generated on the DAQ Board. The board is also compatible with the MATLAB/Simulink™ software enabling real-time implementations.

In the system, the translational motion in the horizontal direction is achieved by the motion of the first step motor along the rack via the pinion mounted on it. The rotational motion is controlled by the second step motor mounted to the cart. The useful rotational motion is 360^{o}. The second step motor is connected to the quarter-chord locations of each wing model from their leading edges. Both step motors are driven by pulse width modulation (PWM) signals through commands received from the controller PC through the DAQ Board.

The period of each hovering motion is set to 10 s and the maximum angular velocity is then limited as 0.63 rad/s in order to be consistent with the numerical studies.

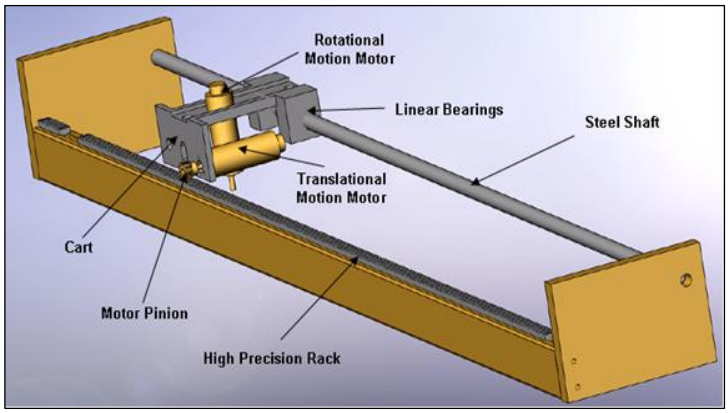

Figure 4.1.3 The schematic illustration of the positioning system.

4.2 Particle Image Velocimetry (PIV)

A Particle Image Velocimetry (PIV) system from Dantec Dynamics [74] is used to collect the instantaneous velocity field data of the flow round the wind models considered. A PIV system mainly consists of a high power laser for illuminating the test section, a camera, a CCD camera in general, for image acquisition and seeding particles in various types. The general working principle of the PIV method can be summarized as visualizing the flow by the seeding particles to take double frame images of a test section illuminated by the laser and then storing these images to the buffer of the computer for performing an integration analysis later to obtain a unique velocity field data of the flow.

The detailed explanations of four main requisites for the PIV measurements performed, namely illumination, seeding, image acquisition and data analysis, are given in the following sections.

4.2.1 Illumination

An Nd:YAG (Neodymium-doped Yttrium Aluminum Garnet) laser system from New Wave Research having a maximum power of 200 mJ/pulse is used in the present experiments in order to illuminate the flow. The power of the laser can be changed by the control panel located on the laser housing. During the experiments a power of 120 mJ/pulse is used. Nd:YAG lasers can operate in single or dual pulse modes [75]. In the present study, dual pulse mode of the laser is used with time difference of 10000 μs between the two laser pulses. The illumination plane is arranged in such a way that the laser sheet crosses the wing model from its mid-span that is inside the water, 0.065 m from the water surface, and it is perpendicular to the camera.

4.2.2 Seeding

For seeding the flow, various kinds of seeding particles are used in PIV systems. Fog, smoke, atomizing glycerin or water/oil mixtures are used for the experiments carried out in air. On the other hand, fluorescent dyes, hollow glass sphere particles or silver coated hollow sphere particles are treated as seeding particle in the experiments with water [76].

Among the alternatives that can be used as a seeding particle in the present study, namely hollow glass sphere particles and silver coated hollow glass sphere particles, silver coated hollow glass sphere particles with an average diameter of 10 μm are chosen to be used. They have the advantage of reflecting the laser light better than the hollow glass sphere particles. However, since they are coated with silver, they are heavier than the hollow glass sphere particles. In other words, silver coated hollow sphere particles have a density slightly greater than that of water. Therefore, an error in the out of plane velocity caused by the gravity appears in the experimental results. Yet, this error is neglected in the present study since the illumination plane is arranged horizontally in all studied cases [77].

The concentration of the particles in the water tank is 4.75×10^{-5} g/cm^3. The concentration of the seeding is decided such that no blurred snapshots are taken due to rich seeding and no flow field regions having lack of velocity information are obtained as a result of poor seeding [73].

4.2.3 Image Acquisition

In the present study, a FlowSense 2M/E CCD camera having an AF-MICRO-NIKKOR objective of 60 mm with an aperture setting of f#2.8 is used to take the snapshots having the instantaneous velocity information of the flow at any instant. The camera is placed under the water tank perpendicular to the illumination plane.

The camera operates in synchronized fashion with the Nd:YAG laser. The synchronization between the CCD camera and the Nd:YAG laser is achieved by a National Instruments PCI-6601 timer device. Since the Nd:YAG laser used in the experiments emits green light with a wavelength of 532 nm, a green light filter is attached to the camera in order to increase the quality of the snapshots taken. Double frame / double exposure images, which means the scattered lights of the first and the second illumination are recorded in sequential two frames, respectively [63], are taken during the experiments. The frame rate of the recordings is 5 Hz. This means that 50 double images in a period of motion (T=10 s) are taken by the camera. For each case investigated, 300 double frame images are taken in order to obtain the instantaneous velocity vectors around the airfoils for six period of hovering motion. The resolution of the snapshots is 1600 × 1200 pixels. The PIV measurements in the present study are performed within a field of view of 150 × 112.5 mm^2.

4.2.4 Data Analysis

The captured images are then interrogated by means of a double frame, adaptive cross correlation method via a 2-D FFT calculation with an initial interrogation area of 64 × 64 pixels and going down to 32 × 32 pixels each with two iterations with 50% integration area overlapping in each direction in order to extract the instantaneous velocity information from the captured images ([78], [79]). By repeating the cross correlation for each interrogation area over the two frame of images captured, velocity vector map of the whole flow is obtained at that instant [80]. The main aim of the interrogation analysis is to determine the displacement between sequential images in order to calculate the velocity vector at that instant [63]. In this study, this process is carried out by commercially available Dantec Dynamics' DynamicStudio software [81]. The output of the interrogation analysis is the velocity vector field, i.e. x and y components of the velocity at any instant depending on the location. Then, these data are used to compute vorticity vector map of the flow at any instant.

4.3 Summary of the Experimental Conditions

The summary of the experimental conditions for the PIV measurements carried out is tabulated in Table 4.3.1.

Table 4.3.1 Summary of the experimental conditions for the PIV measurements.

Wing Model	Airfoil	SD7003, NACA0012, 10 % thick elliptical, 10% thick flat plate
	Chord [m]	0.06
	Span [m]	0.25
Flow	Fluid	Water
	Temperature [°C]	20
Motion	Period [s]	10
	Max. Angular Velocity [rad/s]	0.63
Seeding	Type	Silver Coated Hollow Glass Spheres
	Diameter [μm]	10
	Concentration [g/cm^3]	4.75×10^{-5}
Laser	Type	Nd:YAG
	Pulse Energy [mJ/pulse]	120
Recording	Camera Type	CCD FlowSense 2M/E
	Number of Camera	1
	Lens Focal Length [mm]	60
	Frame Rate [Hz]	5
	$\Delta t/T$	0.02
	Resolution [pixels]	1600 x 1200
	Exposure Delay Time [μs]	10000
	Synchronization	via National Instruments PCI-6601 Timer Device
Interrogation	Method	Double Frame / Double Exposure & Adaptive Cross Correlation
	Resolution	Initial: 64 × 64 pixels Final: 32 × 32 pixels each with two iterations with 50% overlap

4.4 Experimental Procedure

Working with PIV is not ordinary and great care should be taken in order for the experiments to be successful. For this reason, some adjustments are made on the experimental setup before starting to the experiments. Firstly, all sides of the water tank that are not used for the access of laser or camera are enclosed by black paperboards in order to avoid the reflections caused by the water tank. Some shadow regions behind the airfoils are observed in the snapshots taken during the experiments but these are because of the difference of the refractive indices of wing models and water inside the tank. Moreover, before starting to each experiment, the environment is darkened in order for the camera to see the laser light effectively and to take clear snapshots. Besides, the distance between the camera and water tank is arranged such that the dimensions of the test section are approximately three times wider than the chord length of the airfoils. Parallelism of the camera lens with respect to the test section is also assured for all experiments. Additionally, the illumination plane is arranged such that the laser sheet crosses the wing model from its mid-span that is inside the water. Before the experiments, a calibration image is taken by the camera so the system is calibrated and the pixels are converted to the meters in order to calculate the velocities at each instant correctly. As mentioned before, in order not to have unwanted velocity vectors in the flow field caused by the unsteadiness of the water inside the tank, a minimum of fifteen minutes is waited before starting to the each experiment. And lastly, the mixture inside the water tank is checked before starting to each experiment in order to observe if the seeding particles precipitate in water or not. If the precipitation is observed, the mixture is simply stirred before starting to the experiment.

CHAPTER 5

RESULTS AND DISCUSSION

This chapter is devoted to the discussion and comparison of all the results obtained from the numerical simulations and PIV measurements of the baseline test cases (see Figure 3.10.1 and Table 3.10.1). The results of the rest of the test cases investigated are given in Appendix A section. It should be noted that all the results are presented for the sixth period of the motion for each studied case, where the impulsive effects of the motion are observed to disappear and periodical motions are obtained ([63], [66]). In this context, unless otherwise specified, the non-dimensional time $t/T=0$ corresponds to the beginning of the stroke at the beginning of the sixth period.

For the sake of convenience, this thesis chapter is divided into four main sections. In the first three sections, the results obtained from the numerical simulations and experimental visualizations of sinusoidal pure pitch, pure plunge and combined pitch-plunge motions of SD7003 and NACA0012 airfoils are analyzed and compared with each other in terms of the instantaneous flow topology, respectively. To be comparable with the 2-D results, a 2-D plane, which is identical with the illuminated plane in the experiments (see Section 4.2.1 for the details), is subtracted from the 3-D domain and 2-D flow field of this plane is analyzed. The effects of pitching and plunging amplitudes on different modes of the constant frequency sinusoidal hovering motion are also investigated in these sections. And in the last section, the mean aerodynamic force and moment coefficients, calculated numerically for each studied case, are presented and compared with each other in order to investigate the highest lift, the lowest drag and the highest moment producing cases.

5.1 Results of the Pure Pitch Motion Case

5.1.1 SD7003 Airfoil Undergoing Pure Pitch Motion

In Figure 5.1.1 and Figure 5.1.2, the instantaneous vorticity contours obtained from the numerical and experimental studies of the purely pitching SD7003 airfoil with pitching amplitudes of 30^o and 45^o are presented, respectively. From the phenomenological point of view, the numerical and experimental results show similarity with each other in terms of instantaneous vorticity field generated around the airfoil for both cases. It can be said that the strength and duration of the vortices around the airfoil increases as the pitching amplitude increases from 30^o to 45^o. In Table 5.1.1 and Table 5.1.2, instantaneous maximum vorticity magnitudes of the LEVs and TEVs attached to the airfoil obtained from four different methods, which are 2-D CFD with fine grid, 2-D CFD with coarse grid, 3-D CFD and PIV, are given at different time instants. As it can be seen from these two tables, both the LEVs and TEVs are stronger in the case having $\alpha_a=45^o$ compared to the case having $\alpha_a=30^o$. From the contour graphs obtained, it is also observed that vortices dissipate faster as the pitching amplitude increases. The same phenomenon is also valid when considered the instantaneous vorticity contours of the case having $\alpha_a=10^o$ given in Appendix A.1.1 section. The vortices in the flow field of this lowest pitching amplitude case are clearly so weak and swiftly dissipate compared to the other two cases. Hence, it is possible to be said that the amplitude of the motion strongly affects the strength and duration of the vortices formed.

Phenomenologically, at t/T=0.0, CCW rotating (red) TEV formation around the airfoil is observed in the results of the numerical and experimental studies of both cases. In both cases, it is observed that this vortex form more or less at the same location considering the numerical and experimental results. Yet, the strength of it differs from one case to another as seen in Table 5.1.1 and Table 5.1.2. CW rotating (blue) detached TEV remaining from the previous period of the motion is also

observed at that time instant for both cases. Furthermore, at t/T=0.0, CCW rotating LEV, which is observed in all results of the both cases, form in the flow. It is clear that it is stronger in the 2-D CFD cases compared to the 3-D CFD and PIV results. The possible reason of this phenomenon is thought to be three-dimensional effects existing in the experiments and 3-D CFD simulations. Wing tip losses, which cannot be modeled in the 2-D CFD simulations, can be considered as a three-dimensional effect. They have an effect on the formation of the trailing edge vortices. At t/T=0.2, all CCW rotating TEV observed at t/T=0.0 starts detaching from the airfoil and it completely detaches at t/T=0.4. Following this, a CW rotating TEV develops over the airfoil, observed in all results of the studied cases. The CW rotating TEV detached from the airfoil starts to be washed out by the free stream after t/T=0.4 and henceforth the lift coefficient of both cases follows a decreasing trend until t/T=0.6. From t/T=0.4 to t/T=0.6, CCW rotating LEV dissipates too. When reached to t/T=0.8, new CCW rotating TEV and LEV form over the airfoil, which are again stronger in the case having $\alpha_a=45^o$. It should be emphasized that the case having $\alpha_a=10^o$ does not have any LEV formation, which is believed to have a significant effect on the mean lift coefficient of this case.

For each investigated case, it is observed that the vortices observed in the results of the experimental visualizations dissipate faster than those observed in the results of the numerical simulations mainly due to the three-dimensional effects presented in the experiments. Since three-dimensional effects also exist in the 3-D CFD simulations, this phenomenon is also observed in 3-D CFD results. Mainly because of the meshing strategies of the 3-D grid domain and various experimental conditions that could not be modeled by numerically, the results of these two solutions are not exactly the same but very close to each other. Moreover, it is also noticeable that the domain resolution, which can be defined as the number of vectors defining the velocity field, has an important effect on the formation of the vortices. There are 7326 velocity field vectors in the PIV measurements whereas this number is 128000 for 2-D CFD with fine grid, almost seventeen times more. Because of this, vortices exist in the flow field of the 2-D CFD with fine grid case are stronger than vortices exist in the flow field of the 3-D CFD and PIV cases. However, 2-D CFD with

coarse grid case has only 7384 velocity field vectors, which is very close to the number of velocity field vectors existing in the PIV measurements. Hence, the results of this case are closer to the experimental results and also to the 3-D CFD results.

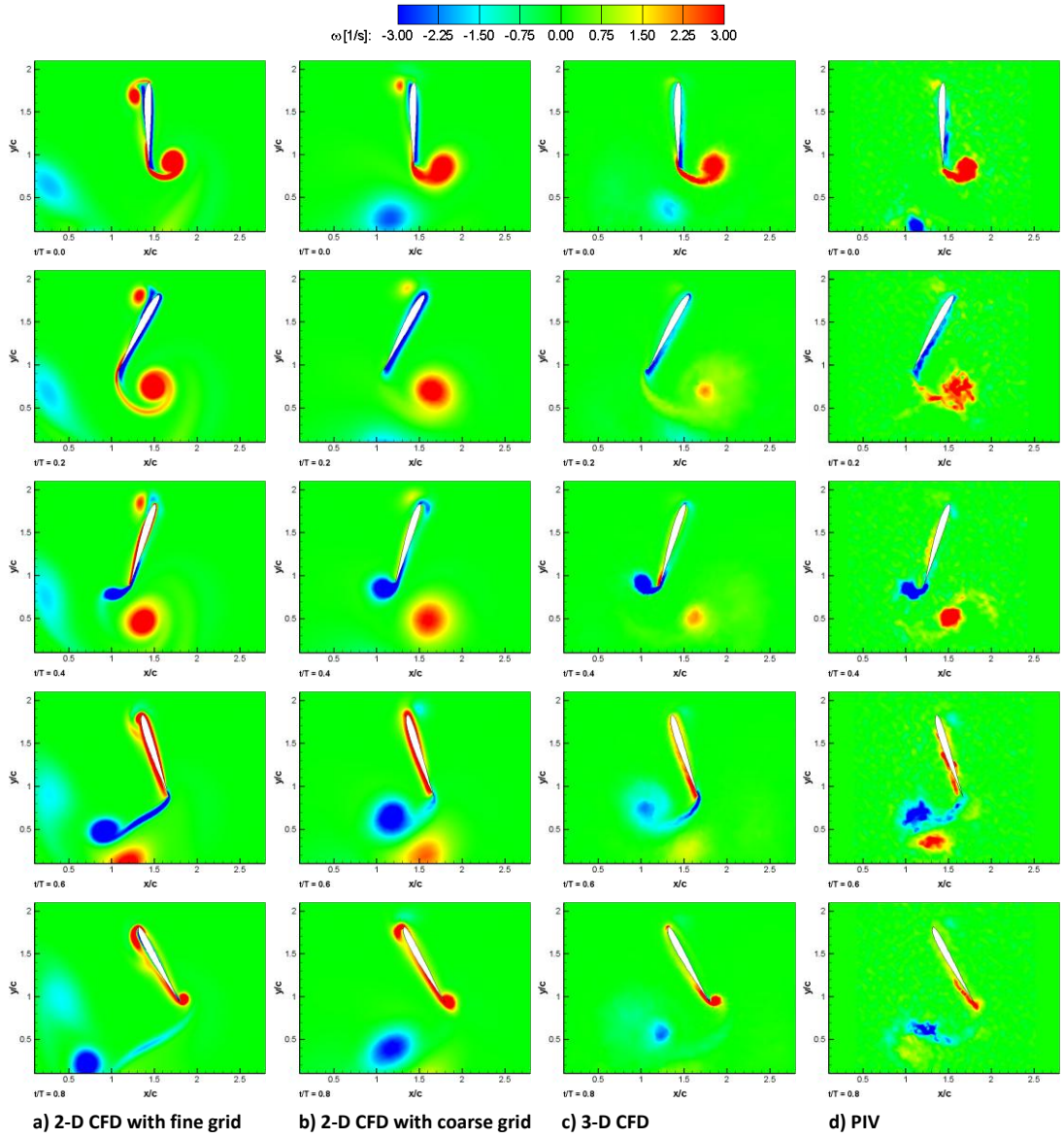

Figure 5.1.1 Instantaneous vorticity contours for purely pitching ($\alpha_a=30^o$; $k=3.8$) SD7003 airfoil.

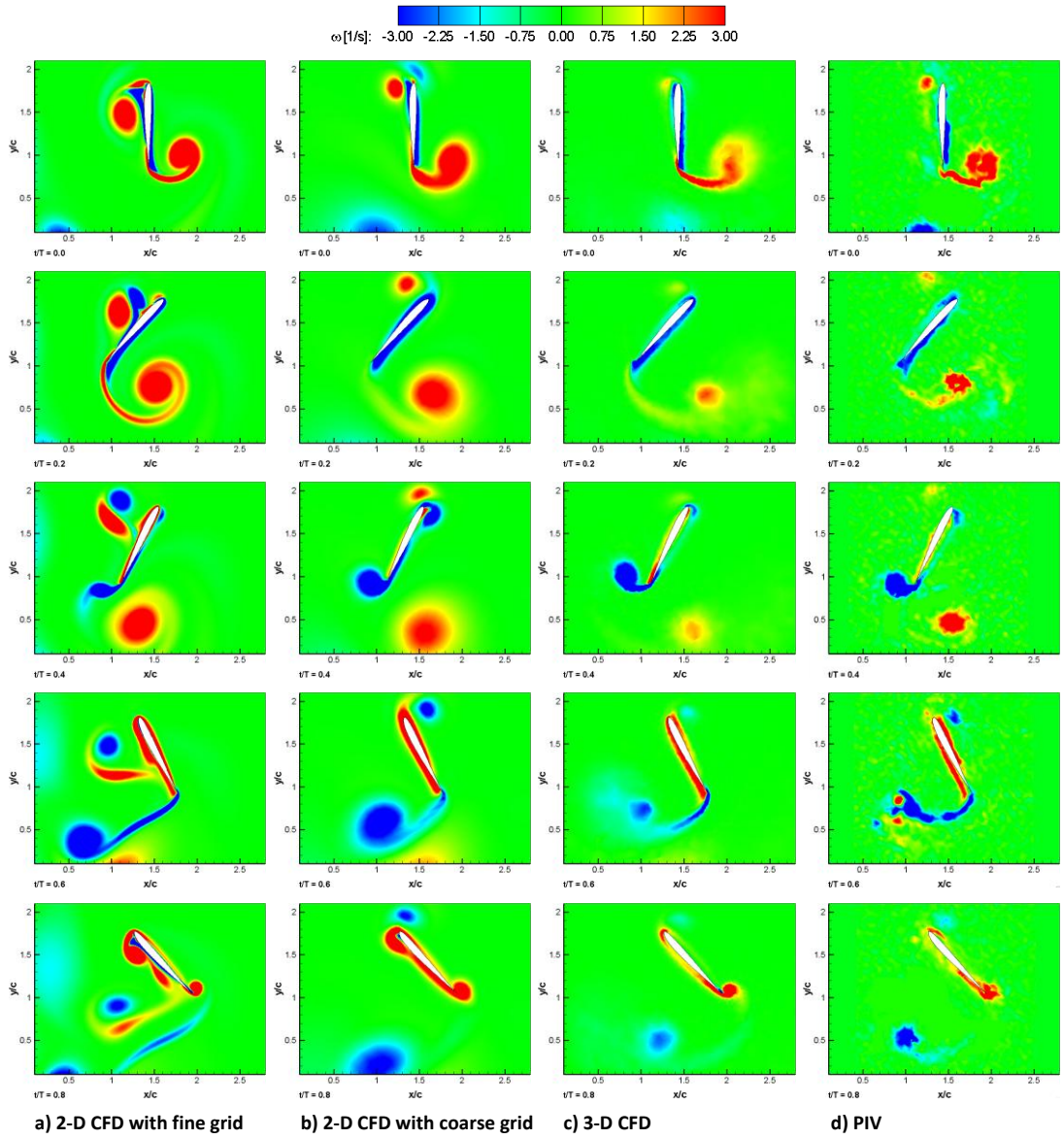

Figure 5.1.2 Instantaneous vorticity contours for purely pitching ($\alpha_a=45^o$; $k=2.5$) SD7003 airfoil.

The flow phenomenon figured out in the forward flapping flight studies of Jones and Platzer ([60], [82]) is also observed in the cases having $\alpha_a=30^o$ and $\alpha_a=45^o$. In other words, the vortex street behind the airfoil is deflected towards upstream indicating a lift generation. This phenomenon is clearly observed from t/T=0.6 to t/T=0.8. The lift coefficients of both cases also increase during that time. A positive mean lift coefficient is also calculated from the lift coefficient curves of these two cases, which also indicates a lift generation of the airfoils for the overall motion.

Table 5.1.1 Comparison of the instantaneous maximum vorticity magnitudes of LEVs and TEVs attached to the purely pitching ($\alpha_a=30^o$; $k=3.8$) SD7003 airfoil [1/s] (positive values indicate the CCW, negative values indicate the CW rotating vortices).

	2-D CFD with fine grid		**2-D CFD with coarse grid**		**3-D CFD**		**PIV**	
Vortex	*LEV*	*TEV*	*LEV*	*TEV*	*LEV*	*TEV*	*LEV*	*TEV*
t/T=0.0	4.57	8.40	2.70	5.86	0.92	5.59	1.59	5.72
t/T=0.2	-3.06	6.69	-2.85	4.69	-2.33	2.28	-2.26	4.45
t/T=0.4	-2.05	-10.25	-2.48	-8.65	-1.59	-8.80	-1.50	-9.12
t/T=0.6	5.40	-5.92	3.59	-4.23	1.77	-2.28	0.78	-4.38
t/T=0.8	6.24	9.41	5.27	8.92	3.27	8.65	1.01	7.45

Table 5.1.2 Comparison of the instantaneous maximum vorticity magnitudes of LEVs and TEVs attached to the purely pitching ($\alpha_a=45^o$; $k=2.5$) SD7003 airfoil [1/s] (positive values indicate the CCW, negative values indicate the CW rotating vortices).

	2-D CFD with fine grid		**2-D CFD with coarse grid**		**3-D CFD**		**PIV**	
Vortex	*LEV*	*TEV*	*LEV*	*TEV*	*LEV*	*TEV*	*LEV*	*TEV*
t/T=0.0	8.38	9.47	5.98	7.08	1.85	4.89	2.94	7.80
t/T=0.2	-6.01	7.82	-5.71	5.92	-3.45	2.45	-3.28	5.02
t/T=0.4	-3.39	-12.10	-4.06	-11.78	-2.67	-10.56	-2.73	-10.37
t/T=0.6	8.27	-6.61	7.70	-5.93	3.61	-3.44	3.19	-5.25
t/T=0.8	9.72	11.62	8.30	11.13	5.09	10.86	3.32	9.98

In Figure 5.1.3, instantaneous pressure coefficient contours of purely pitching ($\alpha_a=30^o$; $k=3.8$) SD7003 airfoil obtained from 2-D CFD calculations are presented. It should be noted that some pressure discontinuities are observed at the wake of the airfoil since no boundary condition is applied at those region. From t/T=0.0 to t/T=0.1, the influence of the overpressure region at the upper surface of the airfoil decreases and lift coefficient curve follows a decreasing trend during that time. Following this, pressure at the lower surface of the airfoil start to increase and this increase continues until t/T=0.36. As a result of this pressure increase, the lift

coefficient value also increases during t/T=0.1 to t/T=0.36. Lift coefficient reaches to its local maximum at t/T=0.36. From t/T=0.36 to t/T=0.5, pressure at the lower surface of the airfoil decreases and starting from t/T=0.6, pressure at the upper surface of the airfoil increases until the time instant t/T=0.8. The effect of these pressure changes, is also observed in the lift curve as a decreasing trend between t/T=0.36 and t/T=0.5 and as an increase between t/T=0.6 and t/T=0.8. After t/T=0.8, towards to the end of the motion, lift curve again goes into a decreasing trend.

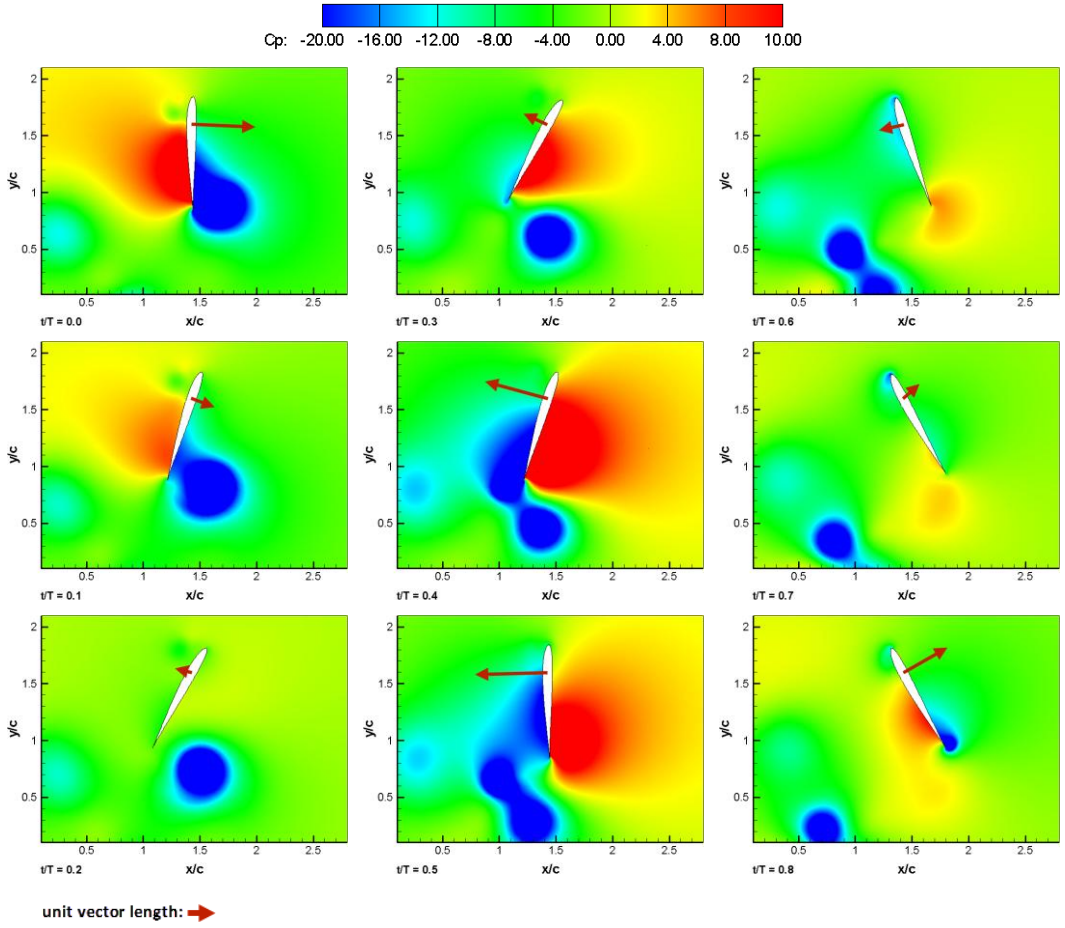

Figure 5.1.3 Instantaneous pressure coefficient (C_p) contours obtained from 2-D CFD for purely pitching ($\alpha_a=30^o$; $k=3.8$) SD7003 airfoil (vectors in *red color* denote the magnitude of instantaneous total force with its direction).

The instantaneous total forces vectors are also shown in Figure 5.1.3. From this figure, it is observed that the direction of the total force vector is always in the direction of the motion except at t/T=0.2 and t/T=0.7. Those two time instants are the

time instants after which the direction of the motion changes. At t/T=0.25 and t/T=0.75, the rotational velocities diminish to zero and consequently the magnitude of the total force vectors fall to zero. It is observed that the decrease of the total force magnitude from t/T=0.0 to t/T=0.15 make the drag coefficient to decrease too. After that time, total force vector changes its direction and its magnitude starts to increase until t/T=0.45. As a result, drag coefficient decreases further and local minimum drag coefficient occurs at t/T=0.45. Following this time, total force magnitudes follow a decreasing trend until t/T=0.65 and drag coefficient starts to increase. During t/T=0.15 to t/T=0.65, the drag coefficient is negative indicating a thrust producing behavior of the airfoil. After t/T=0.65, the total force vector changes its direction again and its magnitude increases until the end of the period. Starting from t/T=0.65, drag coefficients continues to increase and at t/T=0.95 drag coefficient reaches to its local maximum. Drag coefficient is positive during t/T=0.0 to t/T=0.15 and t/T=0.65 to t/T=1.0, which indicates a drag production. Considering the overall motion, the purely pitching ($\alpha_a=30^o$; $k=3.8$) SD7003 airfoil can be said to produce thrust.

Time histories of the aerodynamic force and moment coefficients and moment coefficient versus pitching angle distributions obtained from 2-D CFD simulations of purely pitching ($\alpha_a=30^o$; $k=3.8$ and $\alpha_a=45^o$; $k=2.5$) SD7003 airfoil are shown in Figure 5.1.4. The general trend of these curves is similar for both cases. It is noticed that moment coefficient curves show a very similar trend to the drag coefficient curves. It is also noticed that the drag forces highly dominate the flow. As it can be seen from this figure, there are small discrepancies between the results of the coarse and fine grid simulations. Yet, the mean values of the aerodynamics force and moment coefficients are nearly the same for these two solution methods. The difference between the mesh intensities of these domains is thought to play an important role on this phenomenon. The local minimum and maximum values occur nearly at the similar time instants in both cases. The local maximum value of the lift coefficient of the $\alpha_a=45^o$ case is greater than that of the $\alpha_a=30^o$ case; however, the $\alpha_a=45^o$ case has a smaller mean lift coefficient value compared to the $\alpha_a=30^o$ case considering the overall motion. On the other hand, the local minimum value of the drag coefficient of the $\alpha_a=30^o$ case are greater than that of $\alpha_a=45^o$ case; however the

$\alpha_a=30^o$ case has a smaller mean drag coefficient value, meaning to produce more thrust, compared to the $\alpha_a=45^o$ case considering the overall motion. The same phenomenon observed in the drag coefficients is also valid for the moment coefficients. A hysteresis type of graph is obtained from the moment coefficient versus pitching angle curves of two cases. During the first half of the downstroke, moment coefficient values of both cases decrease with an increase in the pitching angle indicating a stable motion. During the first half of the upstroke, pitching angle decreases and moment coefficient values of both cases further decrease, indicates an unstable motion. The second halves of the downstroke and upstroke exhibit the same phenomenon observed in the first halves of regarding to the stability, respectively.

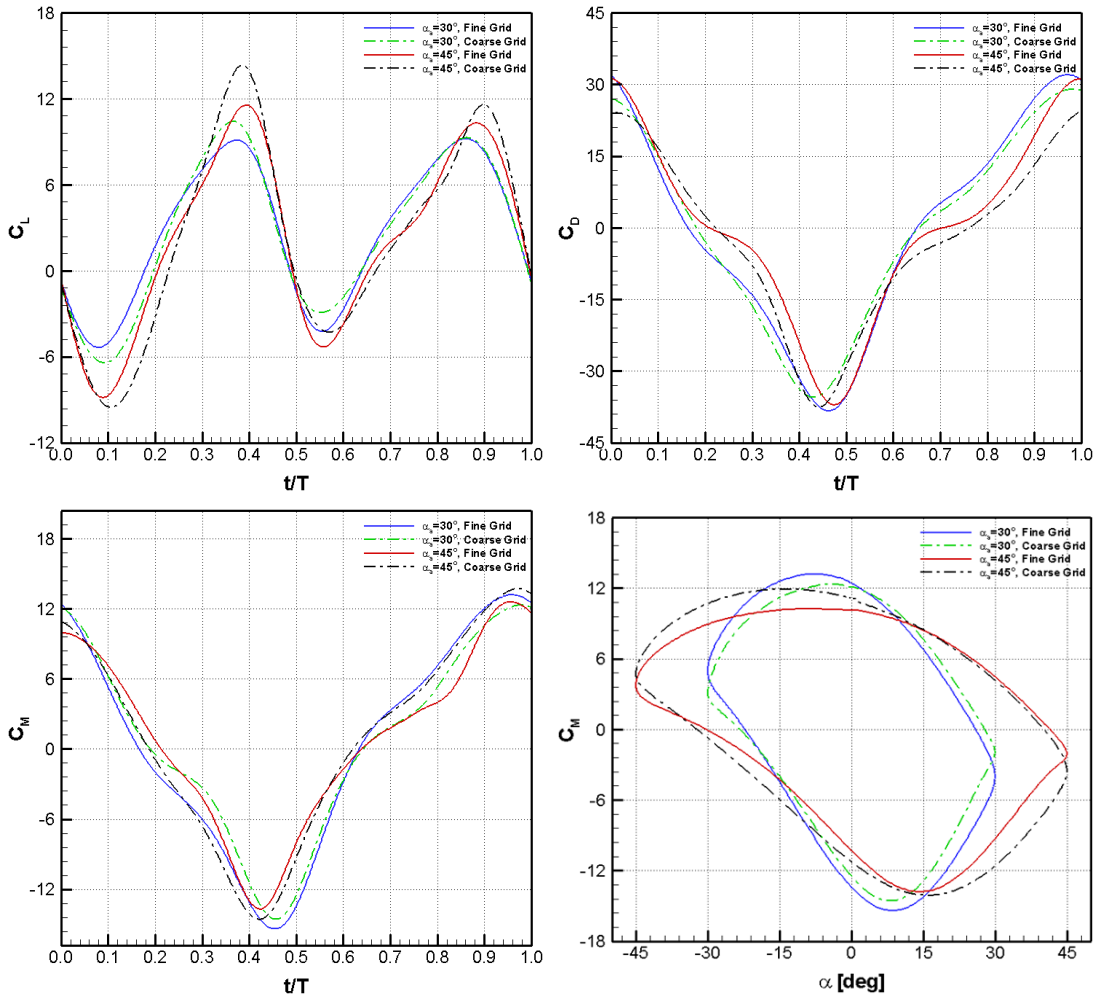

Figure 5.1.4 Time histories of lift, drag and moment coefficients and moment coefficient versus pitching angle distributions obtained from 2-D CFD for purely pitching ($\alpha_a=30^o$; $k=3.8$ and $\alpha_a=45^o$; $k=2.5$) SD7003 airfoil.

5.1.2 NACA0012 Airfoil Undergoing Pure Pitch Motion

The numerical and experimental results of the instantaneous vorticity contours of the purely pitching NACA0012 airfoil with $\alpha_a=30^o$ and $\alpha_a=45^o$ are shown in Figure 5.1.5 and Figure 5.1.6, respectively. As in the case of purely pitching SD7003 airfoil, there is also an agreement between the numerical and experimental results of both cases by means of the unsteady aerodynamics phenomenon occurring in the flow phenomenologically. As in the case of purely pitching SD7003 airfoil, vortices generated over the airfoil get stronger as the pitching amplitude increases. Table 5.1.3 and Table 5.1.4 have the information related to the instantaneous maximum vorticity magnitudes of the LEVs and TEVs attached to the airfoil obtained from the numerical simulations and experimental visualizations. The results presented in these tables figure out that the case having $\alpha_a=45^o$ have higher values of LEV and TEV magnitudes compared to the case having $\alpha_a=30^o$. Besides, the radius of the LEVs and TEVs generated in flow field of the case having $\alpha_a=45^o$ are greater than those for the case having $\alpha_a=30^o$. As in the case of purely pitching SD7003 airfoil, the case having $\alpha_a=10^o$ have a so weak vorticity field and vortices in the flow field of this case dissipate much faster compared to the other cases. The pitching amplitude again has an important effect on the strength and duration of the vortices generated.

Comparing the results obtained from two cases of the purely pitching NACA0012 airfoil with the results of the purely pitching SD7003 airfoil cases, the vortex generation mechanism of the flow is observed to be similar for each studied case. However, magnitudes of the vortices generated over the airfoils show some differences. Considering the results of the PIV measurements, it can be said that TEVs attached to the purely pitching ($\alpha_a=30^o$) NACA0012 airfoil are stronger than the those attached to the purely pitching ($\alpha_a=30^o$) SD7003 airfoil whereas LEVs attached to the airfoil are weaker in the purely pitching ($\alpha_a=45^o$) NACA0012 airfoil case compared to the same test case of the SD7003 airfoil. On the other hand, TEVs and LEVs attached to the purely pitching ($\alpha_a=45^o$) NACA0012 airfoil are stronger than those attached to the purely pitching ($\alpha_a=45^o$) SD7003 airfoil.

Similar to the purely pitching SD7003 airfoil cases, at the beginning of the period of both cases, CCW rotating (red) LEV and TEV formations are observed in the results of the numerical and experimental studies. As observed in the case of SD7003 airfoil, although the locations of these vortices are nearly the same for four different solutions, the maximum vorticity magnitudes of them differs as seen in Table 5.1.3 and Table 5.1.4. At t/T=0.2, CCW rotating TEV stops to grow and starts to detach from the airfoil in both cases. This vortex completely detach from the airfoil at t/T=0.4 and at that time CW rotating (blue) TEV develops over the airfoil of the both cases. From t/T=0.4 to t/T=0.6, CCW rotating detached TEV and LEV are washed out by the free stream and consequently the lift coefficient of both cases follows decreasing trend. Towards to the end of the period, at t/T=0.8, new CCW rotating TEV and LEV are generated over the airfoil. These vortices again have a stronger magnitudes in the case having $\alpha_a=45^o$.

As in the case of purely pitching SD7003 airfoil, the vortices observed in the results of the 3-D CFD simulations and PIV measurements dissipate faster than those observed in the results of the 2-D CFD simulations mainly due to three-dimensional effects existing. Furthermore, the difference observed between the magnitudes of the vortices obtained from the 2-D CFD with fine and coarse grid simulations of purely pitching SD7003 airfoil is also observed here. The results of the 2-D CFD with coarse grid simulations are closer to the experimental results.

Flow phenomenon observed in the test cases of purely pitching SD7003 airfoil, deflected vortex patterns behind the airfoil towards upstream indicating a lift generation, is also observed in purely pitching NACA0012 airfoil cases. Similar to the purely pitching SD7003 airfoil cases, during t/T=0.6 to t/T=0.8, this phenomenon is clearly observed. The lift coefficients of both cases, as a result, also increase during that time. Compared to the lift coefficients of the purely pitching SD7003 airfoil cases during t/T=0.6 to t/T=0.8, lift coefficients of the purely pitching NACA0012 airfoil cases during the same time instants are slightly smaller.

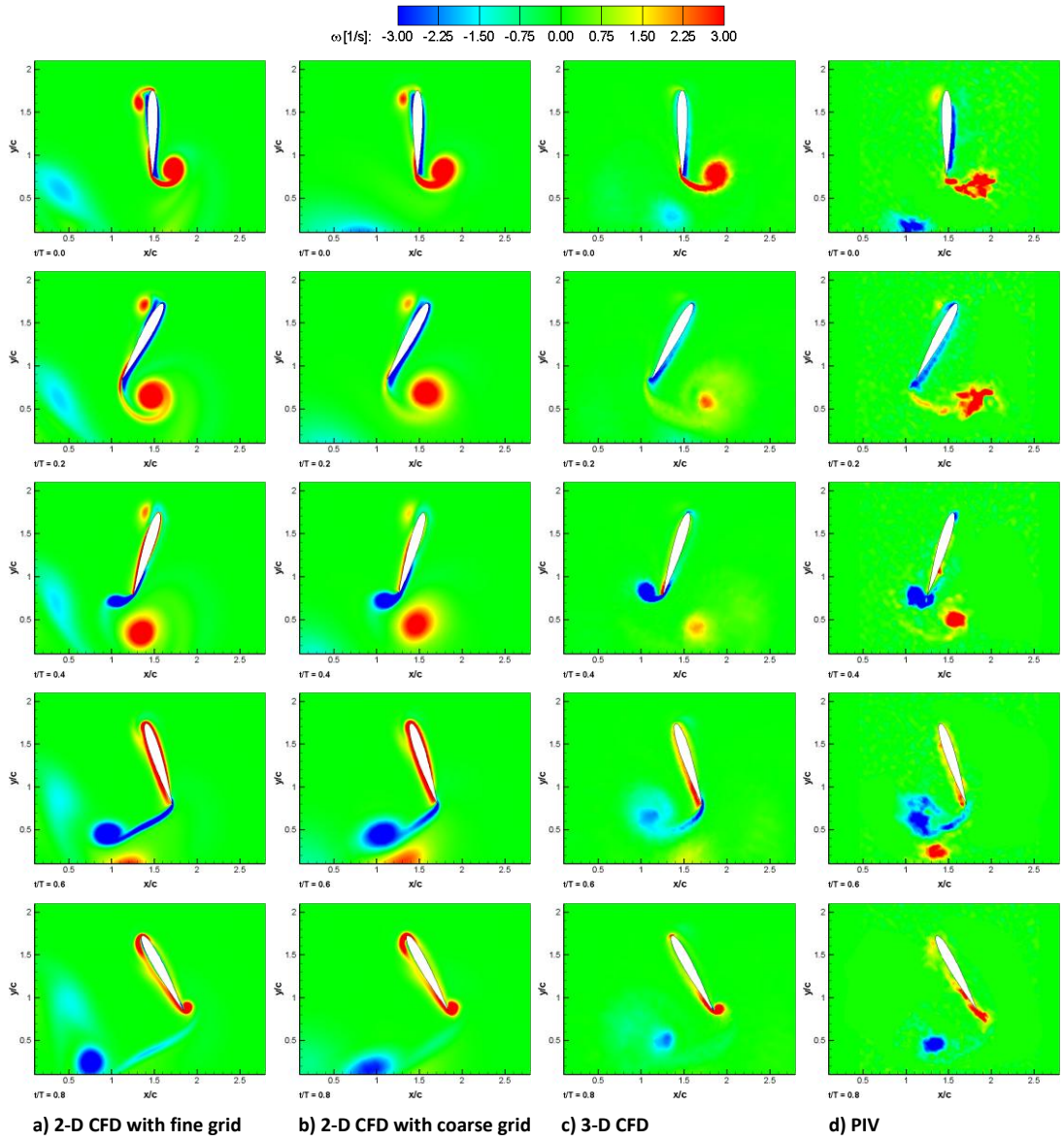

Figure 5.1.5 Instantaneous vorticity contours for purely pitching ($\alpha_a=30^o$; $k=3.8$) NACA0012 airfoil.

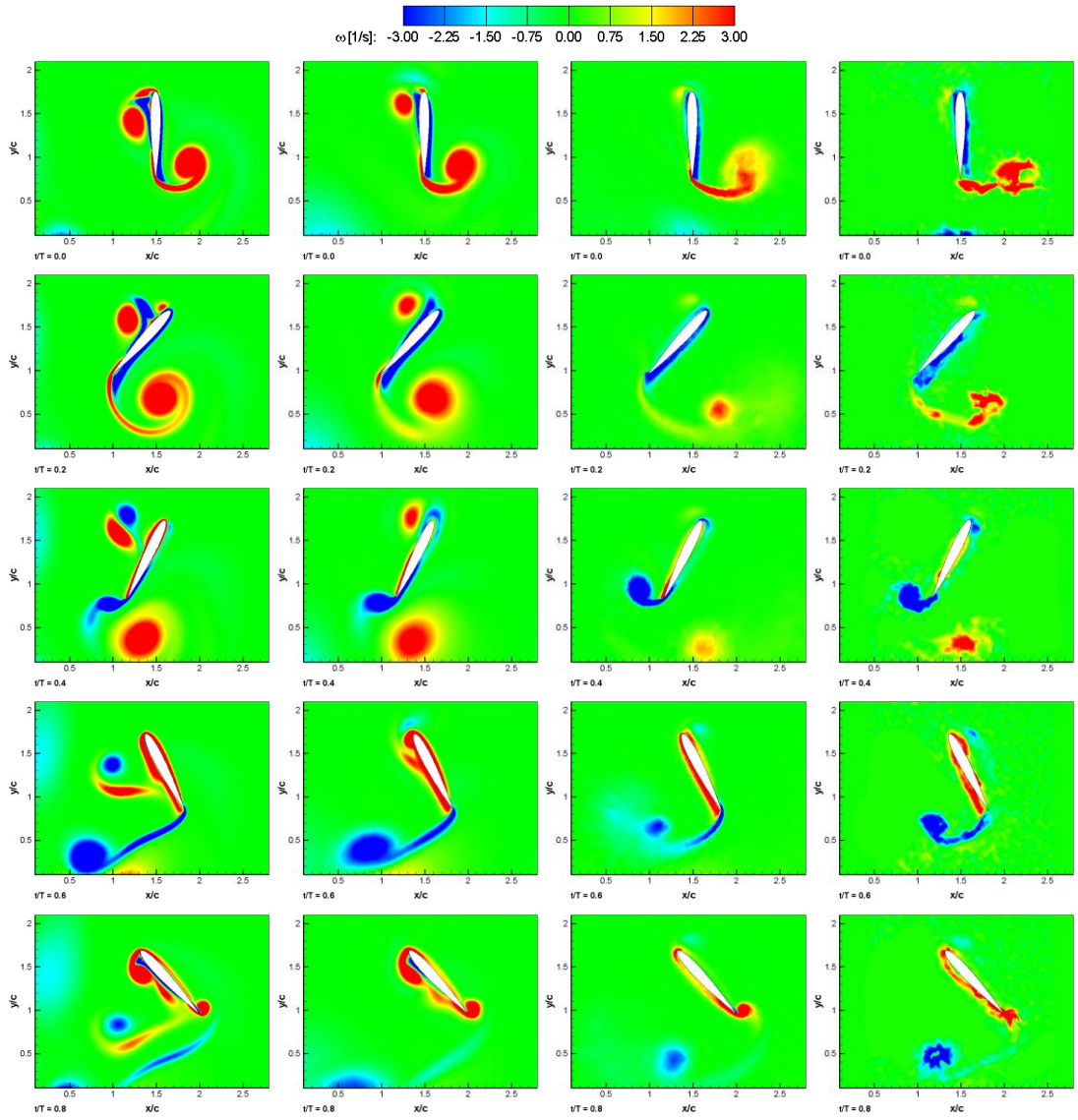

Figure 5.1.6 Instantaneous vorticity contours for purely pitching ($\alpha_a=45^o$; $k=2.5$) NACA0012 airfoil.

Table 5.1.3 Comparison of the instantaneous maximum vorticity magnitudes of LEVs and TEVs attached to the purely pitching ($\alpha_a=30^o$; $k=3.8$) NACA0012 airfoil [1/s] (positive values indicate the CCW, negative values indicate the CW rotating vortices).

	2-D CFD with fine grid		**2-D CFD with coarse grid**		**3-D CFD**		**PIV**	
Vortex	*LEV*	*TEV*	*LEV*	*TEV*	*LEV*	*TEV*	*LEV*	*TEV*
t/T=0.0	4.32	7.92	2.88	5.68	0.89	5.77	1.73	5.55
t/T=0.2	-2.86	6.35	-3.18	4.61	-1.96	2.17	-2.68	4.09
t/T=0.4	-1.76	-9.86	-1.02	-8.62	-1.32	-8.34	-2.14	-8.87
t/T=0.6	5.55	-5.98	4.18	-4.35	1.94	-2.65	1.32	-4.62
t/T=0.8	6.78	9.72	5.70	9.21	3.72	8.91	1.34	8.21

Table 5.1.4 Comparison of the instantaneous maximum vorticity magnitudes of LEVs and TEVs attached to the purely pitching ($\alpha_a=45^o$; $k=2.5$) NACA0012 airfoil [1/s] (positive values indicate the CCW, negative values indicate the CW rotating vortices).

	2-D CFD with fine grid		**2-D CFD with coarse grid**		**3-D CFD**		**PIV**	
Vortex	*LEV*	*TEV*	*LEV*	*TEV*	*LEV*	*TEV*	*LEV*	*TEV*
t/T=0.0	8.09	9.69	5.54	7.30	1.41	4.19	1.98	7.55
t/T=0.2	-7.41	8.14	-6.42	6.70	-3.83	2.94	-2.99	4.88
t/T=0.4	-2.01	-12.47	-2.69	-12.01	-2.27	-10.62	-2.78	-10.84
t/T=0.6	7.98	-6.78	7.67	-5.93	3.47	-3.65	3.29	-5.38
t/T=0.8	10.15	11.71	8.67	11.01	5.35	10.96	4.42	10.17

Instantaneous pressure coefficient contours of purely pitching ($\alpha_a=30^o$; $k=3.8$) NACA0012 airfoil obtained from 2-D CFD calculations are presented in Figure 5.1.7. A similar phenomenon observed in the purely pitching SD7003 airfoil case is also obtained for this case. In other words, the decrease in the effect of the overpressure region at the upper surface of the airfoil is observed during t/T=0.0 to t/T=0.1 resulting to a decrease in the lift coefficient values during that time. Following this, Pressure at the lower surface of the airfoil increases during t/T=0.1 to t/T=0.38 and consequently, the lift coefficient curve follows an increasing trend

during that time. In this case, the local maximum value of the lift coefficient occur at t/T=0.38. Between t/T=0.38 and t/T=0.5, the overpressure region at the lower surface of the airfoil decreases and shifts from the lower surface to the upper surface starting from t/T=0.6. After that time, overpressure region at the upper surface of the airfoil start to increase and this increase continues until t/T=0.8. These pressure changes observed over the airfoil makes the lift coefficient curve to follow a decreasing trend during t/T=0.38 to t/T=0.5 and an increasing trend during t/T=0.6 to t/T=0.8. After t/T=0.8, lift coefficient curve follows again a decreasing trend until the end of the motion.

In Figure 5.1.7, the instantaneous total force vectors are also presented. As in the case of purely pitching SD7003 airfoil, except at t/T=0.2 and t/T=0.7, the direction of the total force vector is in the direction of the motion. At the turning points of the motion, at t/T=0.25 and t/T=0.75, the rotational velocities fall to zero and as a result, the magnitude of the total force vectors fall to zero. Starting from the beginning of the period until t/T=0.15, magnitude of the total force vector and drag coefficient decrease. Following this time, total force vector changes its direction and its magnitude increases until t/T=0.45 resulting to the further decrease of the drag coefficient. The local minimum value of the drag coefficient occur at t/T=0.45 in this case too. Between t/T=0.45 and t/T=0.65, the magnitude of the total force vector decreases whereas the drag coefficient increases. Negative sign of the drag coefficient between t/T=0.15 and t/T=0.65 indicates a thrust production during that time period. At t/T=0.65, the total force vector changes its direction once more and its magnitude increases until the end of the period. The drag coefficient also tends to increase after t/T=0.65. Positive sing of the drag coefficient during t/T=0.0 to t/T=0.15 and t/T=0.65 to t/T=1.0 indicates the drag producing behavior of the airfoil. Considering the overall motion, the purely pitching ($\alpha_a=30^o;\ k=3.8$) NACA0012 airfoil can be said to produce thrust as purely pitching ($\alpha_a=30^o;\ k=3.8$) SD7003 airfoil.

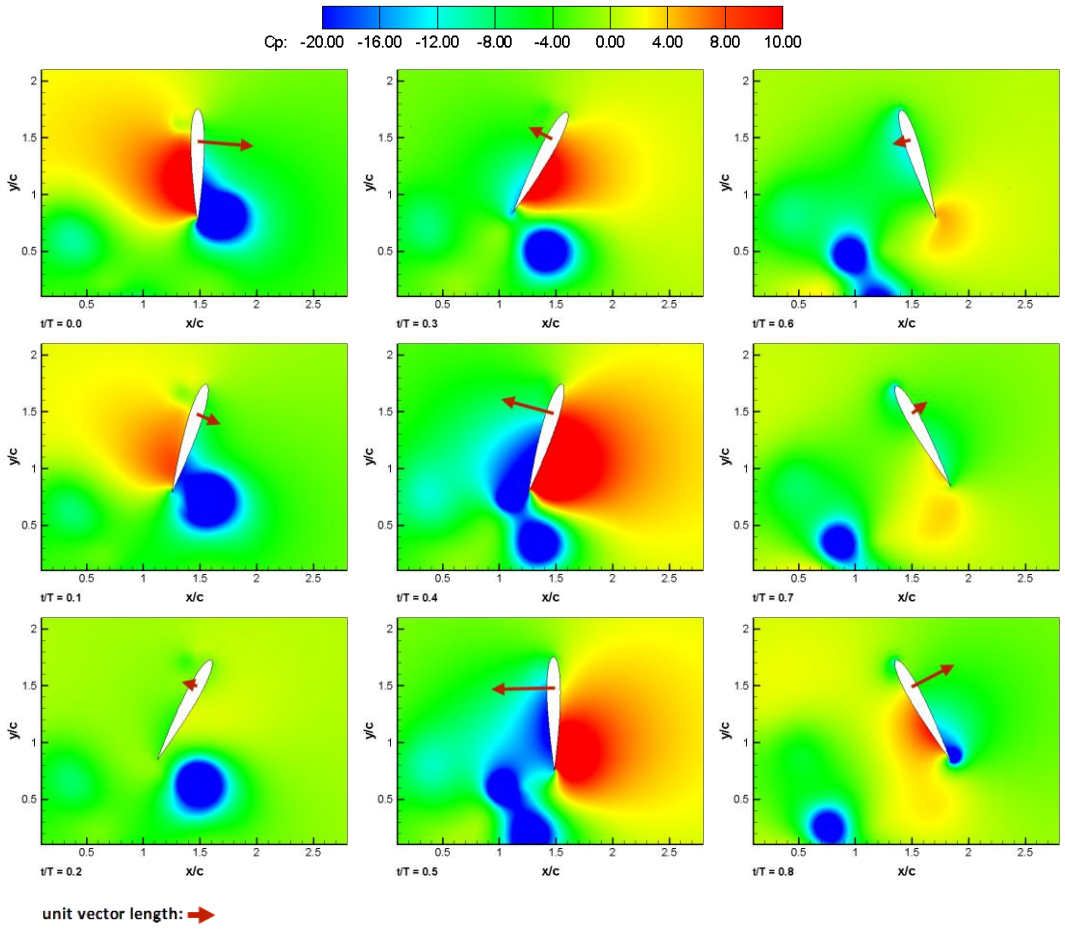

Figure 5.1.7 Instantaneous pressure coefficient (C_p) contours obtained from 2-D CFD for purely pitching ($\alpha_a=30^o$; $k=3.8$) NACA0012 airfoil (vectors in *red color* denote the magnitude of instantaneous total force with its direction).

Time histories of the aerodynamic force and moment coefficients and moment coefficient versus pitching angle distributions obtained from 2-D CFD simulations of purely pitching ($\alpha_a=30^o$; $k=3.8$ and $\alpha_a=45^o$; $k=2.5$) NACA0012 airfoil are shown in Figure 5.1.8. The general trend of each curve shows similarities with those of the SD7003 airfoil cases. Compared to the purely pitching SD7003 airfoil cases, purely pitching NACA0012 airfoil has smaller lift coefficient values whereas it has greater drag and moment coefficient values considering the each studied pure pitch motion case, the main reason of which is thought to be that the NACA0012 airfoil is a thicker airfoil compared to the SD7003 airfoil. As in the case of purely pitching SD7003 airfoil, small discrepancies occur between the results of the coarse and fine grid solutions mainly due to the difference in the mesh intensities of these two

domains. As in the case of purely pitching SD7003 airfoil, although the mean lift coefficient of the case having $\alpha_a=45^o$ is smaller considering the overall motion, the local maximum value of the lift coefficient of this case higher than that of the $\alpha_a=30^o$ case. On the other side, the mean drag coefficient of the $\alpha_a=30^o$ case is smaller than that of the $\alpha_a=45^o$ case, although the vice versa is valid for a comparison between the local minimum values of the drag coefficients of these two cases. Another hysteresis type of graph is obtained from the moment coefficient versus pitching angle curves of the purely pitching NACA0012 airfoil cases. The phenomena observed in the hysteresis graph of the moment coefficient of the purely pitching SD7003 airfoil cases are also valid for purely pitching NACA0012 airfoil cases.

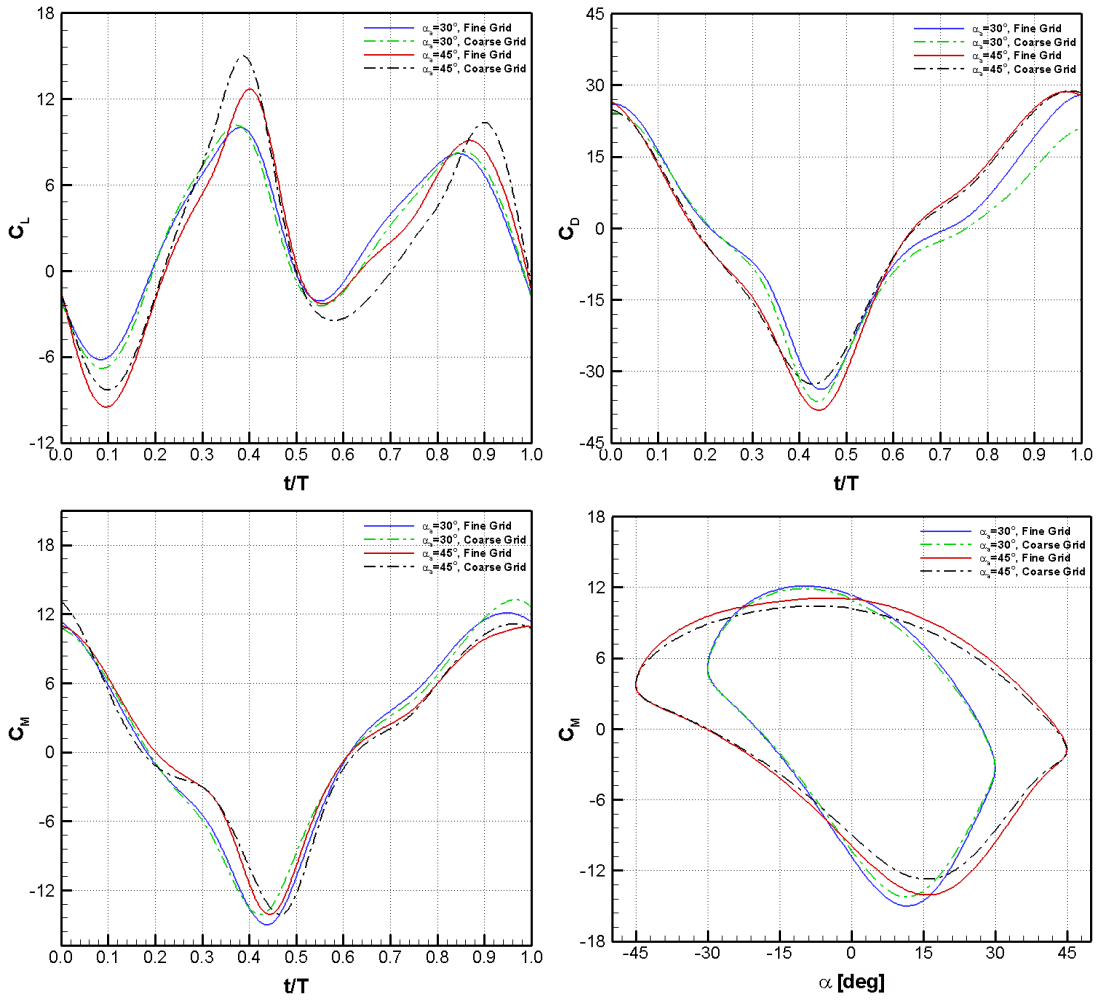

Figure 5.1.8 Time histories of lift, drag and moment coefficients and moment coefficient versus pitching angle distributions obtained from 2-D CFD for purely pitching ($\alpha_a=30^o$; $k=3.8$ and $\alpha_a=45^o$; $k=2.5$) NACA0012 airfoil.

5.2 Results of the Pure Plunge Motion Case

5.2.1 SD7003 Airfoil Undergoing Pure Plunge Motion

In Figure 5.2.1 and Figure 5.2.2, results of the numerical and experimental studies of the purely plunging SD7003 airfoil having plunging amplitudes of *0.01 m* and *0.02 m* are presented by means of the instantaneous vorticity contours, respectively. As in the case of purely pitching airfoils, the numerical and experimental results seem to agree with each other considering the type and location of the vortices observed in the flow field of the both cases. As expected, instantaneous maximum magnitude of the vortices around the airfoil and vortex core radii increase as the plunging amplitude increases from *0.01 m* to *0.02 m*. The same phenomena are also valid when the results of the purely pitching SD7003 airfoil case having plunging amplitude of *0.03 m* are considered, given in Appendix A.2.1 section. The vortices around the airfoil highly dominate the flow in this case and they dissipate slowly compared to the cases having lower plunging amplitudes. The instantaneous maximum vorticity magnitudes of the LEVs and TEVs attached to the airfoil, obtained from the numerical and experimental calculations, are presented in Table 5.2.1 and Table 5.2.2 at different time instants. As it can also be seen from these tables, the vortices observed in the case having plunging amplitude of *0.02 m* are stronger compared to the case having lowest plunging amplitude, *0.01 m*. It is clear to conclude that the strength and duration of the vortices are strongly affected by the amplitude of the pure plunge motion.

From the phenomenological point of view, at the beginning of the motion, CW rotating (blue) LEV formation over the airfoil is observed in the results of the numerical simulations and experimental visualizations of both cases. Although the size and location of this vortex is very close to each other as observed in the four different results of the case having x_a*=0.01 m*, it differs from each other considering the numerical and experimental studies carried out for the case having x_a*=0.02 m*. At

the same time instant, a CCW rotating (red) LEV, remaining from the previous period of the motion, is also observed in the results of both cases. It is observed that the CCW rotating detached LEV is observed to be weaker in the 3-D CFD and PIV results compared to 2-D CFD results. A CCW rotating TEV is also observed in the results of both cases at t/T=0.0. The same phenomenon related to the CW rotating LEV can also be said for this vortex. CW rotating LEV detaches from the airfoil at t/T=0.2 and following this, a CCW rotating LEV forms over the airfoil as observed in all results of studied cases. CCW rotating TEV, on the other hand, start detaching from the airfoil at t/T=0.2 and it completely detaches at t/T=0.4, which is again observed in all results. Similarly, a CW rotating TEV forms over the airfoil following this detachment. The detached LEV and TEV are suddenly washed out by the free stream in the case of $x_a=0.01\ m$ while they stay in the flow longer in the case of $x_a=0.02\ m$. At t/T=0.6, LEV and TEV formed at t/T=0.4 grow against the direction of motion and henceforth the drag coefficient curves follow an increasing trend for both cases. When reached to t/T=0.8, these LEV and TEV detach from the airfoil and new LEV and TEV form over the airfoils as observed in both cases.

Considering the results obtained from the numerical and experimental studies of pure plunge motion cases of SD7003 airfoil, it is observed that the results of the 3-D CFD simulations are closer to the PIV measurements. The main reason of this is thought to be the three-dimensional effects existing. It is also note that he vortices observed in the 3-D CFD simulations dissipates more quickly compared to the other cases. Moreover, results of the 2-D CFD with fine grid studies differ from that of the 2-D CFD with coarse grid studies, especially observed in the results of the case having $x_a=0.02\ m$. The domain resolution, which is very close to each other for 2-D CFD with coarse grid and PIV calculations as discussed in pure pitch motion cases, can also be said to affect the results of this case too. It can be concluded that the more intense the domain, the more complex vortex field, i.e. a vortex field highly dominated with the vortices remaining from the previous period, exists in the flow. This effect is not very significant at low plunging amplitudes, yet as the plunging amplitude increases it starts to occur distinguishably in the flow field.

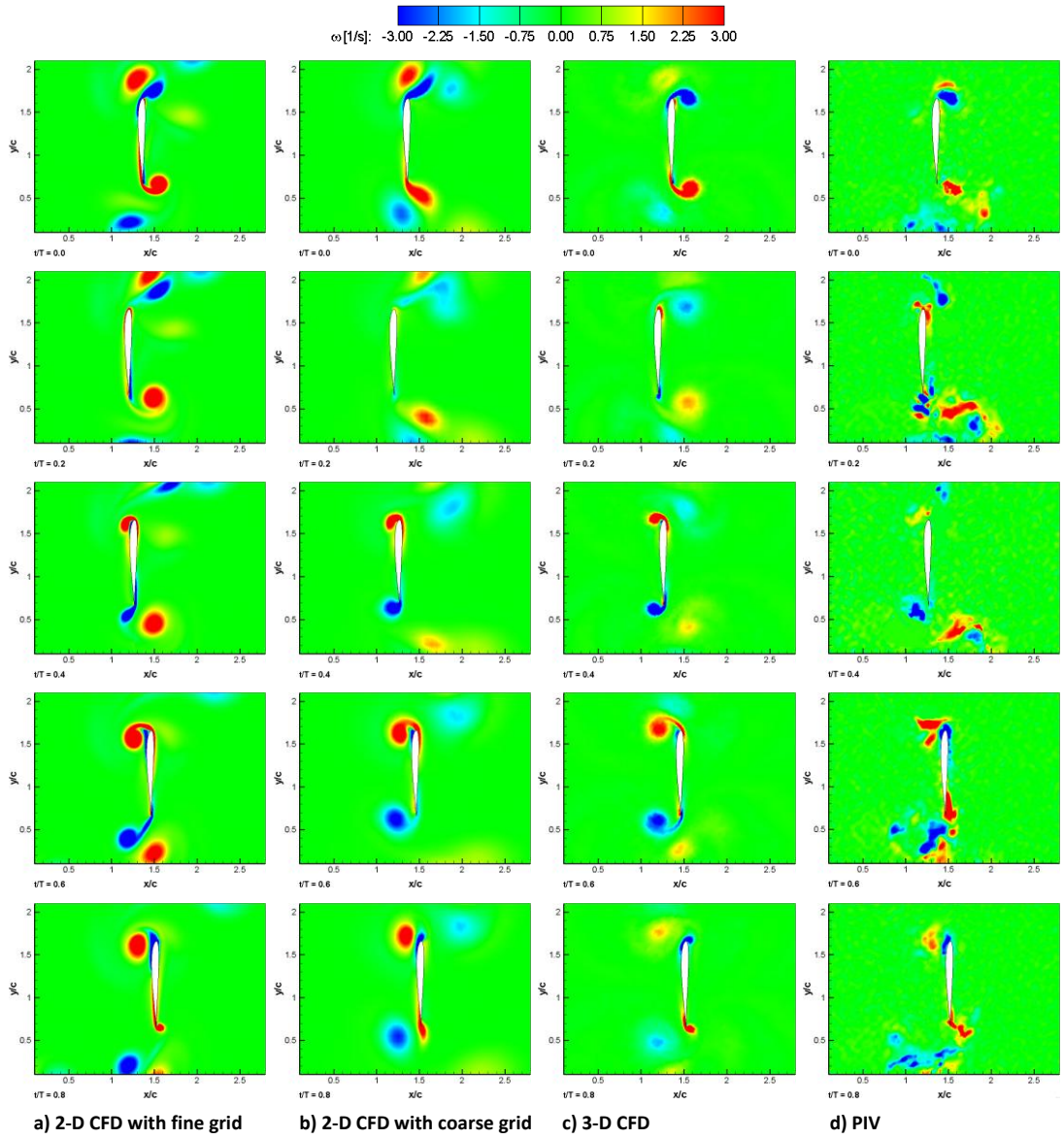

Figure 5.2.1 Instantaneous vorticity contours for purely plunging (x_a=*0.01 m; k=3.0*) SD7003 airfoil.

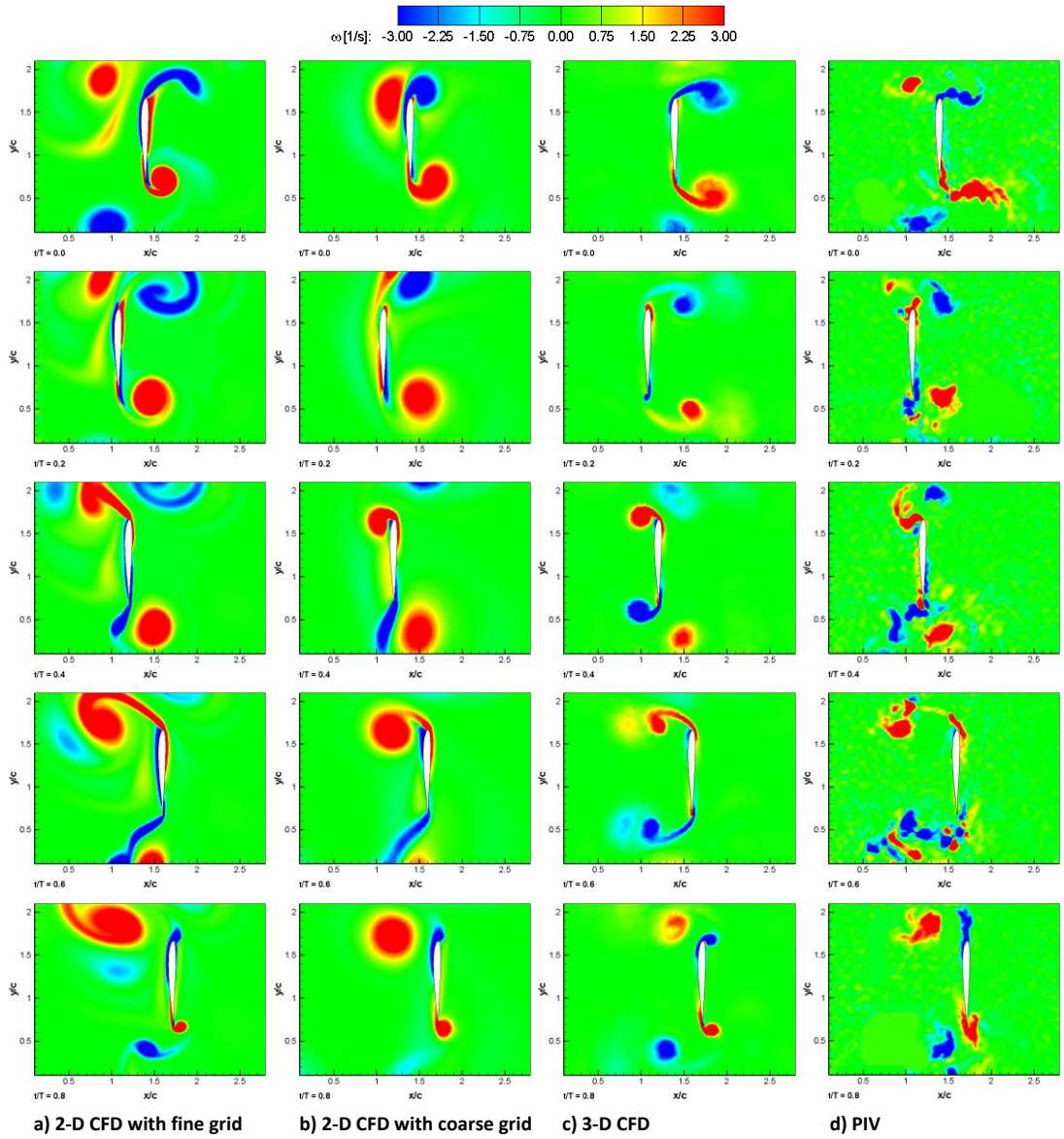

Figure 5.2.2 Instantaneous vorticity contours for purely plunging (x_a=*0.02 m; k=1.5*) SD7003 airfoil.

Table 5.2.1 Comparison of the instantaneous maximum vorticity magnitudes of LEVs and TEVs attached to the purely plunging (x_a*=0.01 m; k=3.0*) SD7003 airfoil [1/s] (positive values indicate the CCW, negative values indicate the CW rotating vortices).

	2-D CFD with fine grid		**2-D CFD with coarse grid**		**3-D CFD**		**PIV**	
Vortex	*LEV*	*TEV*	*LEV*	*TEV*	*LEV*	*TEV*	*LEV*	*TEV*
t/T=0.0	-7.04	6.87	-5.96	5.79	-5.67	6.38	-5.46	5.41
t/T=0.2	-5.58	5.54	-1.89	2.91	-2.19	2.07	-4.38	4.17
t/T=0.4	8.27	-7.28	6.77	-6.12	6.91	-6.41	2.21	-5.26
t/T=0.6	6.89	-5.63	5.42	-4.16	3.31	-3.15	5.31	-4.21
t/T=0.8	-4.97	6.22	-4.80	5.82	-4.73	5.78	-4.34	5.41

Table 5.2.2 Comparison of the instantaneous maximum vorticity magnitudes of LEVs and TEVs attached to the purely plunging (x_a*=0.02 m; k=1.5*) SD7003 airfoil [1/s] (positive values indicate the CCW, negative values indicate the CW rotating vortices).

	2-D CFD with fine grid		**2-D CFD with coarse grid**		**3-D CFD**		**PIV**	
Vortex	*LEV*	*TEV*	*LEV*	*TEV*	*LEV*	*TEV*	*LEV*	*TEV*
t/T=0.0	-9.18	11.15	-8.85	9.11	-6.87	7.92	-7.11	6.89
t/T=0.2	-6.61	9.34	-6.77	8.92	-4.54	4.84	-5.25	4.94
t/T=0.4	10.04	-9.15	9.19	-8.97	8.07	-8.01	7.56	-7.19
t/T=0.6	8.79	-7.01	8.25	-4.85	5.02	-4.95	5.63	-5.27
t/T=0.8	-6.42	9.02	-5.92	8.84	-5.35	8.68	-5.69	8.22

Instantaneous pressure coefficient contours of purely plunging (x_a*=0.02 m; k=1.5*) SD7003 airfoil obtained from the 2-D CFD calculations are presented in Figure 5.2.3. As time goes from t/T=0.0 to t/T=0.15, pressure side of the airfoil changes its location from the upper surface to the lower surface as the airfoil start to move from its initial position towards left and as a result, lift coefficient curve follows a decreasing trend during that time. Following this, overpressure region at the lower surface of the airfoil increases until t/T=0.45 resulting to an increase in the lift coefficient during t/T=0.15 to t/T=0.45 too. The local maximum value of the lift

coefficient occur at t/T=0.45. From t/T=0.45 to t/T=0.7, pressure at the lower surface of the airfoil start to decrease as the airfoil moves from left to right and consequently the lift coefficient curve goes into a decreasing trend. Starting from t/T=0.7, pressure at the upper surface of the airfoil increases and airfoil changes its direction of motion at t/T=0.75 and after that time it goes towards its initial position. As a result, the lift coefficient curve follows again an increasing trend during t/T=0.7 to t/T=0.9.

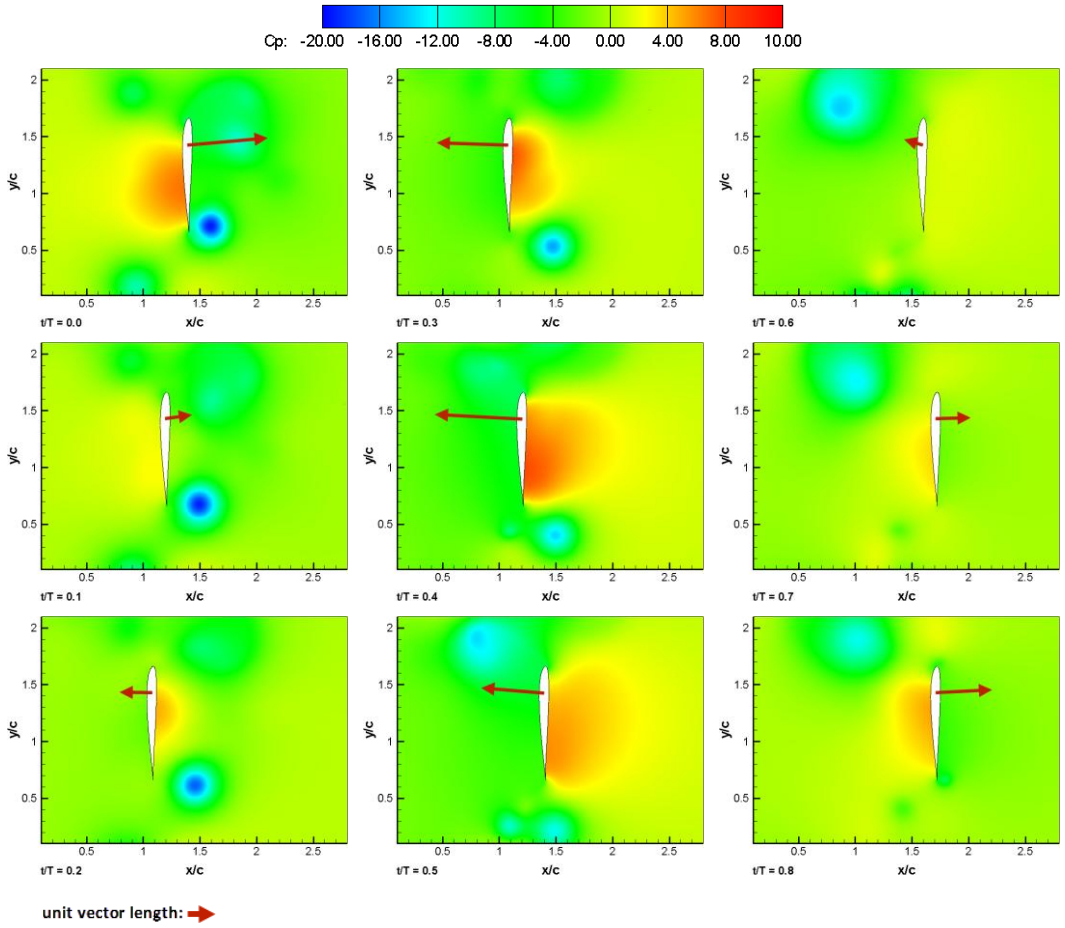

Figure 5.2.3 Instantaneous pressure coefficient (C_p) contours obtained from 2-D CFD for purely plunging (x_a*=0.02 m; k=1.5*) SD7003 airfoil (vectors in *red color* denote the magnitude of instantaneous total force with its direction).

The instantaneous total force vectors are also shown in Figure 5.2.3. Except at t/T=0.2 and t/T=0.7, after which the direction of motion changes, the total force vector is always in the opposite direction of the motion being different from the pure pitch motion cases. At t/T=0.25 and t/T=0.75, the axial velocities diminishes to zero

and consequently the magnitude of the total force vectors at that instants fall to zero. The magnitude of the total force vector decreases from t/T=0.0 to t/T=1 and it falls to zero at t/T=0.15. Following this, total force vector changes its direction and its magnitude start to increase until t/T=0.4. During that time period, from t/T=0.0 to t/T=0.4, drag coefficient curve also follow a decreasing trend. After that time, magnitude of the total force vector goes again towards zero and it falls to zero at t/T=0.65. Following this time, direction of the total force vector changes once more time and magnitude of the total force vector increases until the end of motion. The changes in the total force vector makes the drag coefficient to increase during t/T=0.4 to t/T=0.95. Because the direction of motion and total force vector is opposite during the great majority of the period, mean drag coefficient value approaches to positive values. Mean drag coefficient of the present case is also larger compared to the purely pitching ($\alpha_a=30^o;\ k=3.8$) SD7003 airfoil case. Nevertheless, considering the overall motion the purely plunging ($x_a=0.02\ m;\ k=1.5$) SD7003 airfoil case can be said to be a thrust producing case.

In Figure 5.2.4, time histories of the aerodynamic force and moment coefficients and moment coefficient versus plunging distance distributions obtained from the 2-D CFD studies of the purely plunging ($x_a=0.01\ m;\ k=3.0$ and $x_a=0.02\ m;\ k=1.5$) SD7003 airfoil are presented. Although the general trend of the drag coefficient and moment coefficient curves are very close to each other for fine and coarse grid results, lift coefficient curves is observed to exhibit different behaviors between fine and coarse grid results. The drag forces highly dominate the flow in this case too. Considering the two studied cases of pure plunge motion of SD7003 airfoil, the local minimum and local maximum values of the lift coefficients are observed to occur at the similar time instants. The local maximum value of the lift coefficient and the mean lift coefficient of the case having $x_a=0.02\ m$ are smaller than the case having $x_a=0.01\ m$ whereas the local minimum value of the lift coefficient of the case $x_a=0.02\ m$ is greater than the case having $x_a=0.01\ m$. On the other hand, while the local minimum value of the drag coefficient and the mean drag coefficient of the $x_a=0.02\ m$ case are smaller, the local maximum value of the $x_a=0.02\ m$ case is greater than the $x_a=0.01\ m$ case. Similarly, the local maximum value of the moment

coefficient and the mean moment coefficient values are greater in the case of $x_a=0.02$ *m* whereas the local minimum value of the $x_a=0.02$ *m* case is smaller compared to that of the case $x_a=0.01$ *m*. A hysteresis type of graph for the moment coefficient versus plunging amplitude distributions observed in the pure pitch motion cases is also obtained from the purely plunging cases of SD7003 airfoil. The pure pitch motions of SD7003 airfoil are stable, the slope of the moment coefficient versus plunging amplitude curves are negative, during the first and second halves of the downstroke and upstroke, respectively whereas they are unstable, the slope of the moment coefficient versus plunging amplitude curves are positive, during the second and first halves of the downstroke and upstroke, respectively.

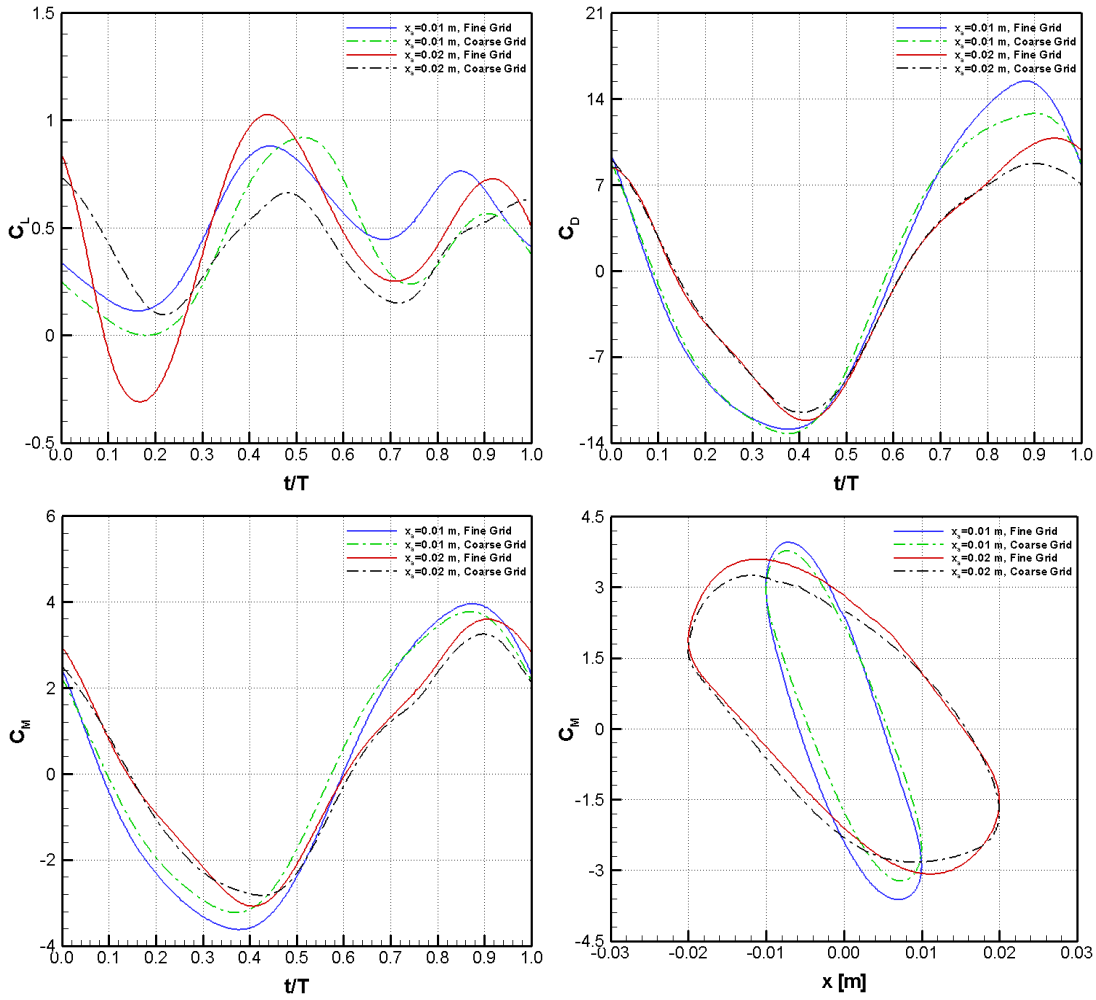

Figure 5.2.4 Time histories of lift, drag and moment coefficients and moment coefficient versus plunging distance distributions obtained from 2-D CFD for purely plunging ($x_a=0.01$ *m; k=3.0* and $x_a=0.02$ *m; k=1.5*) SD7003 airfoil.

5.2.2 NACA0012 Airfoil Undergoing Pure Plunge Motion

The numerical and experimental results of the instantaneous vorticity contours of the purely plunging (x_a=*0.01 m* and x_a=*0.02 m*) NACA0012 airfoil are given in Figure 5.2.5 and Figure 5.2.6, respectively. As in the case of previously discussed test cases, there is a phenomenological agreement between the results of the numerical and experimental studies in terms of the instantaneous vorticity field of the flow. As in the case of purely plunging SD7003 airfoil, as the plunging amplitude increases from *0.01 m* to *0.02 m* and from *0.02 m* to *0.03 m*, the size and dissipation rate of the vortices observed in the flow field also increases. The vortex core radii of the higher amplitude cases are clearly are bigger. In the case having the highest plunging amplitude among the studied cases, *0.03 m*, the flow field is highly dominated by the vortices around the airfoil and these vortices are observed to dissipate very slowly compared to the other cases. In Table 5.2.3 and Table 5.2.4, instantaneous maximum vorticity magnitudes of the LEVs and TEVs attached to the purely plunging NACA0012 airfoils are presented at different time instants. As it is expected, the vortices observed in the case having bigger plunging amplitude, *0.02 m*, are stronger than those observed in the case having plunging amplitude of *0.01 m*. Again, the formation and duration of the vortices around the airfoil are strongly affected by the amplitude of the motion.

Phenomenologically, instantaneous vortex topologies of the purely plunging NACA0012 airfoil cases show similarities with the cases of purely plunging SD7003 airfoil. Namely, at t/T=0.0, beginning of the motion, CW rotating (blue) LEV forms over the leading edge of the airfoil of the both cases. Considering the 2-D CFD with fine grid simulations and PIV visualizations, although vortex core radii of this vortex seem to be different, its magnitude is very close. The difference between the vortex core radii of the numerical and experimental studies increases as the plunging amplitude increases. At the same time instant, a CCW rotating (red) detached LEV formation, remaining from the previous period of the motion, is also observed in all cases. However, it is observed that the strength of this vortex is weaker in the results

of the 3-D CFD and PIV studies whereas it is stronger in the results of the 2-D CFD studies. A CCW rotating TEV formation is also observed in the results of both cases at the beginning of the period. Similar discussion related to the CW rotating LEV can also be said for this vortex. The CW rotating LEV, observed at the beginning of the period, detaches from the leading edge of the airfoil at t/T=0.2 and following this detachment, a CCW rotating LEV start to develop over the airfoil as observed in all results of the investigated cases. Meanwhile, CCW rotating TEV, observed at t/T=0.0, start to detach from the purely plunging airfoils at t/T=0.2 and it completely detaches from the airfoils at t/T=0.4. Just after this detachment, CW rotating TEV starts to form over the trailing edge of the airfoils. The LEV and TEV detached from the airfoil dissipate faster in $x_a=0.01\ m$ case compared to the $x_a=0.02\ m$ case. Besides, it is observed that the dissipation rate is higher in the 3-D CFD simulations as observed in both test cases. From t/T=0.4 to t/T=0.6, CCW rotating LEV and CW rotating TEV grow against the direction of motion and consequently, the drag coefficients increase during that time. Reaching to t/T=0.8, the growth LEV and TEV detach from the airfoil and at this time new formations of the CW rotating LEV and CCW rotating TEV are observed in the flow. After t/T=0.8, drag coefficients goes into a decreasing trend until the end of the period.

As in the case of purely plunging SD7003 airfoils, vortices are observed to dissipate faster in 3-D CFD simulations and PIV visualizations mainly due to the three-dimensionality effects. Moreover, the vortices over the airfoil show similarity with each other from the phenomenological point of view considering the 3-D CFD and PIV studies. On the other hand, there are some discrepancies observed between the results of the 2-D CFD simulations in terms of instantaneous vortex topologies of the flow. Especially in the case having plunging amplitude of *0.01 m*, results of the 2D CFD with coarse grid simulations exhibit similarities with the results of the 3-D CFD and PIV studies. Yet, considering the results of the case having *0.02 m*, 2-CFD results differ from the results of the other studies. It is observed that the vortices remaining from the previous periods of the motion highly dominate the flow field of the 2-D CFD with fine grid simulations in $x_a=0.02\ m$ case. This phenomenon is not very significant in the case having $x_a=0.01\ m$.

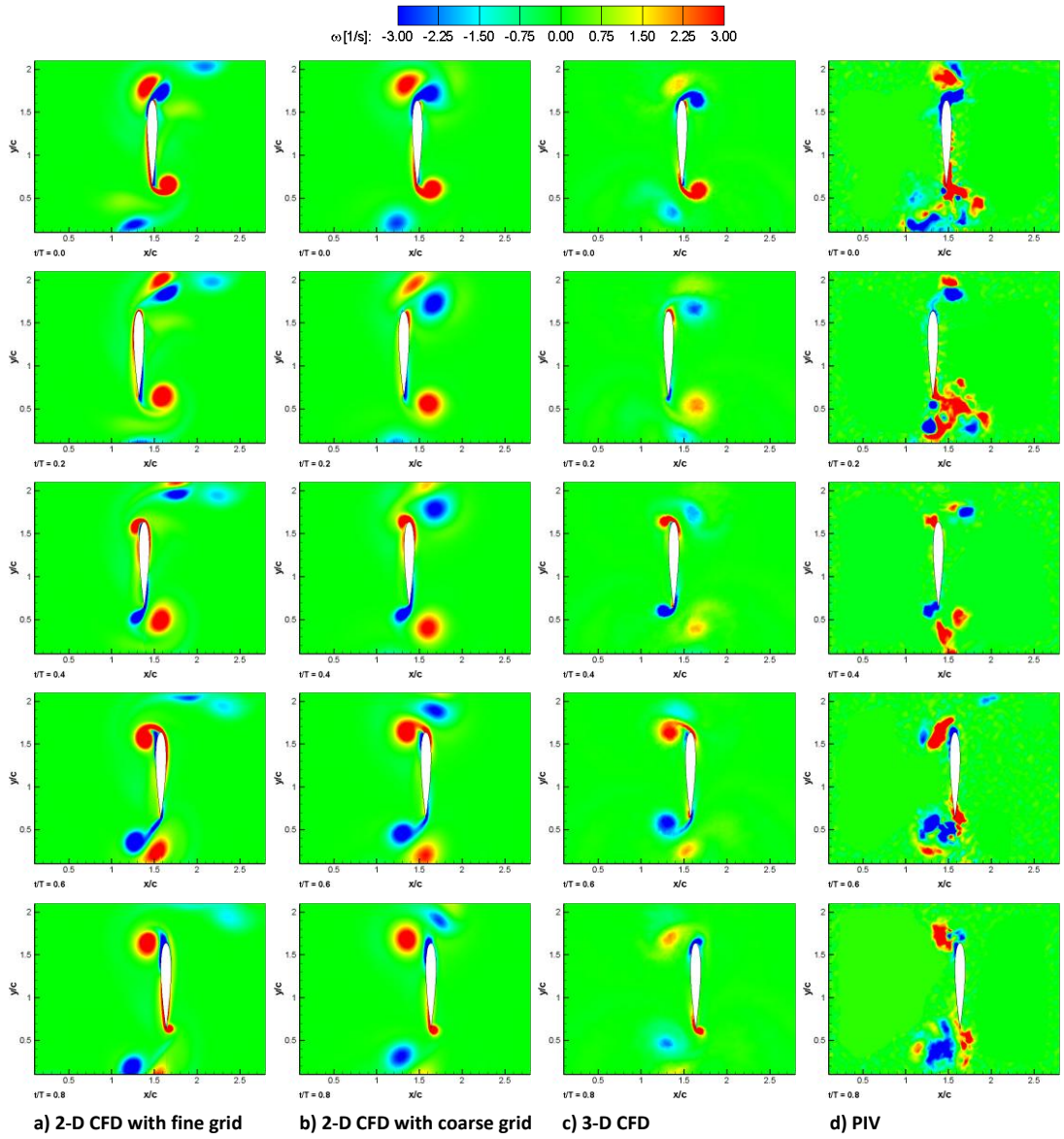

Figure 5.2.5 Instantaneous vorticity contours for purely plunging (x_a=*0.01 m; k=3.0*) NACA0012 airfoil.

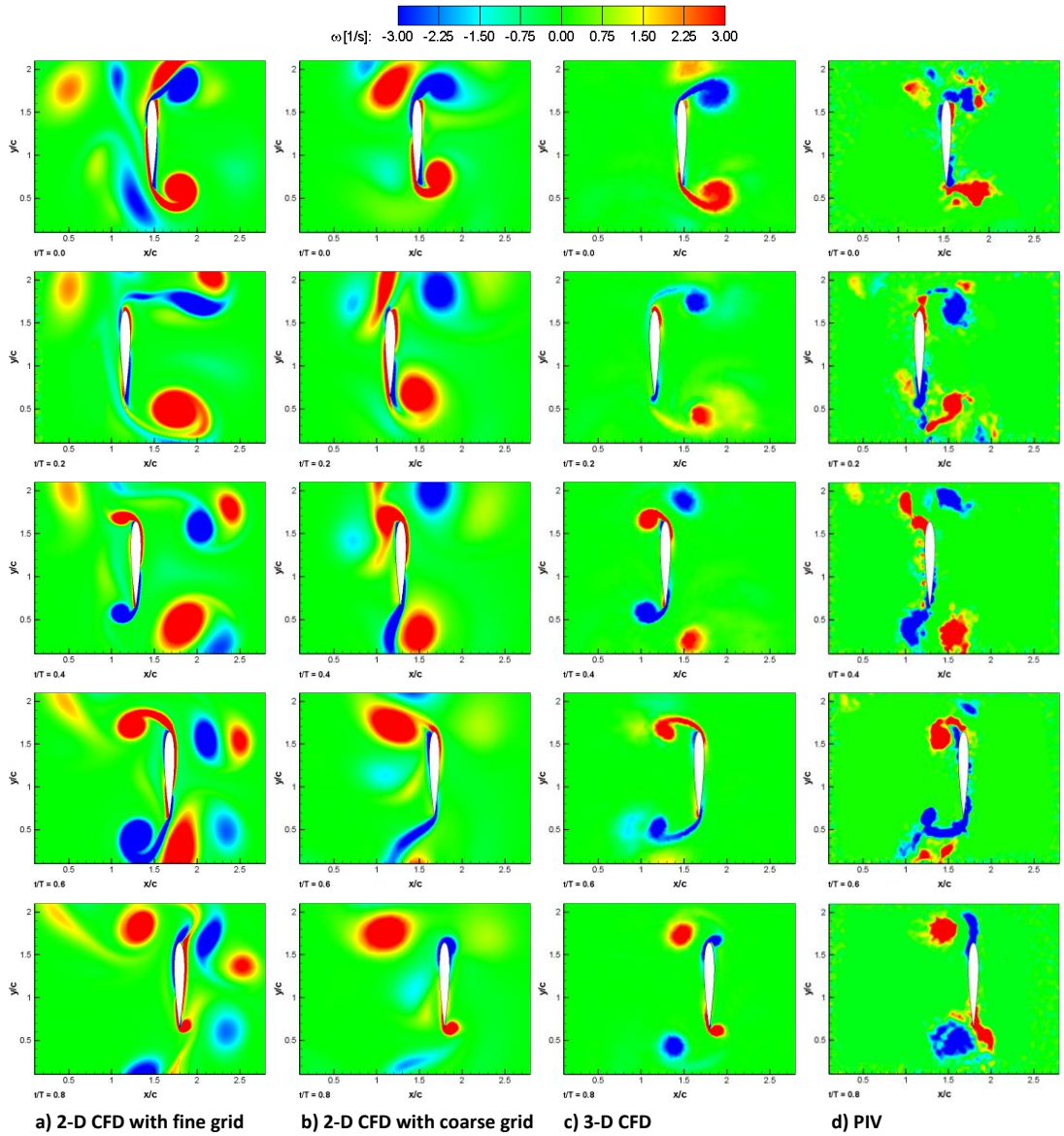

Figure 5.2.6 Instantaneous vorticity contours for purely plunging (x_a=*0.02 m; k=1.5*) NACA0012 airfoil.

Table 5.2.3 Comparison of the instantaneous maximum vorticity magnitudes of LEVs and TEVs attached to the purely plunging (x_a*=0.01 m; k=3.0*) NACA0012 airfoil [1/s] (positive values indicate the CCW, negative values indicate the CW rotating vortices).

	2-D CFD with fine grid		**2-D CFD with coarse grid**		**3-D CFD**		**PIV**	
Vortex	*LEV*	*TEV*	*LEV*	*TEV*	*LEV*	*TEV*	*LEV*	*TEV*
t/T=0.0	-8.23	6.77	-6.15	5.73	-6.57	6.39	-8.33	5.63
t/T=0.2	-6.18	5.75	-4.18	4.27	-2.58	2.34	-4.82	4.39
t/T=0.4	8.68	-7.87	7.03	-6.53	7.52	-7.25	4.74	-5.89
t/T=0.6	7.01	-5.70	5.65	-4.31	3.59	-3.46	5.62	-5.21
t/T=0.8	-5.28	6.38	-4.90	6.12	-4.52	6.05	-4.55	5.45

Table 5.2.4 Comparison of the instantaneous maximum vorticity magnitudes of LEVs and TEVs attached to the purely plunging (x_a*=0.02 m; k=1.5*) NACA0012 airfoil [1/s] (positive values indicate the CCW, negative values indicate the CW rotating vortices).

	2-D CFD with fine grid		**2-D CFD with coarse grid**		**3-D CFD**		**PIV**	
Vortex	*LEV*	*TEV*	*LEV*	*TEV*	*LEV*	*TEV*	*LEV*	*TEV*
t/T=0.0	-9.74	10.14	-7.41	8.98	-6.81	6.47	-9.08	9.62
t/T=0.2	-7.86	8.67	-7.21	6.96	-5.74	5.92	-8.55	6.01
t/T=0.4	10.09	-10.24	9.78	-9.84	8.42	-9.54	7.88	-9.21
t/T=0.6	8.27	-7.38	7.82	-2.77	7.65	-5.97	7.75	-6.39
t/T=0.8	-8.34	9.62	-7.14	9.40	-7.38	9.52	-7.85	10.02

In Figure 5.2.7, instantaneous pressure coefficient contours of purely plunging (x_a*=0.02 m; k=1.5*) NACA0012 airfoil obtained from 2-D CFD calculations are presented. From t/T=0.0 to t/T=0.15, the overpressure region at the upper surface of the airfoil decreases as the airfoil starts its movement towards left and consequently, lift coefficient goes into a decreasing trend during that time. The local minimum value of the lift coefficient occur at t/T=0.15. Following this time, the pressure at the lower surface of the airfoil increases continuing until t/T=0.45. The effect of this pressure increase is observed as an increase in the lift coefficient during t/T=0.15 to

t/T=0.45, at which the local maximum value of the lift coefficient occur. From t/T=0.45 to t/T=0.7, overpressure region at the lower surface of the airfoil start to decrease as the airfoil moves from left to right. As a result, the lift coefficient curve follows a decreasing trend. After t/T=0.7, overpressure region at the upper surface of the airfoil increases and airfoil changes its direction of motion at t/T=0.75 to go to its initial position. After that time, the lift coefficient curve follows again an increasing trend until t/T=0.9, after which it again goes into a decreasing trend.

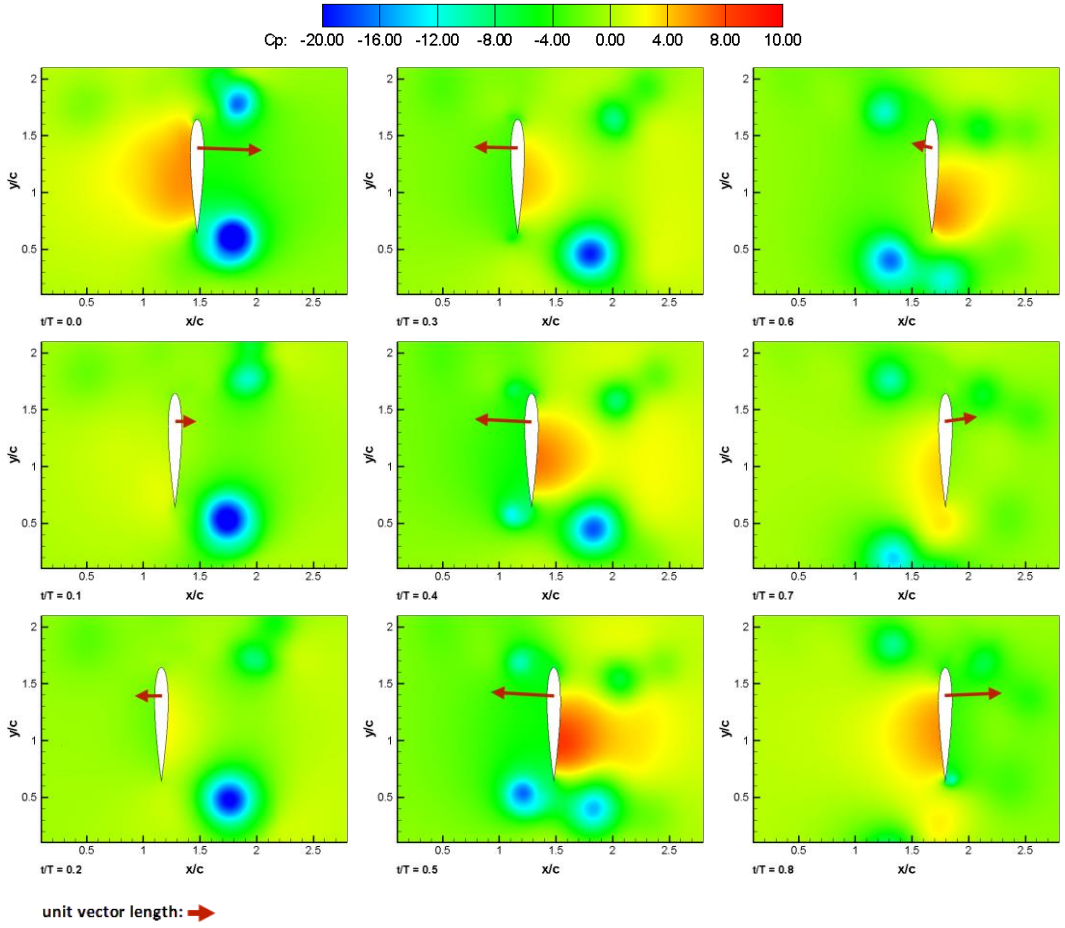

Figure 5.2.7 Instantaneous pressure coefficient (C_p) contours obtained from 2-D CFD for purely plunging (x_a*=0.02 m; k=1.5*) NACA0012 airfoil (vectors in *red color* denote the magnitude of instantaneous total force with its direction).

The instantaneous total force vectors are also shown in Figure 5.2.7. As in the case of purely plunging SD7003 airfoil, except at t/T=0.2 and t/T=0.7, after which the direction of motion changes, the total force vector is always in the opposite direction.

At t/T=0.25 and t/T=0.75, the axial velocities diminishes to zero and as a result of this, the magnitude of the total force vectors at that instants fall to zero. The magnitude of the total force vector decreases as time goes from t/T=0.0 to t/T=0.15, at which its magnitude falls to zero. Following this time, total force vector changes its direction and its magnitude start to increase continuing until t/T=0.4. As a result of the changes in the magnitude of the total force vector, drag coefficient decreases during t/T=0.0 to t/T=0.4. After t/T=0.4, magnitude of the total force vector decreases again it becomes zero at t/T=0.65. Just after t/T=0.65, direction of the total force vector changes again and its magnitude follows an increasing trend until the end of the motion. The effect of changes in the total force vector is observed as an increase in the drag coefficient values during t/T=0.4 to t/T=0.9. As in the case of purely plunging SD7003 airfoil, since the direction of motion and total force vector opposes each other during the whole the period, in general, mean drag coefficient value becomes positive indicating a drag producing behavior of the airfoil for the overall motion. Hence, mean drag coefficient of the present case is larger compared to the purely plunging ($x_a=0.02\ m$) SD7003 airfoil case.

Time histories of the aerodynamic force and moment coefficients and moment coefficient versus plunging distance distributions obtained from 2-D CFD studies of purely plunging ($x_a=0.01\ m;\ k=3.0$ and $x_a=0.02\ m;\ k=1.5$) NACA0012 airfoil are given in Figure 5.2.8. Although the general trend of the drag coefficient and moment coefficient curves are similar for the fine and coarse grid results, lift coefficient curves is observed to behave differently for those as in the case of purely plunging SD7003 airfoil. The flow field is highly dominated by the drag forces in this case too. The local maximum and minimum values of the aerodynamic force and moment coefficients of two studied cases occur nearly at the same time instants. However the maximum and minimum values of them differ for each studied case. Namely, the local maximum value of the lift coefficient and mean lift coefficient of the case having $x_a=0.01\ m$ are greater than the case having $x_a=0.02\ m$. On the other hand, the mean drag coefficient of the case having $x_a=0.01\ m$ is greater than the case having $x_a=0.02\ m$, the local minimum value of the drag coefficient of the case having the lowest plunging amplitude is smaller. Lastly, the local maximum value of the

moment coefficient and mean moment coefficient of the case having $x_a=0.02\ m$ are greater than the case having $x_a=0.01\ m$. A hysteresis type of graph for the moment coefficient versus plunging amplitude distributions observed in the results of the previously discussed test cases is also obtained from the purely plunging cases of NACA0012 airfoil. It is possible to conclude that the pure plunge motions of the NACA0012 airfoil are stable during the first and third quarters of the period, where the slope of the moment coefficient versus plunging amplitude curves are negative, whereas they are unstable during the rest of the period, where the slope of the moment coefficient versus plunging amplitude curves are positive.

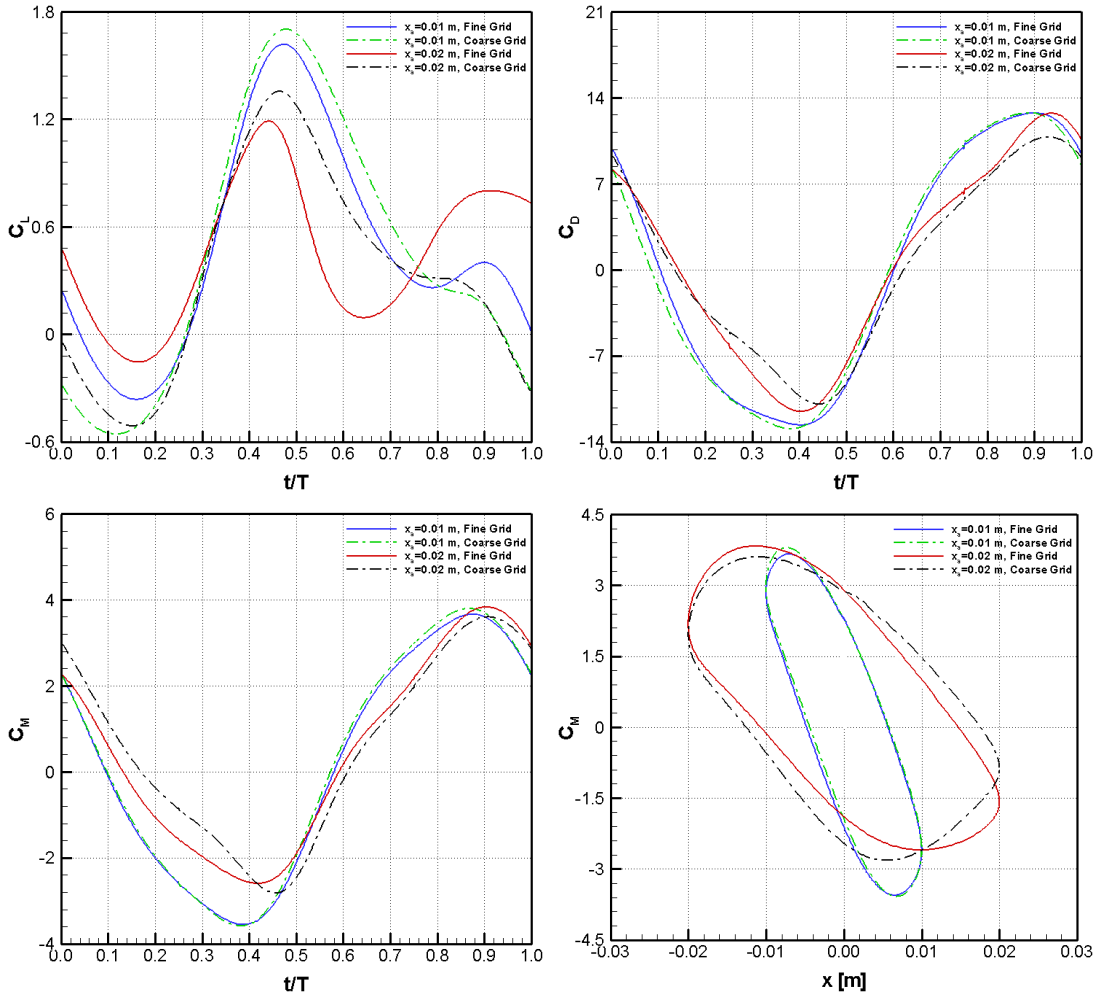

Figure 5.2.8 Time histories of lift, drag and moment coefficients and moment coefficient versus pitching angle distributions obtained from 2-D CFD for purely plunging ($x_a=0.01\ m;\ k=3.0$ and $x_a=0.02\ m;\ k=1.5$) NACA0012 airfoil.

5.3 Results of the Combined Pitch-Plunge Motion Case

5.3.1 SD7003 Airfoil Undergoing Combined Pitch-Plunge Motion

In Figure 5.3.1 and Figure 5.3.2, results of the numerical and experimental studies related to the instantaneous vorticity contours of the pitching-plunging SD7003 airfoil having $\alpha_a=30^o$, $x_a=0.01\ m$ and $\alpha_a=30^o$, $x_a=0.02\ m$ are presented. As in the case of previously discussed test cases, the results obtained from the numerical and experimental studies are in a good agreement with each other for both cases considering the type and location of the vortices observed in the flow. There is clearly a better agreement in the results of the $\alpha_a=30^o$, $x_a=0.01\ m$ case since the oscillation of the $\alpha_a=30^o$, $x_a=0.02\ m$ case is higher. As in the other cases, instantaneous maximum magnitude of the vortices over the airfoil and vortex core radii increase as the plunging amplitude increases from *0.01 m* to *0.02 m* and pitching amplitude stays constant at 30^o. The same phenomenon is also observed if the plunging amplitude of the pitch-plunge motion is kept constant and pitching amplitude of it is increased, the results of which are given in Appendix A.3.1 section. In other words, if the motion gets more oscillatory as the pitching and/or plunging amplitudes increase, the vorticity field observed, consequently, becomes more complex and vortices observed in the highly oscillatory cases dissipate so slowly. In Table 5.3.1 and Table 5.3.2, instantaneous maximum vorticity magnitudes of the LEVs and TEVs attached to the pitching-plunging SD7003 airfoils, obtained from the numerical and experimental calculations, are presented. It is again observed from these two tables that the magnitude of the vortices over the airfoil gets stronger as the plunging amplitude increases from *0.01 m* to *0.02 m* and pitching amplitude stays constant at 30^o.

Phenomenologically, at the beginning of the motion, at t/T=0.0, a CCW rotating (red) TEV formation over the airfoil is observed in the results of the numerical simulations and experimental visualizations of both cases. Location, vortex core radii

and magnitude of this vortex is observed to be similar for the 3-D CFD simulations and PIV visualizations of both cases. However, it is observed to be stronger in 2-D CFD results of both cases. At the same time instant, a CW rotating (blue) LEV development is also observed in all results. Again, magnitude of this vortex is close to each other considering the 3-D CFD and PIV results. CCW rotating detached LEV, remaining from the previous period of motion, is also observed at this time instant. It is also observed to be very strong 2-D CFD studies. CW rotating LEV develops at t/T=0.2 and it detaches from the airfoil at t/T=0.4. Similarly, CCW rotating TEV start to detach from the airfoil at t/T=0.2 and it completely detaches at t/T=0.4 as observed in all results. As in the other cases, detached vortices are washed out by the free stream and consequently, the lift coefficients follow a decreasing trend during t/T=0.4 to t/T=0.55. Following the detachment of CW rotating LEV and CCW rotating TEV, new CCW rotating LEV and CW rotating TEV form over the airfoil as observed again all results. These vortices continue to develop at t/T=0.6 resulting to an increase in the lift coefficients after this time and detach from the airfoil at t/T=0.8 resulting to a decrease in the lift coefficients after this time.

As in the other cases, it is observed that the results of the 3-D CFD simulations are closer to the results of the PIV visualizations considering the all results obtained, mainly due to the three-dimensional effects existing. It is also observed that he vortices observed in the results of the 3-D CFD simulations dissipates more quickly compared to the other cases. Furthermore, results of the 2-D CFD with fine grid simulations differ from the results of the 2-D CFD with coarse grid simulations due to the difference of the domain resolutions of them. Again, the difference in the results of the 2-D CFD simulations increases as the motion becomes more oscillatory, i.e. amplitude of the motion increases.

Furthermore, a deflected vorticity field towards the upstream indicating a lift generation is also observed behind the airfoil in both cases. This phenomenon is clearly observed in the results from t/T=0.2 to t/T=0.4 and t/T=0.6 to t/T=0.8. The lift coefficients of both cases also increase during that time instants. A positive mean

lift coefficient is also calculated from the lift coefficient curves of both cases, which also indicates a lift generation by the airfoils for the overall motion.

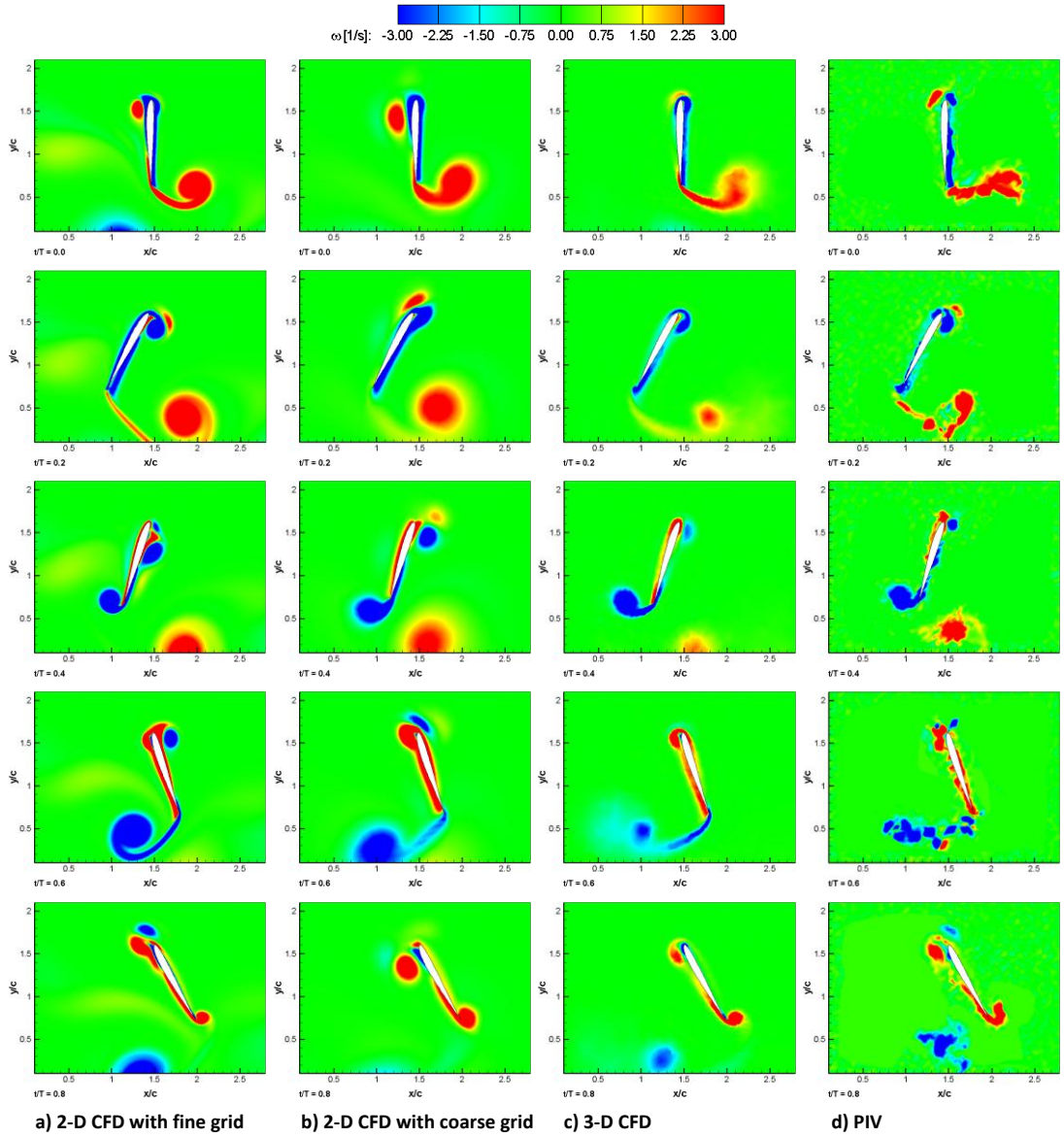

Figure 5.3.1 Instantaneous vorticity contours for pitching-plunging ($\alpha_a=30^o$, $x_a=0.01\ m;\ k=2.4$) SD7003 airfoil.

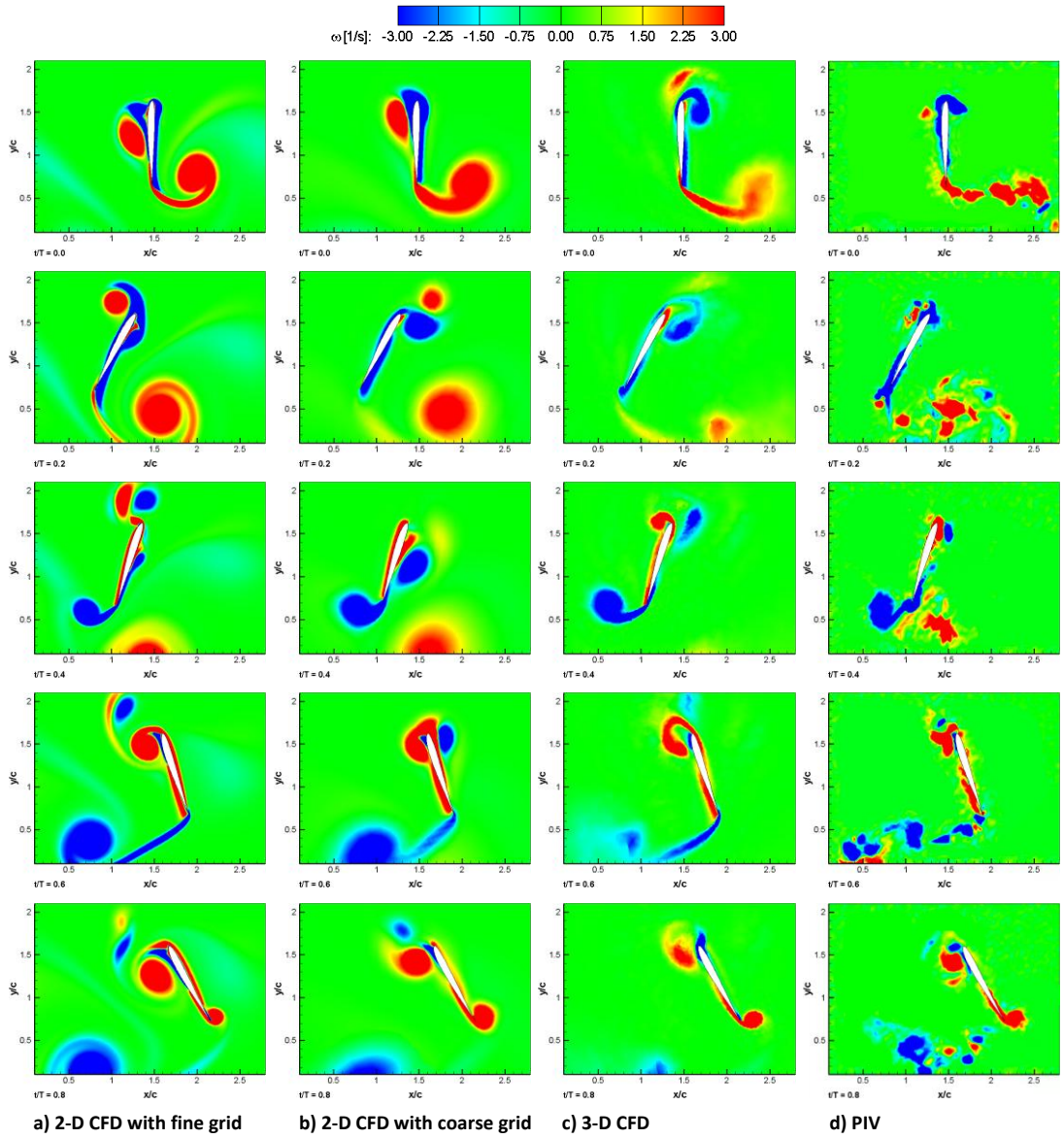

Figure 5.3.2 Instantaneous vorticity contours for pitching-plunging ($\alpha_a=30^o$, $x_a=0.02$ *m;* $k=1.4$) SD7003 airfoil.

Table 5.3.1 Comparison of the instantaneous maximum vorticity magnitudes of LEVs and TEVs attached to the pitching-plunging ($\alpha_a=30^o$, $x_a=0.01$ *m; k=2.4*) SD7003 airfoil [1/s] (positive values indicate the CCW, negative values indicate the CW rotating vortices).

	2-D CFD with fine grid		**2-D CFD with coarse grid**		**3-D CFD**		**PIV**	
Vortex	*LEV*	*TEV*	*LEV*	*TEV*	*LEV*	*TEV*	*LEV*	*TEV*
t/T=0.0	-12.56	9.08	-9.21	5.73	-7.69	3.10	-7.24	5.06
t/T=0.2	-13.40	7.15	-10.55	4.24	-8.12	2.96	-7.86	3.92
t/T=0.4	4.92	-10.34	5.29	-6.39	6.26	-6.50	5.74	-6.28
t/T=0.6	12.29	-9.32	14.34	-4.25	7.20	-3.30	6.87	-4.81
t/T=0.8	9.82	7.45	8.48	6.79	3.38	6.51	3.02	6.43

Table 5.3.2 Comparison of the instantaneous maximum vorticity magnitudes of LEVs and TEVs attached to the pitching-plunging ($\alpha_a=30^o$, $x_a=0.02$ *m; k=1.4*) SD7003 airfoil [1/s] (positive values indicate the CCW, negative values indicate the CW rotating vortices).

	2-D CFD with fine grid		**2-D CFD with coarse grid**		**3-D CFD**		**PIV**	
Vortex	*LEV*	*TEV*	*LEV*	*TEV*	*LEV*	*TEV*	*LEV*	*TEV*
t/T=0.0	-14.87	11.46	-11.57	6.97	-8.82	4.03	-8.33	5.61
t/T=0.2	-15.12	9.75	-12.52	5.76	-9.11	3.78	-8.78	4.45
t/T=0.4	6.67	-13.74	6.08	-8.92	7.48	-9.01	6.83	-8.65
t/T=0.6	13.58	-9.92	15.35	-4.94	9.81	-3.52	8.39	-5.16
t/T=0.8	11.07	10.19	10.16	9.79	5.21	9.42	4.86	9.13

In Figure 5.3.3, instantaneous pressure coefficient contours of pitching-plunging ($\alpha_a=30^o$, $x_a=0.02$ *m; k=1.4*) SD7003 airfoil obtained from the 2-D CFD calculations are given. Starting from the beginning of the period until t/T=0.1, overpressure region at the upper surface of the airfoil decreases as the airfoil moves towards left and as a result, lift coefficient curve goes into a decreasing trend during that time. The local minimum value of the lift coefficient occur nearly at t/T=0.1. Following this, the pressure at the lower surface of the airfoil increases continuing until t/T=0.4. The effect of this pressure increase is observed as an increase in the lift coefficient

during t/T=0.1 to t/T=0.4, at which the local maximum value of the lift coefficient occur. From t/T=0.4 to t/T=0.6, overpressure region at the lower surface of the airfoil start to decrease as the airfoil moves from left to right. As a result, the lift coefficient curve follows a decreasing trend during that time period. After t/T=0.6, overpressure region at the upper surface of the airfoil start to increase and this continues until the end of the period. After t/T=0.6, the lift coefficient follows again an increasing trend until t/T=0.85, after which it again goes into a decreasing trend.

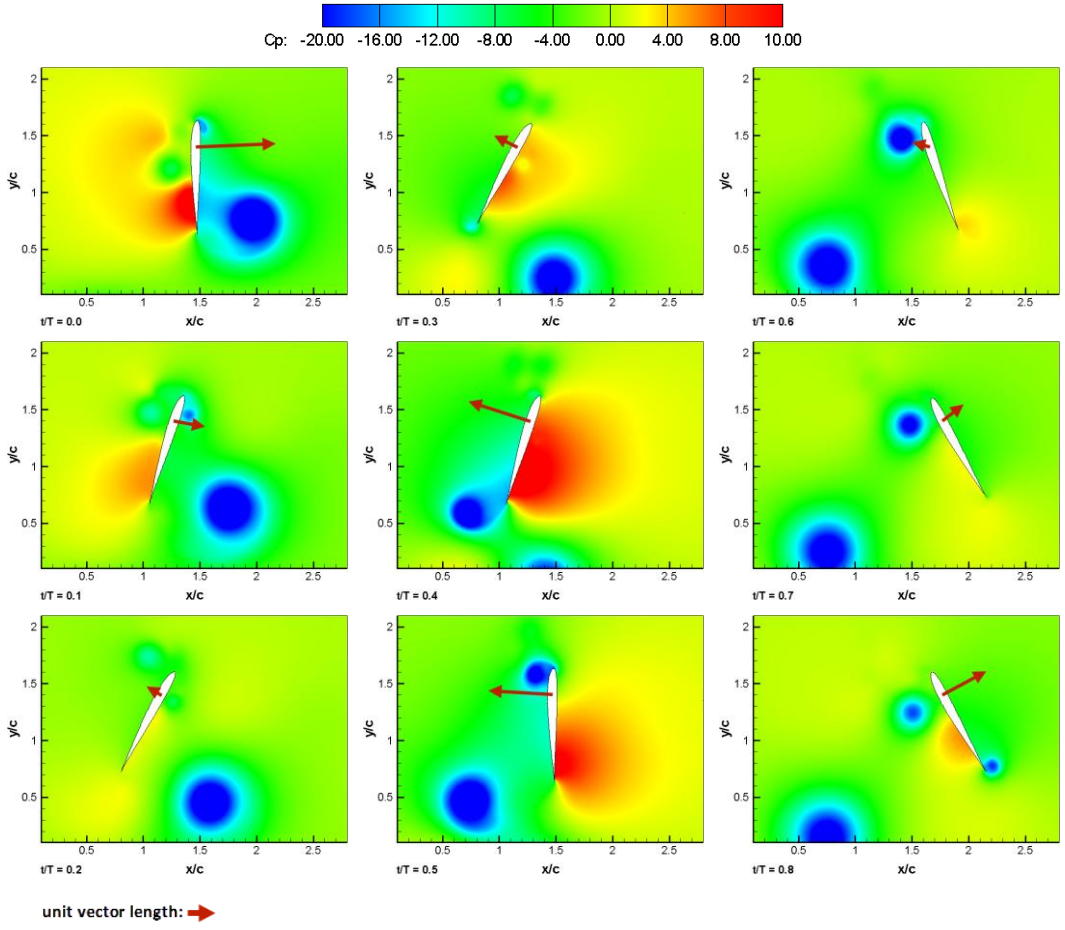

Figure 5.3.3 Instantaneous pressure coefficient (C_p) contours obtained from 2-D CFD for pitching-plunging ($\alpha_a=30^o$, $x_a=0.02$ *m;* $k=1.4$) SD7003 airfoil (vectors in *red color* denote the magnitude of instantaneous total force with its direction).

The instantaneous total force vectors are also shown in Figure 5.3.3. As observed, except at t/T=0.2 and t/T=0.7, the direction of the total force vector and the direction of the leading edge of the airfoil, i.e. pitching direction, are the same. At the turning

points of the motion, at t/T=0.25 and t/T=0.75, the rotational velocities fall to zero and consequently, the magnitude of the total force vectors fall to zero. From t/T=0.0 to t/T=0.15, magnitude of the total force vector decreases resulting to a decrease in the drag coefficient during that time period too. Following this, total force vector changes its direction and its magnitude increases until t/T=0.45 resulting to the further decrease of the drag coefficient. The local minimum value of the drag coefficient occur at t/T=0.45. From t/T=0.45 to t/T=0.65, the magnitude of the total force vector decreases as the airfoil moves towards right whereas the drag coefficient increases. At t/T=0.65, the direction of the total force vector changes once more and magnitude of the total force vector increases until the end of the period. The drag coefficient curve also follows an increasing trend after t/T=0.65. Negative sign of the drag coefficients between t/T=0.15 and t/T=0.65 indicates the thrust producing behavior of the airfoil during that time period. Considering the overall motion, the pitching-plunging ($\alpha_a=30^o$, $x_a=0.02$ *m;* $k=1.4$) NACA0012 airfoil can be said to produce thrust. Among the all studied cases, this case of the combined pitch-plunge motion also produces the highest thrust considering the overall motion.

Time histories of the aerodynamic force and moment coefficients and moment coefficient versus pitching amplitude distributions obtained from the 2-D CFD calculations of the pitching-plunging SD7003 airfoil are presented in Figure 5.3.4. The general trend of each curve is very similar considering the fine and coarse grid simulations of both cases. Therefore, it is possible to conclude that the effect of domain resolution is not very significant for the aerodynamic force and moment coefficient curve characteristics. The drag forces highly dominate the flow in these cases too. The local maximum value of the lift coefficient and mean lift coefficient of the case having $\alpha_a=30^o$, $x_a=0.01$ *m* are greater compared to the case $\alpha_a=30^o$, $x_a=0.02$ *m*. Among the all studied cases, the $\alpha_a=30^o$, $x_a=0.01$ *m* case of the combined pitch-plunge motion of the SD7003 airfoil is also the case having the highest mean lift coefficient. On the other hand, while the local minimum value of the drag coefficient of the $\alpha_a=30^o$, $x_a=0.01$ *m* case is smaller, the mean drag coefficient of the $\alpha_a=30^o$, $x_a=0.02$ *m* case is smaller. As said before, $\alpha_a=30^o$, $x_a=0.02$ *m* case of the pitching-plunging SD7003 airfoil is the case having the lowest mean drag coefficient. Similar

to the phenomenon observed in the lift coefficient, the mean moment coefficient and the local maximum value of the moment coefficient of the $\alpha_a=30^o$, $x_a=0.01\ m$ case is greater. Similar to the previously discussed cases, hysteresis type of graphs is obtained for the moment coefficient versus pitching amplitude distributions of both cases. From these graphs, it can be concluded that the pitching-plunging motions of SD7003 airfoil are stable, moment coefficient versus pitching amplitude curves have negative slope, during the first and third quarters of the motion whereas they are unstable, moment coefficient versus pitching amplitude curves have positive slope, during the rest of the motion.

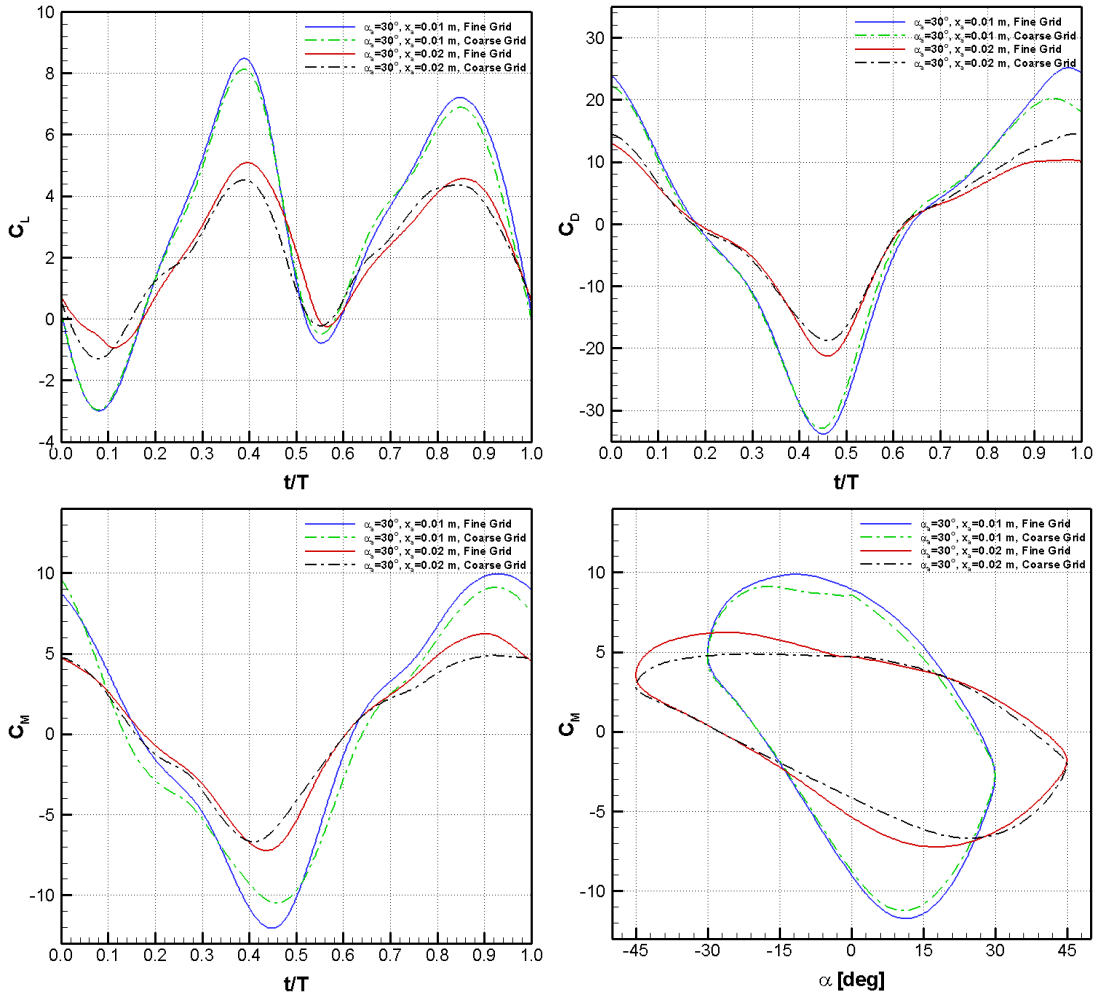

Figure 5.3.4 Time histories of lift, drag and moment coefficients and moment coefficient versus pitching angle distributions obtained from 2-D CFD for pitching-plunging ($\alpha_a=30^o$, $x_a=0.01\ m$; $k=2.4$ and $\alpha_a=30^o$, $x_a=0.02\ m$; $k=1.4$) SD7003 airfoil.

5.3.2 NACA0012 Airfoil Undergoing Combined Pitch-Plunge Motion

Results of the instantaneous vorticity contours of the NACA0012 airfoil undergoing combined pitch-plunge motion having $\alpha_a=30^o$, $x_a=0.01\ m$ and $\alpha_a=30^o$, $x_a=0.02\ m$ obtained from the numerical and experimental studies are presented in Figure 5.3.5 and Figure 5.3.6, respectively. The results of the other cases of the pitching-plunging NACA0012 airfoil are given in Appendix A.3.2 section. An agreement between the numerical experimental studies regarding to the type and location of the vortices over the airfoil is also observed for these cases. As in the case of pitching-plunging SD7003 airfoil, the agreement is observed to be better in the results of the case $\alpha_a=30^o$, $x_a=0.01\ m$ since the case $\alpha_a=30^o$, $x_a=0.02\ m$ is more oscillatory. As it can be seen from the results obtained, the instantaneous maximum magnitude of the vortices over the airfoil and their core radii depends on the amplitude of the motion. Namely, both of them increase with the increase of the amplitude of the motion. Increasing the plunging amplitude while the pitching amplitude is kept constant or increasing the pitching amplitude while the plunging amplitude is kept constant makes both of them to increase. Vortices are again observed to dissipate quicker in the lower amplitude pitching-plunging motion cases compared to the higher amplitude pithing-plunging motion cases. The instantaneous maximum vorticity magnitudes of the LEVs and TEVs attached to the pitching-plunging NACA0012 airfoils, obtained from the numerical and experimental calculations, are given in Table 5.3.3 and Table 5.3.4. The results presented in these two tables also indicate that as the plunging amplitude increases from *0.01 m* to *0.02 m* while the pitching amplitude is kept constant at 30^o, the vortices over the airfoil become stronger. Compared to the vortices over the pitching-plunging SD7003 airfoils, the vortices over the pitching-plunging NACA0012 airfoils are observed to be slightly weaker.

From the phenomenological point of view, at the beginning of the motion, at t/T=0.0, a CCW rotating (red) TEV around the airfoil is observed in the numerical and experimental results of both cases. Considering the results of the 3-D CFD and PIV studies, the strength and location of this vortex is very close to each other. Yet, this

vortex is observed to be stronger in the results of the 2-D CFD studies. Moreover, a CW rotating (blue) LEV formation over the leading edge of the airfoil is also observed at t/T=0.0 in all results of both cases. The strength of this vortex is again very close to each other considering the results of the 3-D CFD and PIV studies. At this time instant, a CCW rotating detached LEV formation, remaining from the previous period, is also observed. CW rotating LEV observed at t/=0.0 develops at t/T=0.2 and it detaches from the airfoil at t/T=0.4. Similarly, CCW rotating TEV formed at t/T=0.0 start to detach from the airfoil at t/T=0.2 and it completely detaches at t/T=0.4. The detached LEV and TEV are washed out by the free stream and this results to a decrease in the lift coefficients during t/T=0.4 to t/T=0.55. At t/T=0.4, new CCW rotating LEV and CW rotating TEV form over the airfoil and they develop at t/T=0.6 resulting to an increase in the lift coefficients after this time. These vortices detach from the airfoil at t/T=0.8 and this results again to a decrease in the lift coefficients after t/T=0.8.

As in the case previously studied cases, the results of the 3-D CFD simulations and PIV visualizations are found to be closer to each other by means of the instantaneous vortices over the airfoil. The possible reason of this is thought to be the three-dimensional effects existing. Furthermore, the dissipation rate of the vortices observed in the results of the 3-D CFD simulations is higher compared to the other cases. The results of the 2-D CFD simulations also differ from each other mainly because of the difference of the resolution of the 2-D coarse and fine grid domains as observed in all studied cases.

Moreover, deflected vortex patterns behind the airfoil are also observed in the results of both cases. The vortices are deflected towards the upstream indicating a lift generation. This is clearly observed in the results of the numerical and experimental studies from t/T=0.2 to t/T=0.4 and t/T=0.6 to t/T=0.8. The lift coefficients of both cases also increase during that time instants. For both cases, a positive mean lift coefficient is also obtained considering the whole period, which also indicates a lift generation by the airfoils.

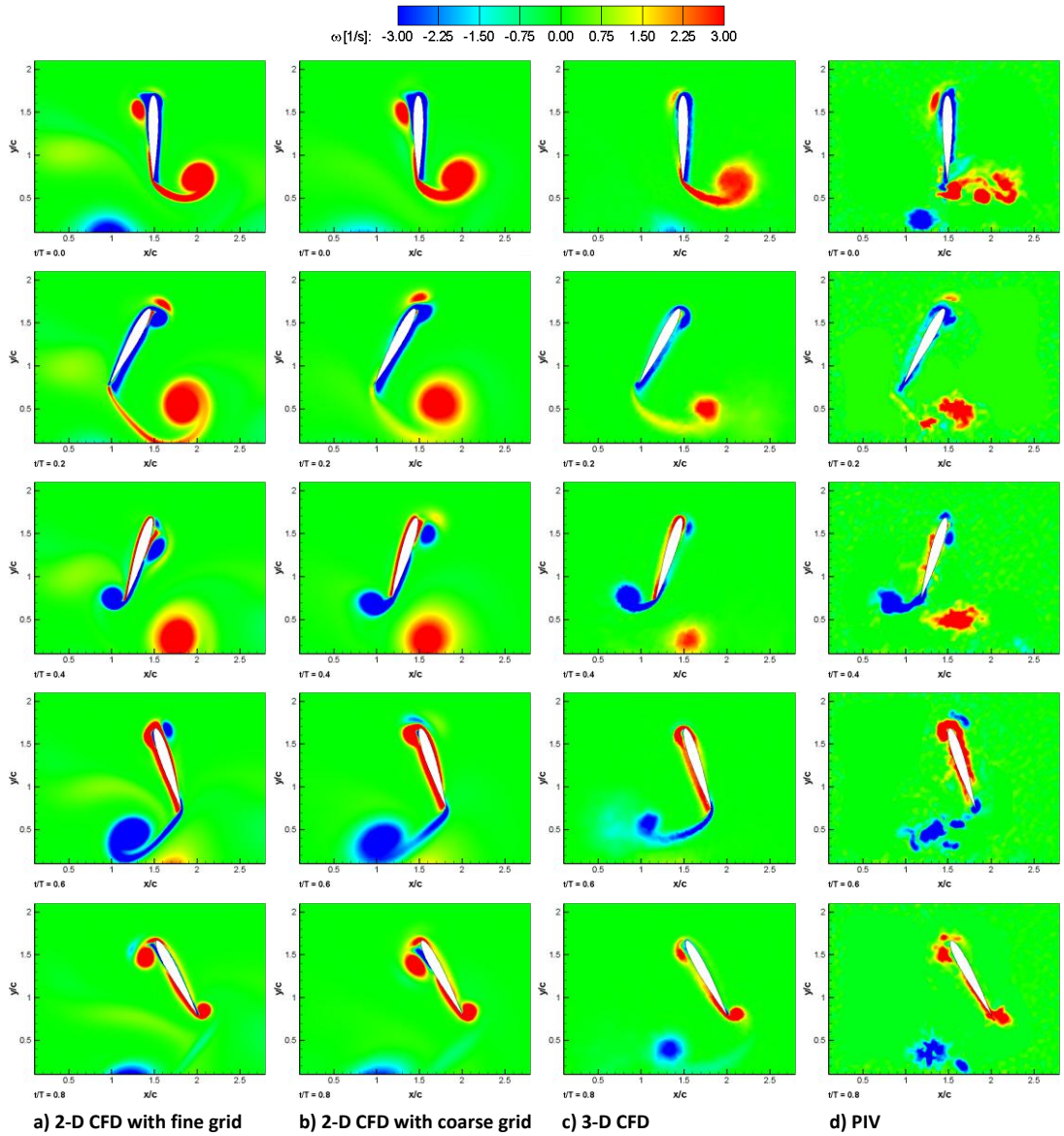

Figure 5.3.5 Instantaneous vorticity contours for pitching-plunging ($\alpha_a=30^o$, $x_a=0.01$ *m;* $k=2.4$) NACA0012 airfoil.

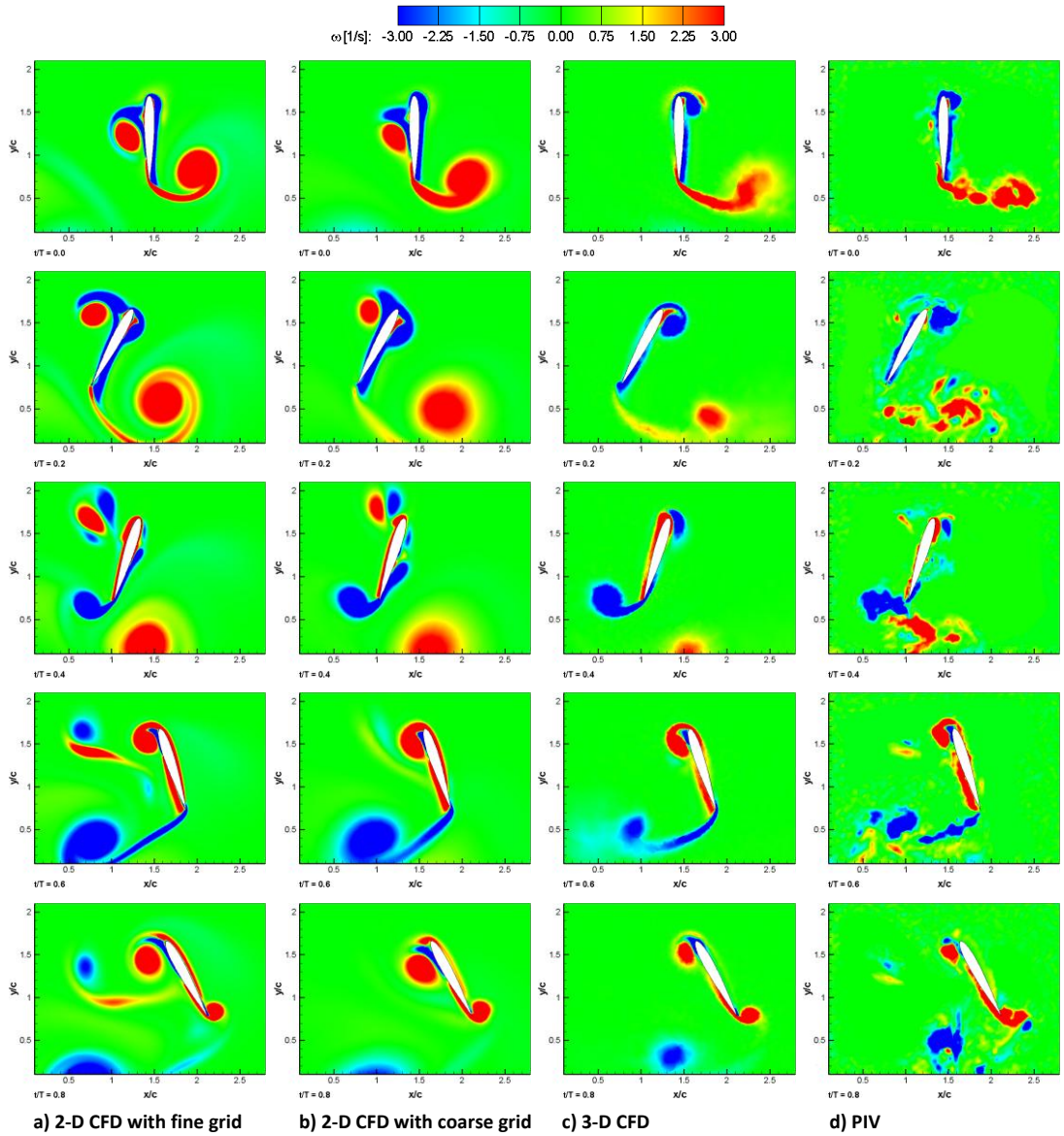

Figure 5.3.6 Instantaneous vorticity contours for pitching-plunging ($\alpha_a=30^o$, $x_a=0.02$ *m;* $k=1.4$) NACA0012 airfoil.

Table 5.3.3 Comparison of the instantaneous maximum vorticity magnitudes of LEVs and TEVs attached to the pitching-plunging ($\alpha_a=30^o$, $x_a=0.01$ *m; k=2.4*) NACA0012 airfoil [1/s] (positive values indicate the CCW, negative values indicate the CW rotating vortices).

	2-D CFD with fine grid		**2-D CFD with coarse grid**		**3-D CFD**		**PIV**	
Vortex	*LEV*	*TEV*	*LEV*	*TEV*	*LEV*	*TEV*	*LEV*	*TEV*
t/T=0.0	-12.38	8.90	-9.03	5.85	-7.54	2.87	-7.06	4.78
t/T=0.2	-13.35	7.51	-10.45	4.36	-7.99	3.02	-7.68	3.72
t/T=0.4	3.78	-11.24	4.98	-6.54	6.16	-6.75	5.65	-6.31
t/T=0.6	12.10	-8.85	14.12	-3.54	6.89	-3.36	6.67	-4.78
t/T=0.8	9.34	7.28	8.05	6.61	3.21	6.38	2.98	6.32

Table 5.3.4 Comparison of the instantaneous maximum vorticity magnitudes of LEVs and TEVs attached to the pitching-plunging ($\alpha_a=30^o$, $x_a=0.02$ *m; k=1.4*) NACA0012 airfoil [1/s] (positive values indicate the CCW, negative values indicate the CW rotating vortices).

	2-D CFD with fine grid		**2-D CFD with coarse grid**		**3-D CFD**		**PIV**	
Vortex	*LEV*	*TEV*	*LEV*	*TEV*	*LEV*	*TEV*	*LEV*	*TEV*
t/T=0.0	-14.57	11.54	-11.21	7.03	-8.54	4.09	-8.11	5.42
t/T=0.2	-15.02	9.72	-12.19	5.80	-9.16	3.86	-8.85	4.50
t/T=0.4	6.78	-13.68	5.83	-9.01	7.29	-8.91	6.54	-8.58
t/T=0.6	13.62	-9.77	15.29	-4.99	9.92	-3.65	8.07	-5.09
t/T=0.8	11.29	10.08	10.07	9.68	5.08	9.38	4.66	9.15

Instantaneous pressure coefficient contours of pitching-plunging ($\alpha_a=30^o$, $x_a=0.02$ *m; k=1.4*) NACA0012 airfoil obtained from the 2-D CFD simulations are presented in Figure 5.3.7. The phenomena observed in this case are very similar to the pitching-plunging ($\alpha_a=30^o$, $x_a=0.02$ *m; k=1.4*) SD7003 airfoil case. Namely, from the beginning of the period, t/T=0.0, to t/T=0.1, pressure at the upper surface of the airfoil decreases as the airfoil start it movement from its initial position towards left. As a result, lift coefficients follow a decreasing trend during that time period. The local minimum value of the lift coefficient occur nearly at t/T=0.1 as in the case of

pitching-plunging SD7003 airfoil. Following this time, overpressure region at the lower surface of the airfoil start to increase and this continues until t/T=0.4. As a result of this pressure increase, the lift coefficients also increase during t/T=0.1 to t/T=0.4. The local maximum value of the lift coefficient occur at t/T=0.4. From t/T=0.4 to t/T=0.6, pressure at the lower surface of the airfoil start to decrease as the airfoil moves from left to right and this makes the lift coefficients to follow a decreasing trend during that time period. After t/T=0.6, pressure at the upper surface of the airfoil increases, which continues until the end of the period. After t/T=0.6, the lift coefficient curve follows again an increasing trend until t/T=0.85, after which it again decreases.

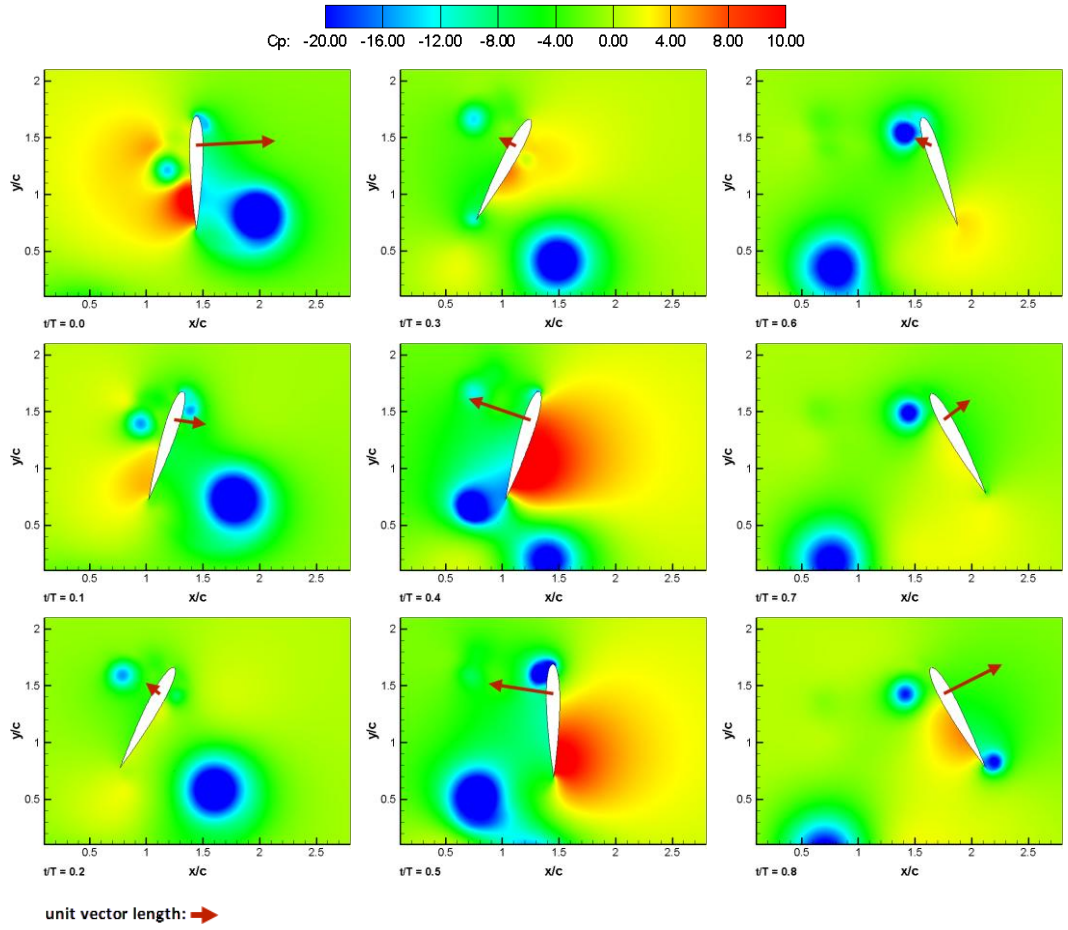

Figure 5.3.7 Instantaneous pressure coefficient (C_p) contours obtained from 2-D CFD for pitching-plunging ($\alpha_a=30^o$, $x_a=0.02$ *m;* $k=1.4$) NACA0012 airfoil (vectors in *red color* denote the magnitude of instantaneous total force with its direction).

The instantaneous total force vectors are also presented in Figure 5.3.7. As it is observed, except at t/T=0.2 and t/T=0.7, the direction of the total force vector and the direction of the leading edge of the airfoil are the same. At t/T=0.25 and t/T=0.75, after which the direction of motion changes, the rotational velocities fall to zero and as a result, the magnitude of the total force vectors fall to zero. Starting from t/T=0.0 until t/T=0.15, magnitude of the total force vector decreases and this results to a decrease in the drag coefficient during that time period too. Following this, total force vector changes its direction and its magnitude increases until t/T=0.45. This results to the further decrease of the drag coefficient and the local minimum value of it occur at t/T=0.45. Between t/T=0.45 to t/T=0.65, the magnitude of the total force vector decreases as the airfoil moves towards right. During that time period, the drag coefficient increases. At t/T=0.65, the direction of the total force vector changes once more and its magnitude start to increase, which continue until the end of the period. The drag coefficient also start to increase after t/T=0.65. Negative sign of the drag coefficients between t/T=0.15 and t/T=0.65 indicates a thrust production by the airfoil. Considering the whole period, this pitching-plunging NACA0012 airfoil case can be said to be a thrust producing case.

Time histories of the aerodynamic force and moment coefficients and moment coefficient versus pitching amplitude distributions obtained from the 2-D CFD calculations of the pitching-plunging NACA0012 airfoil are given in Figure 5.3.8. The general trend of each curve is very similar for the fine and coarse grid simulations of both cases. Again, the drag forces highly dominate the flow in both cases. As in the case of pitching-plunging SD7003 airfoil, the local maximum value of the lift coefficient and mean lift coefficient of the case having $\alpha_a=30^o$, $x_a=0.02\ m$ are smaller compared to the case $\alpha_a=30^o$, $x_a=0.01\ m$. Similarly, the mean moment coefficient and the local maximum value of the moment coefficient of the $\alpha_a=30^o$, $x_a=0.01\ m$ case is greater. On the other hand, while the local minimum value of the drag coefficient of the $\alpha_a=30^o$, $x_a=0.02\ m$ case is greater, the mean drag coefficient of the $\alpha_a=30^o$, $x_a=0.01\ m$ case is greater. Similar to the other cases, hysteresis type of graphs is obtained for the moment coefficient versus pitching amplitude distributions of both cases. From these graphs, it can be concluded that the pitching-plunging

motions of NACA0012 airfoil are stable, moment coefficient versus pitching amplitude curves have negative slope, during the first and second halves of the downstroke and upstroke, respectively whereas they are unstable, moment coefficient versus pitching amplitude curves have positive slope, during the second and first halves of the downstroke and upstroke, respectively.

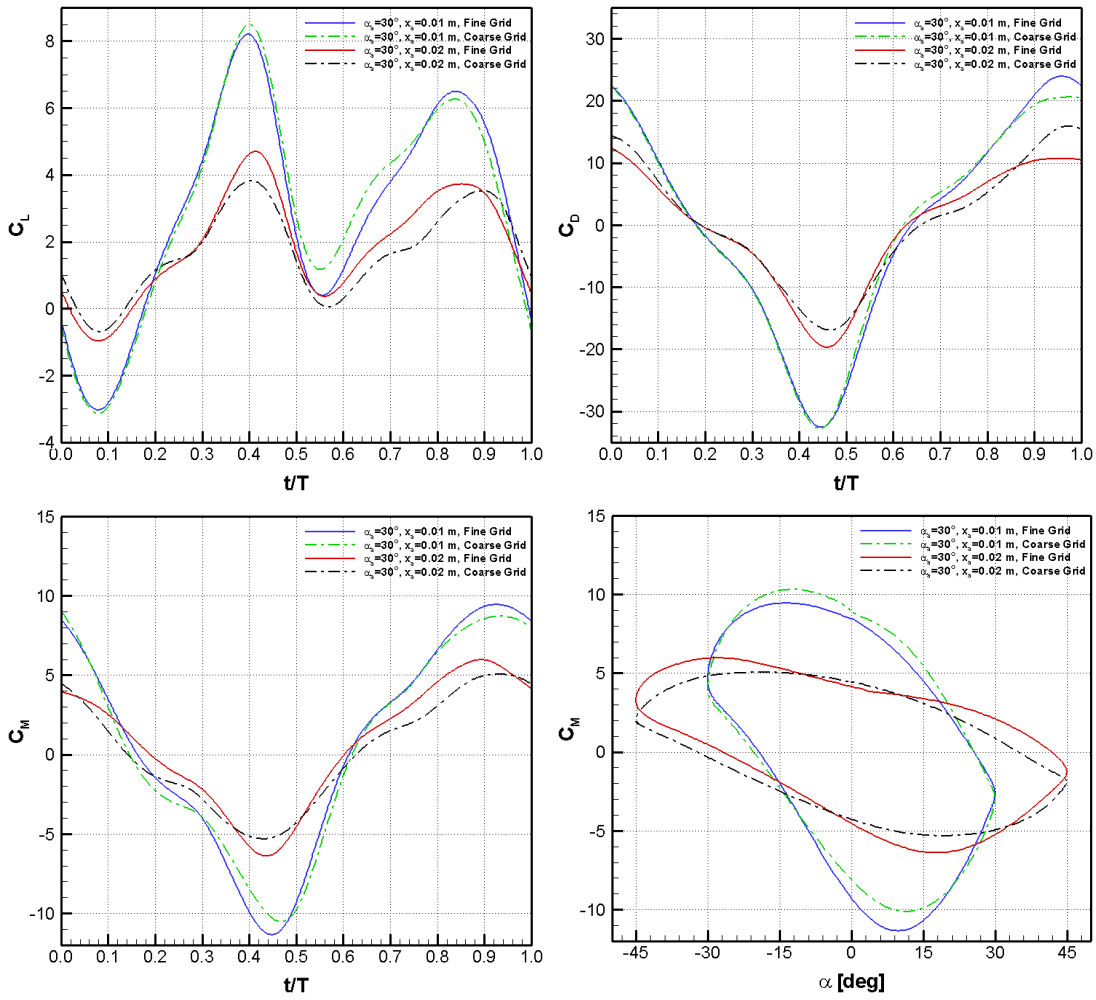

Figure 5.3.8 Time histories of lift, drag and moment coefficients and moment coefficient versus pitching angle distributions obtained from 2-D CFD for pitching-plunging ($\alpha_a=30^o$, $x_a=0.01$ *m;* $k=2.4$ and $\alpha_a=30^o$, $x_a=0.02$ *m;* $k=1.4$) NACA0012 airfoil.

5.4 Comparison of the Aerodynamic Force and Moment Coefficients

In Table 5.4.1, the mean aerodynamic force and moment coefficients obtained from 2-D CFD calculations for purely pitching four different airfoils are tabulated. As seen in this table, as the pitching amplitude increases from 10^o to 30^o, the mean lift coefficient values exhibit an increasing behavior for SD7003 and NACA0012 airfoils. However, further increase of the pitching amplitude to 45^o makes the mean lift coefficient values to drop. This phenomenon is observed for all airfoils and the maximum mean lift coefficients occur for the cases having pitching amplitude of 30^o. A similar behavior is observed for the mean drag coefficient values too. For SD7003 and NACA0012 airfoils, it decreases with the increase of the pitching amplitude from 10^o to 30^o and then follows an increasing trend from 30^o to 45^o for all airfoils. Again, the minimum mean drag coefficients are obtained from the cases having pitching amplitude of 30^o for all airfoils. Except 10% thick flat plate airfoil, all other airfoils have a negative mean drag coefficient indicating a thrust producing behavior of these airfoils for the overall motion. And lastly, the general behavior of the mean moment coefficient is similar for all airfoils such that it increases with the increasing pitching amplitude. The cases having the highest pitching amplitude have the highest mean moment coefficients for all airfoils.

As a result of the pure pitch motion studies, both of the highest mean lift coefficient and the lowest mean drag coefficient are obtained from purely pitching ($\alpha_a=30^o$; $k=3.8$) SD7003 airfoil case whereas the highest mean moment coefficient is obtained from purely pitching ($\alpha_a=45^o$; $k=2.5$) NACA0012 airfoil case, which is also the case having the highest mean moment coefficient among the all studied hovering motion cases.

Table 5.4.1 The mean aerodynamic force and moment coefficients obtained from 2-D CFD for pure pitch motion cases.

	SD7003			**NACA0012**			**10% Thick Elliptical**		**10% Thick Flat Plate**	
α_a	*10^o*	*30^o*	*45^o*	*10^o*	*30^o*	*45^o*	*30^o*	*45^o*	*30^o*	*45^o*
k	*11.5*	*3.8*	*2.5*	*11.5*	*3.8*	*2.5*	*3.8*	*2.5*	*3.8*	*2.5*
$\overline{C_L}$	2.3838	2.7266	2.1287	1.7016	2.6219	2.1213	1.0698	0.3902	0.6032	0.1156
$\overline{C_D}$	-0.0701	-0.5380	-0.2401	0.0458	-0.4358	-0.1215	-0.2265	-0.0956	0.4502	0.5542
$\overline{C_M}$	-0.0998	0.2976	0.5872	-0.0422	0.7780	**1.0431**	-0.4907	-0.0910	-0.6430	0.2228

The mean aerodynamic force and moment coefficients obtained from 2-D CFD calculations for purely plunging four different airfoils are given in Table 5.4.2. The general trend of all coefficients is similar for all airfoils. In other words, the mean lift coefficient and the mean drag coefficient values show a decreasing trend with the increasing plunging amplitude for all airfoils studied. On the other hand, as in the case of pure pitch motion, the mean moment coefficient values of all airfoils increases as the plunging amplitude increases. The results of the pure plunge studies indicate that the highest mean lift coefficient is obtained from purely plunging (x_a*=0.01 m; k=3.0*) SD7003 airfoil case while the lowest mean drag coefficient value is obtained from purely plunging (x_a*=0.03 m; k=1.0*) SD7003 airfoil case. The highest mean moment coefficient, on the other hand, is obtained from purely plunging (x_a*=0.03 m; k=1.0*) NACA0012 airfoil case.

Table 5.4.2 The mean aerodynamic force and moment coefficients obtained from 2-D CFD for pure plunge motion cases.

	SD7003			**NACA0012**			**10% Thick Elliptical**		**10% Thick Flat Plate**	
x_a	*0.01m*	*0.02m*	*0.03m*	*0.01m*	*0.02m*	*0.03m*	*0.01m*	*0.02m*	*0.01m*	*0.02m*
k	*3.0*	*1.5*	*1.0*	*3.0*	*1.5*	*1.0*	*3.0*	*1.5*	*3.0*	*1.5*
$\overline{C_L}$	0.5142	0.4471	0.3152	0.4759	0.4439	0.3035	0.0120	-0.0224	-0.0007	-0.0716
$\overline{C_D}$	0.1700	-0.1927	-0.3070	0.0591	0.0364	-0.2898	0.1602	0.0353	0.2627	0.1104
$\overline{C_M}$	0.0091	0.2847	0.3791	0.1172	0.4248	0.5981	0.0437	0.0896	-0.0697	-0.0023

The tabulated data corresponding to the mean aerodynamic force and moment coefficients obtained from 2-D CFD calculations for the airfoils undergoing combined pitch-plunge motion are given in Table 5.4.3 and Table 5.4.4. From these tables, it is observed that the mean lift coefficient values decrease while keeping the pitching amplitude constant and increasing the plunging amplitude for all studied cases. On the other hand, as in the case of pure pitch motion, they increase with the increase of the pitching amplitude from 10^o to 30^o and from then starts to decrease until 45^o independently from the plunging amplitude. The highest mean lift coefficients, for this reason, occur for the cases having $\alpha_a=30^o$ and $x_a=0.01\ m$ for all the cases. The mean drag coefficient values, on the other side, decrease while keeping the pitching amplitude constant and increasing the plunging amplitude for all studied cases. Additionally, they decrease with the increasing pitching amplitude from 10^o to 30^o and then increase until 45^o independently from the plunging amplitude. As a result of this phenomenon, the lowest mean drag coefficients are obtained from the cases having $\alpha_a=30^o$ and $x_a=0.02\ m$. Except all the cases of 10% thick elliptical airfoil and $\alpha_a=45^o$ and $x_a=0.01\ m$ case of NACA0012 airfoil, all other cases have a negative mean drag coefficient indicating a thrust producing behavior of these cases for the overall motion The mean moment coefficient values, however, shows an increasing trend as the pitching or the plunging amplitude increases and therefore, the highest mean moment coefficients are obtained from the cases having $\alpha_a=45^o$ and $x_a=0.02\ m$.

From the results of the combined pitch-plunge studies, it is observed that the highest mean lift coefficient and the lowest mean drag coefficient are obtained from the cases of SD7003 airfoil having $\alpha_a=30^o$, $x_a=0.01$; $k=2.4$ and $\alpha_a=30^o$, $x_a=0.02$; $k=1.4$, which are also the cases having the highest mean lift coefficient and the lowest mean drag coefficient among the all studied cases, respectively. The highest mean moment coefficient, on the other side, is obtained from $\alpha_a=45^o$, $x_a=0.02$; $k=1.3$ case of the NACA0012 airfoil.

Table 5.4.3 The mean aerodynamic force and moment coefficients obtained from 2-D CFD for combined pitch-plunge motion cases of SD7003 and NACA0012 airfoils.

	SD7003						**NACA0012**					
α_a	10^o		30^o		45^o		10^o		30^o		45^o	
x_a	*0.01m*	*0.02m*	*0.01m*	*0.02m*	*0.01m*	*0.02m*	*0.01m*	*0.02m*	*0.01m*	*0.02m*	*0.01m*	*0.02m*
k	*2.9*	*1.5*	*2.4*	*1.4*	*1.9*	*1.3*	*2.9*	*1.5*	*2.4*	*1.4*	*1.9*	*1.3*
$\overline{C_L}$	1.6549	1.1796	**3.0414**	2.1756	2.4568	1.7209	1.6260	1.0866	2.9341	1.8889	2.6810	1.8024
$\overline{C_D}$	-0.3497	-0.4357	-0.4636	**-0.5717**	-0.0934	-0.1657	-0.1863	-0.2368	-0.2913	-0.3787	0.0368	-0.1285
$\overline{C_M}$	0.1430	0.2405	0.3568	0.4729	0.3734	0.5278	0.3159	0.4904	0.5629	0.6010	0.6525	0.9753

Table 5.4.4 The mean aerodynamic force and moment coefficients obtained from 2-D CFD for combined pitch-plunge motion cases of 10% thick elliptical airfoil.

	10% Thick Elliptical			
α_a	30^o		45^o	
x_a	*0.01m*	*0.02m*	*0.01m*	*0.02m*
k	*2.4*	*1.4*	*1.9*	*1.3*
$\overline{C_L}$	1.9114	1.4534	1.5831	1.3943
$\overline{C_D}$	0.4379	0.3592	0.7713	0.6190
$\overline{C_M}$	0.4302	0.5282	0.6219	0.7228

Among the all studied hovering motion cases, the highest mean lift coefficient is obtained from SD7003 airfoil case undergoing a combined pitch-plunge motion ($\alpha_a=30^o$, $x_a=0.01$; $k=2.4$) whereas the lowest is obtained from purely plunging ($x_a=0.02$ *m*; $k=1.5$) 10% thick flat plate airfoil case. The lowest mean drag coefficient is obtained from pitching-plunging ($\alpha_a=30^o$, $x_a=0.02$; $k=1.4$) SD7003 airfoil case whereas pitching-plunging ($\alpha_a=45^o$, $x_a=0.01$ *m*; $k=1.9$) 10% thick elliptical airfoil case gives the highest. Additionally, the highest mean moment coefficient is obtained from the purely pitching ($\alpha_a=45^o$; $k=2.5$) NACA0012 airfoil case while the lowest is obtained from 10% thick flat plate airfoil case undergoing a pure pitch motion ($\alpha_a=30^o$; $k=3.8$).

CHAPTER 6

CONCLUSION

6.1 General Conclusions

In this thesis, pure pitch, pure plunge and combined pitch-plunge modes of the constant frequency and unsteady hovering motion of four different airfoils, SD7003, NACA0012, 10% thick elliptical, 10% thick flat plate, are investigated by means of the numerical simulations and experimental visualizations mainly in order to provide a better understanding of the complex aerodynamics phenomena and the vortex topology of flapping wings and to validate the newly built experimental setup with the numerical simulations. The numerical and experimental investigations are also extended over the hovering cases having different pitching and plunging amplitudes to study the effect of these parameters on the different modes of hovering motion. For this purpose, the flow field around the airfoils is visualized by solving the unsteady, incompressible Navier-Stokes equations on the 2-D and 3-D computational grids with Fluent v6.3.26. The aerodynamic force and moment coefficient versus time histories and instantaneous vorticity contours are visualized for each mode of motion. On the other hand, the instantaneous velocity field data of the flow around the airfoils are acquired by the Particle Image Velocimetry (PIV) measurements. After then, the results of the different types of visualizations are compared.

An agreement between the results of the numerical and experimental studies of the investigated cases is obtained in terms of the instantaneous vortex structure of the flow around the airfoils. The results acquired from the studies of the baseline test

cases indicate that the results of the 3-D CFD simulations and PIV measurements are very close to each other in terms of the size, location and type of the vortices observed throughout the whole period of motion. The possible reason of this phenomenon is thought to be the three-dimensional effects existing. Nevertheless, the results of these two studies are not exactly the same mainly because of the experimental conditions that could not be modeled numerically. Applying a pressure outlet boundary condition to the open surface area of the water tank instead of applying a free surface boundary condition due to the incapableness of the numerical tools is thought to be one of them. Furthermore, some discrepancies are observed between the results of the 2-D CFD simulations and PIV visualizations as well as between the results of the 2-D CFD with fine grid and coarse grid simulations. The difference between the results of two different types of the 2-D CFD simulations is observed to be very distinguishable. Namely, the interaction of the vortices generated over the airfoil with the trace of the vortices remaining from the previous stroke is observed in the results of the 2-D CFD with fine grid simulations. This can clearly be observed in the results of the pure plunge studies. On the other hand, this phenomenon is not very noticeable in the results of the 2-D CFD with coarse grid simulations. Hence, it is concluded that the mesh intensity of the computational grid domain strongly affects the formation of the vortices and their duration in the flow field. The closer mesh intensity of the computational grid domain to the intensity of the experimental solution domain, the closer results to the PIV visualizations are obtained by the numerical simulations.

The pitching and plunging amplitudes are also observed to affect the magnitude, size and duration of the vortices observed in the flow field. It is observed that the vortices get stronger, become bigger in size and stay longer in the flow field as the pitching or plunging amplitude of the motion is increased. The amplitude of the motion is also observed to have an effect on the generation of the LEV in the pure pitch cases. Namely, for the pure pitch cases having pitching amplitude of 10^o, no LEV generation by the airfoils is observed considering both the numerical and experimental results obtained.

It is also observed that the vortex patterns observed in the present study in terms of the interaction of the vortices and aerodynamic force and moment generation are very close to the results of the previous studies in the literature related to the flapping wings in hover undergoing a sinusoidal motion, such as the studies of Freymuth [42], Birch and Dickinson [83] and Wang et al. [62]. The flow phenomenon figured out in the forward flapping flight studies of Jones and Platzer ([60], [82]) is also observed in pure pitch and combined pitch-plunge cases studied. Namely, the vortex street behind the airfoil undergoing pure pitch and combined pitch-plunge motions is deflected towards upstream indicating a lift generation. The aerodynamic force time histories of the airfoils undergoing those motions, obtained from the 2-D CFD simulations, also support this phenomenon.

Considering the aerodynamic force and moment coefficients generated by the airfoils, the general trend of the lift, drag and moment coefficient versus time curves of the airfoils undergoing same type of hovering motion is observed to be similar. Besides, very similar results are also obtained from the 2-D CFD simulations having different mesh intensities of the pure pitch and combined pitch-plunge motions of the baseline test cases in terms of the aerodynamic force and moment coefficient curves whereas some discrepancies are observed between the different types of 2-D CFD simulations of the pure plunge motions of them. It is also observed that the airfoils undergoing combined pitch-plunge motion generated more lift and more thrust. Because of this, among the all studied cases, the highest mean lift coefficient and the lowest mean drag coefficient values are obtained from the pitching-plunging SD7003 airfoil cases having $\alpha_a=30^o$, $x_a=0.01\ m$ and $\alpha_a=30^o$, $x_a=0.02\ m$, respectively. Furthermore, 10% thick elliptical and 10% thick flat plate airfoils are observed to produce fairly less lift and less thrust compared to the SD7003 and NACA0012 airfoils. Considering the moments generated by the airfoils, the highest mean moment coefficient value is obtained from the purely pitching ($\alpha_a=45^o;\ k=2.5$) NACA0012 airfoil case. Since the NACA0012 airfoil is the thickest airfoil investigated during the present study, this result is thought to be expected.

6.2 Recommendations for Further Studies

The present study is like a pilot study in order to show the capabilities of the newly built PIV setup related to the investigation of the low frequency flapping wing studies in hover. The results obtained from the present study can be said to be consistent with the results of the numerical simulations and the results available in the literature. The phenomena related to flapping wings can further be studied both numerically and experimentally. For instance, impulsive start phenomenon of different airfoils can be studied both numerically and experimentally. Using a time resolved PIV (TR-PIV) system for the experimental visualization of the impulsive start phenomenon is thought to be more beneficial. Moreover, the present study is performed for a constant frequency hovering motion. In order to investigate the effect of frequency of the hovering motion on the instantaneous aerodynamics phenomenon of the flapping wings, the present studies can be extended over the cases having various hovering motion frequencies. More complex modes of the hovering motion, such as the figure-of-eight motion, can also be studied by modifying the present experimental setup to make it to be capable of performing the plunging motion in the vertical direction also.

Lastly, it is strongly suggested to the further researchers of this field to double check the boundary condition applied at the wake of the airfoil in order not to have any pressure discontinuities at the wake of the airfoil, to try to obtain a numerical solution applying a wall boundary condition at the outer boundaries of the 2-D numerical grids, to perform a 3-D numerical study with a finer grid domain, and to try to obtain numerical solutions by applying central difference schemes.

REFERENCES

[1] Dial, K.P., *An Inside Look at How Birds Fly: Experimental Studies of the Internal and External Processes Controlling Flight*. 1994 Report to the Aerospace Profession, 38th Symposium Proceedings, Beverly Hills, CA, 1994.

[2] Shyy, W., Lian, Y., Tang, J., Viieru, D., and Liu, H., *Aerodynamics of Low Reynolds Number Flyers*, Cambridge Univ. Press, New York, 2008.

[3] Kurtuluş, D.F., *Introduction to Micro Air Vehicles: Concepts, Design and Applications*. VKI LS 2011-04: Recent Developments in Unmanned Aircraft Systems (UAS, including UAV and MAV), ISBN-13 978-2-87516-017-1, pp. 1-30, April 2011.

[4] Kurtuluş, D.F., *Unsteady Aerodynamics of Flapping Aerofoils: Case Studies with Experimental, Numerical, Theoretical and Soft Computing Methods*. VKI LS 2011-04: Recent Developments in Unmanned Aircraft Systems (UAS, including UAV and MAV), ISBN-13 978-2-87516-017-1, pp. 1-36, April 2011.

[5] Babinsky, H., Baik, Y., Bansmer, S., Beran, P., Bernal, L., Günaydınoğlu, E., Jones, A., Kang, C.K., Konrath, R., Kurtuluş D.F., Ol, M.V., Paquet, J. B., Radespiel, R., Reichert, T., Rival, D., Shyy, W., Ukeiley, L., Visbal, M.R., and Yuan, W., *Unsteady Aerodynamics for Micro Air Vehicles*, NATO Research and Technology Organization, NATO Technical Report, RTO-TR-AVT-149, ISBN 978-92-837-0118-7, March 2010.

[6] Davis, W.A., *Nano Air Vehicles: A Technological Forecast*. USAF, Blue Horizons Paper, Center for Strategy and Technology, Air War College, 2007.

[7] Guerrero, J., *Numerical Simulation of the Unsteady Aerodynamics of Flapping Flight*. Ph.D. Dissertation, Department of Civil, Environmental and Architectural Engineering, University of Genoa, April 2009.

[8] McMichael, J.M., and Francis, M.S., *Micro Air Vehicles – Toward a New Dimension in Flight.* Defense Advanced Research Projects Agency (DARPA), Technical Report, 1997.

[9] Mueller, T.J., and DeLaurier, J.D., *An Overview of Micro Air Vehicle Aerodynamics*. AIAA, Progress in Astronautics and Aeronautics, Fixed and Flapping Wing Aerodynamics for Micro Air Vehicle Applications, Reston, VA, Vol. 195, 2001.

[10] Liu, Z., and Moschetta, J.M., *Rotary vs. Flapping-Wing Nano Air Vehicles: Comparing Hovering Power*. The European Micro Aerial Vehicle Conference and Flight Competition (EMAV), Netherlands, 14-17 September 2009.

[11] Mueller, T.J., *Fixed and Flapping Wing Aerodynamics for Micro Air Vehicle Applications*. AIAA, Progress in Astronautics and Aeronautics, 2001.

[12] Shyy, W., Lian, Y., Tang, J., Liu, H., Trizila, P., Stanford, B., Bernal, L., Cesnik, C., Friedmann, P., and Ifju, P., *Computational Aerodynamics of Low Reynolds Number Plunging, Pitching and Flexible Wings for MAV Applications*. AIAA-2008-253-CP, 2008.

[13] Dickinson M.H., *Solving the Mystery of Insect Flight*. Scientific American, pp. 35-41, 2001.

[14] Günaydınoğlu, E., *Low Reynolds Number Aerodynamics of Flapping Airfoils in Hover and Forward Flight*. M.Sc. Dissertation, METU Aerospace Engineering Department, September 2010.

[15] Knoller, R., *Die Gesetze des Luftwiderstandes*. Flug und Motortechnik (Wien), Vol. 3, No. 21, pp. 1-7, 1909.

[16] Betz, A., *Ein Beitrag zur Erklärung des Segelfluges*. Zeitschrift für Flugtechnik und Motorluftschiffahrt, Vol. 3, pp. 269-272, 1912.

[17] Katzmayr, R., *Effect of Periodic Changes of Angle of Attack on Behavior of Airfoils*. NACA TM147, October 1922.

[18] Birnbaum, W. *Das ebene Problem des Schlagenden Flügels*. Zeitschrift für Angewandte Mathematik und Mechanik, Vol. 4, No. 4, pp. 277-292, 1924.

[19] Theodorsen, T., *General Theory of Aerodynamic Instability and the Mechanism of Flutter*. NACA Report 496, 1935.

[20] Von Kármán, T., and Burgers, J. M., *General Aerodynamic Theory - Perfect Fluids*. Aerodynamic Theory, edited by W. F. Durand, Vol. 2, Julius Springer, Berlin, p. 308, 1934.

[21] Jones, K.D, and Platzer, M.F., *Numerical Computation of Flapping Wing Propulsion and Power Extraction*. AIAA-97-0826, 1997.

[22] Isogai, K., Shinmoto, Y., and Watonobe, Y., *Effects of Dynamic Stall on Propulsive Efficiency and Thrust of a Flapping Airfoil*. AIAA Journal, Vol. 37. No. 10, October 1999.

[23] Wang, Z.J., *Vortex Shedding and Frequency Selection in Flapping Flight*. Journal of Fluid Mechanics, Vol. 410, pp. 323-341, 2000.

[24] Hall, K.C., Pigott, S.A., and Hall, S.R., *Power Requirements for Large-Amplitude Flapping Flight*. Journal of Aircraft, Vol. 35, No. 3, pp. 352-361, 1998.

[25] Wang, Z.J., *Two Dimensional Mechanism for Insect Hovering*. Physical Review Letters, Vol. 85, No. 10, September 2000.

[26] Sun, M., and Du, G., *Lift and Power Requirements of Hovering Insect Flight*. Acta Mach Sinica, Vol. 19, pp. 458-469, 2003.

[27] Wu, J.H., and Sun, M., *Unsteady Aerodynamic Forces of a Flapping Wing*. The Journal of Experimental Biology, Vol. 207, pp. 1137-1150, 2004.

[28] Wu, J.H., and Sun, M., *Unsteady Aerodynamic Forces and Power Requirements of a Bumblebee in Forward Flight*. Acta Mach Sinica, Vol. 21, pp. 207-217, 2005.

[29] Tuncer, I.H., and Kaya, M., *Thrust Generation caused by Flapping Airfoils in a Biplane Configuration*. Journal of Aircraft, Vol. 40, No. 3, pp. 509-515, 2003.

[30] Kaya, M., Tuncer, I.H., Jones, K.D., and Platzer, M.F., *Optimization of Flapping Motion Parameters for Two Airfoils in a Biplane Configuration*. Journal of Aircraft, Vol. 46, No. 2, 2009.

[31] Tuncer, I.H., and Kaya, M., *Optimization of Flapping Airfoils For Maximum Thrust and Propulsive Efficiency*. AIAA Journal, Vol. 43, pp. 2329-2341, 2005.

[32] Günaydınoğlu, E., and Kurtuluş, D.F., *Effect of Vertical Translation on Unsteady Aerodynamics of a Hovering Airfoil*. Fifth European Conference on Computational Fluid Dynamics ECCOMAS CFD 2010, Lisbon, Portugal, 14-17 June 2010.

[33] Günaydınoğlu, E., and Kurtuluş, D.F., *Reynolds Sayısının Havada Asılı Sekiz Hareketi Yapan Kanat Kesiti Aerodinamiğine Etkisi*. III. Ulusal Havacılık ve Uzay Konferansı, Eskişehir, Türkiye, 16-18 Eylül 2010.

[34] Günaydınoğlu, E., and Kurtuluş, D.F., *Numerical Investigation of Pure Plunge and Pitch/Plunge Motions at Low Reynolds Numbers*. International Symposium of Light-Weight Unmanned Aerial Vehicle Systems and Subsystems, Ostend, Belgium, 11-13 March 2009.

[35] Günaydınoğlu, E., and Kurtuluş, D.F., *Flow Characteristics of Pitching and Plunging SD7003 Airfoil for Different Reduced Frequencies*. 5th Ankara International Aerospace Conference, Ankara, Turkey, 17-19 August 2009.

[36] Günaydınoğlu, E., and Kurtuluş, D.F., *Unsteady Aerodynamic Analysis of a Flapping Flat Plate at Low Reynolds Numbers*. First International Workshop on Computational Engineering - Special Topic: Fluid-Structure Interaction, Research Unit 493 Fluid-Structure Interaction: Modeling, Simulation, Optimization, Herrsching, Germany, 12-14 October 2009.

[37] Maxworthy, T., *The Fluid Dynamics of Insect Flight*. Ann. Rev. Fluid. Mech., Vol. 13, pp. 329-350, 1981.

[38] Weis-Fogh, T., *Quick Estimates of Flight Fitness in Hovering Animals, including Novel Mechanisms for Lift Production*. The Journal of Experimental Biology, Vol. 59, pp. 169-230, 1973.

[39] Lighthill, M., *On Weis-Fogh Mechanism of Lift Generation*. Journal of Fluid Mechanics, Vol. 60, pp. 1-17, 1973.

[40] Maxworthy, T., *Experiments on the Weis-Fogh Mechanism of Lift Generation by Insects in Hovering Flight*. Journal of Fluid Mechanics, Part-I: Dynamics of the Fling, Vol. 93, pp. 47-63, 1979.

[41] Ellington, C.P., *Vortices and Hovering Flight*. In Proc. Conf. on Unsteady Effects of Oscillating Animal Wings, Saarbrucken, West Germany, November 1977.

[42] Freymuth, P., *Thrust Generation by an Airfoil in Hover Modes*. Experiments in Fluids, Vol. 9, pp. 17-24, 1990.

[43] Koochesfahani M., *Vortical Patterns in the Wake of an Oscillation Foil*. AIAA Journal, Vol. 27, pp. 1200-1205, 1989.

[44] Dickinson, M.H., *The Effects of Wing Rotation on Unsteady Aerodynamics Performance at Low Reynolds Numbers*. The Journal of Experimental Biology, Vol. 192, pp. 179-206, 1994.

[45] Dickinson, M.H., Lehmann F.O., and Sane S.P., *Wing Rotation and the Aerodynamic Basis of Insect Flight*. Science, Vol. 284, pp. 1954-1960, 1999.

[46] Anderson, J.M., Streitlien, K., Borrett, D.S., Triantafyllou, M.S., *Oscillating Foils of High Propulsive Efficiency*. Journal of Fluid Mechanics, Vol. 360, pp. 41-72, 1998.

[47] Lai J., and Platzer M.F., *Jet Characteristics of a Plunging Airfoil*. AIAA Journal, Vol. 37, pp. 1529-1537, 1999.

[48] Singh, B., Ramasamy, M., Chopra, I., and Leishman, G.J., *Experimental Studies on Insect-Based Flapping Wings for Micro Hovering Air Vehicles*. AIAA, Vol. 20742, 2004.

[49] Schouveiler L., Hover F.S., and Triantafyllou M.S., *Performance of Flapping Foil Propulsion*. Journal of Fluids and Structures, Vol. 20, pp. 949-959, 2005.

[50] Map of Life, *Swimming and Thermoregulation in Sharks and Tuna*. http://www.mapoflife.org/topics/topic_118_Swimming-and-thermoregulation-in-sharks-and-tuna/ (Last accessed date: 10 September 2012).

[51] Lehmann, F.O., Sane, S.P., and Dickinson, M.H., *The Aerodynamic Effect of Wing-Wing Interaction in Flapping Insect Wings*. The Journal of Experimental Biology, Vol. 208. pp. 3075-3092, 2005.

[52] Lehmann, F.O., and Pick, S., *The Aerodynamic Benefit of Wing–Wing Interaction Depends on Stroke Trajectory in Flapping Insect Wings*. The Journal of Experimental Biology, Vol. 210, pp.1362-1377, 2007.

[53] Poelma, C., Dickson, W.B., and Dickinson, M.H., *Time-resolved Reconstruction of the Full Velocity Field around a Dynamically-scaled Flapping Wing*. Experiment in Fluids, Vol. 41, pp. 213-225, 2006.

[54] Tian, X., Iriarte, J., Middleton, K., Galvao, R., Israeli, E., Roemer, A., Sullivan, A., Song, A., Swartz, S., and Breuer, K., *Direct Measurement of the Kinematics and Dynamics of Bat Flight*. 36th AIAA Fluid Dynamics Conference and Exhibit, San Francisco, California, 5-8 June 2006.

[55] Daichin, Kang, W., Zhao, L., *PIV Measurements of the Near Wake Flow of an Airfoil above a Free Surface*. ScienceDirect, Journal of Hydrodynamics, Ser. B, Vol. 19, No. 4, pp. 482-487, 2007.

[56] Ol, M.V., *Vortical Structures in High Frequency Pitch and Plunge at Low Reynolds Number*. 37th AIAA Fluid Dynamics Conference and Exhibit, Miami, FL, 25-28 June 2007.

[57] Hu, H., Clemons, L., and Igarashi, H., *An Experimental Study of the Unsteady Vortex Structures in the Wake of a Root-Fixed Flapping Wing*. Experiments in Fluids, Vol. 51, pp. 347-359, 2011.

[58] Platzer, M.F., and Jones, K.D., *Flapping Wing Aerodynamics – Progress and Challenges*. Reno, Nevada, AIAA-06-0500, 2006.

[59] Jones, K.D., Dohring, C.M., Platzer, M.F., *Wake Structures behind Plunging Airfoils: A Comparison of Numerical and Experimental Results*. AIAA-96-0078, 1996.

[60] Jones, K.D., Dohring, C.M., Platzer, M.F., *Experimental and Computational Investigation of the Knoller-Betz Effect*. AIAA Journal, Vol. 36, No. 7, July 1998.

[61] Jones, K.D., Castro, B.M., Mahmoud O., and Platzer M.F., *A Numerical and Experimental Investigation of Flapping Wing Propulsion in Ground Effect*. AIAA-2002-0866, 2002.

[62] Wang Z.J., Birch J.M., and Dickinson M.H., *Unsteady Forces and Flows in Low Reynolds Number Hovering: Two-Dimensional Computations vs. Robotic Wing Experiments*. The Journal of Experimental Biology, Vol. 207, pp. 449-450, 2004.

[63] Kurtuluş, D.F., *Numerical and Experimental Analysis of Flapping Motion in Hover. Application to Micro Air Vehicle*. Joint Ph.D. Thesis, Poitiers University/ENSMA (Poitiers-France) and METU (Ankara-Turkey), June 2005.

[64] Perçin, M., Mısırlıoğlu, A., and Ünal, M.F., *Flow around a Plunging Airfoil in a Uniform Flow*. 5th Ankara International Aerospace Conference (AIAC), Ankara, Turkey, 17-19 August 2009.

[65] Ol, M.V., Eldredge, J.D., and Wang, C., *High-Amplitude Pitch of a Flat Plate: an Abstraction of Perching and Flapping*. International Journal of Micro Air Vehicles, Vol. 1, No. 3, pp. 203-216, 2009.

[66] Hızlı, H., and Kurtuluş, D.F., *Numerical and Experimental Analysis of Purely Pitching and Purely Plunging Airfoils in Hover*. 5th International Micro Air Vehicle Conference and Flight Competition (IMAV), Braunschweig, Germany, 03-06 July 2012.

[67] Hızlı, H., and Kurtuluş, D.F., *Experimental and Numerical Investigation of Pitching Airfoils in Hover*. 6th Ankara International Aerospace Conference (AIAC), Ankara, Turkey, 14-16 September 2011.

[68] *Fluent v6.3 User's Guide*. 2006.

[69] *Fluent v6.3 UDF Manual*. 2006.

[70] Kundu, P.K., and Cohen, I.M., *Fluid Mechanics*. 3rd Ed., Academic Press, 2004.

[71] Kurtuluş, D.F., Farcy, A., and Alemdaroğlu, N., *Unsteady Aerodynamics of Flapping Airfoil in Hovering Flight at Low Reynolds Numbers*. 43rd AIAA Aerospace Sciences Meeting and Exhibit, Reno, Nevada, 10-13 January 2005.

[72] Kurtuluş, D.F., David, L., Farcy, A., and Alemdaroğlu, N., *Aerodynamic Characteristics of Flapping Motion in Hover*. Experiments in Fluids, Vol. 44, pp. 23-36, 2008.

[73] Grant, I., Owens, E., and Yan, Y., *Particle Image Velocimetry Measurements of the Separated Flow behind a Reward Facing Step*. Experiments in Fluids, Vol. 12, pp. 238-244, 1992.

[74] Dantec Dynamics, *Particle Image Velocimetry Solutions*. http://www.dantecdynamics.com/Default.aspx?ID=20415 (Last accessed date: 10 September 2012).

[75] Koechner, W., *Solid-State Laser Engineering*. *2nd Ed*., New York: Springer-Verlag, Ch. 2.3, pp. 48-53, 1988.

[76] Uzol, O., and Katz, J., *Flow Measurement Techniques in Turbomachinery*. Springer Handbook of Experimental Fluid Mechanics, Sec. 14, pp. 919-958, 2007.

[77] Durmaz, O., *Dynamical Modeling of the Flow over Flapping Wing by Applying Proper Orthogonal Decomposition and System Identification*. M.Sc. Dissertation, METU Aerospace Engineering Department, September 2011.

[78] Azuma, A., Masato, O., and Kunio, Y., *Aerodynamic Characteristics of Wings at Low Reynolds Numbers, Fixed and Flapping Wings*. Astro. & Aero., Aerodynamics for Micro Air Vehicle Applications, Vol. 195, pp. 341-398, 2001.

[79] Kostas, J., Soria, J., and Chong, M., *Particle Image Velocimetry Measurements of a Backward-Facing Step Flow*. Experiments in Fluids, Vol. 33, pp. 838-853, 2002.

[80] Dantec Dynamics, *Particle Image Velocimetry Measurement Principles*. http://www.dantecdynamics.com/Default.aspx?ID=1049 (Last accessed date: 10 September 2012).

[81] Dantec Dynamics, *DynamicStudio - Smart Software for Imaging Solutions*. http://www.dantecdynamics.com/Default.aspx?ID=740 (Last accessed date: 10 September 2012).

[82] Platzer M.F., and Jones K.D., *The Unsteady Aerodynamics of Flapping-Foil Propellers*. 9th International Symposium on Unsteady Aerodynamics, Aeroacoustics and Aeroelasticity of Turbomachines, Ecole Centrale de Lyon, France, September 2000.

[83] Birch J.M., Dickinson M.H., *The Influence of Wing-Wake Interactions on the Production of Aerodynamic Forces in Flapping Flight*. The Journal of Experimental Biology, Vol. 206, pp. 2257-2272, 2003.

APPENDIX A

RESULTS OF THE CASE STUDIES

The results obtained from the numerical simulations and experimental visualizations of the test cases, which are not discussed in Chapter 5 in order not to have any confusion in that chapter, are presented in this section. These test cases are studied in order to investigate the effects of pitching and plunging amplitudes and also airfoil geometries on the constant frequency hovering motion in more detail by increasing the size of the parameter space. As in the case of baseline test cases discussed in Chapter 5, all the results presented in this section are also for the sixth period of the motion.

The results obtained are presented in terms of the instantaneous vortex topologies for the each studied case. The aerodynamic force and moment coefficient history graphs corresponding to the desired period of the motion are also presented at the end of the section. Similar results obtained for the baseline test cases are obtained from the numerical and experimental studies of these test cases and it can be said that the good agreement between the numerical and experimental results in terms of the unsteady vortex fields observed in the baseline test cases is confirmed for these test cases too.

A.1 Results of the Pure Pitch Motion

A.1.1 SD7003 Airfoil Undergoing Pure Pitch Motion

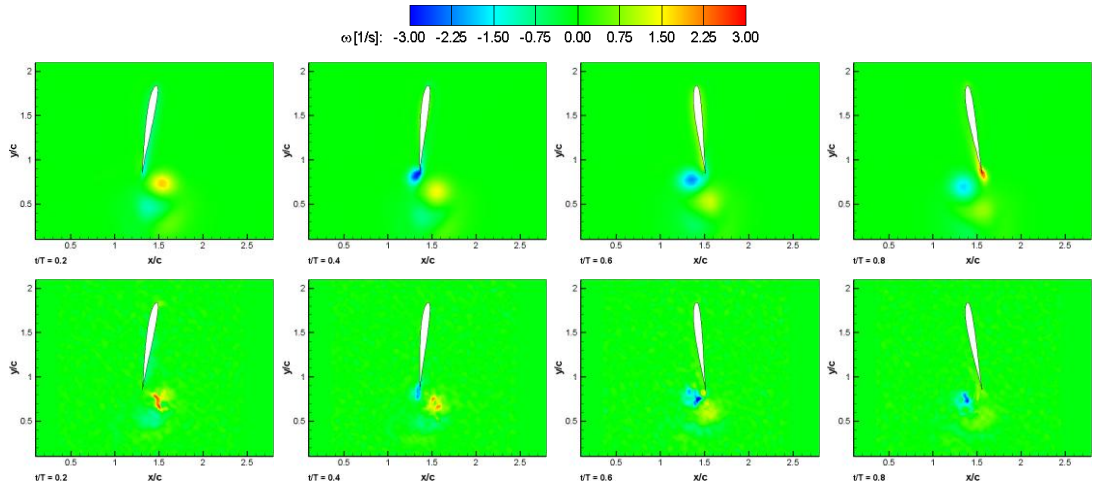

Figure A.1.1 Instantaneous vorticity contours for purely pitching ($\alpha_a=10^o$; $k=11.5$) SD7003 airfoil (2-D CFD: top row, PIV: bottom row).

A.1.2 NACA0012 Airfoil Undergoing Pure Pitch Motion

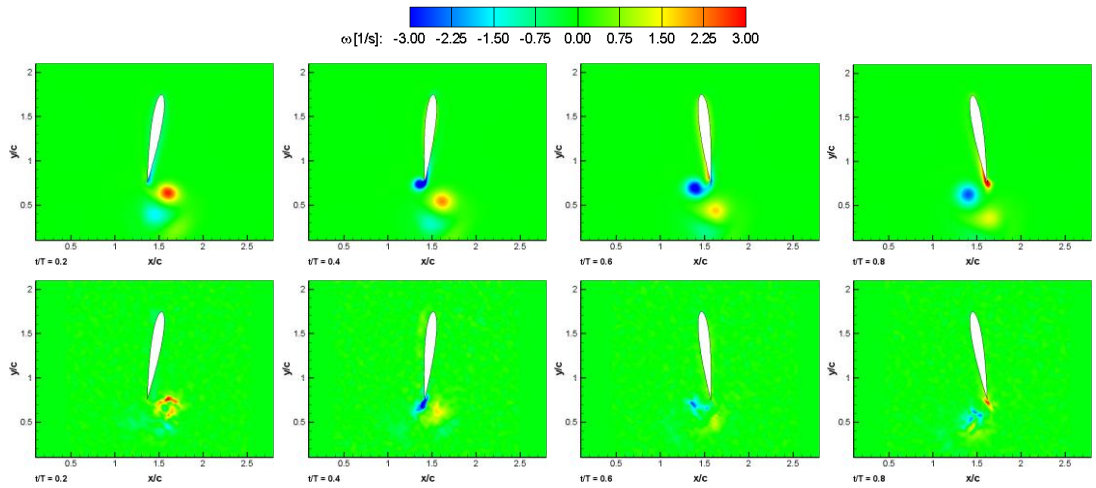

Figure A.1.2 Instantaneous vorticity contours for purely pitching ($\alpha_a=10^o$; $k=11.5$) NACA0012 airfoil (2-D CFD: top row, PIV: bottom row).

A.1.3 10% Thick Elliptical Airfoil Undergoing Pure Pitch Motion

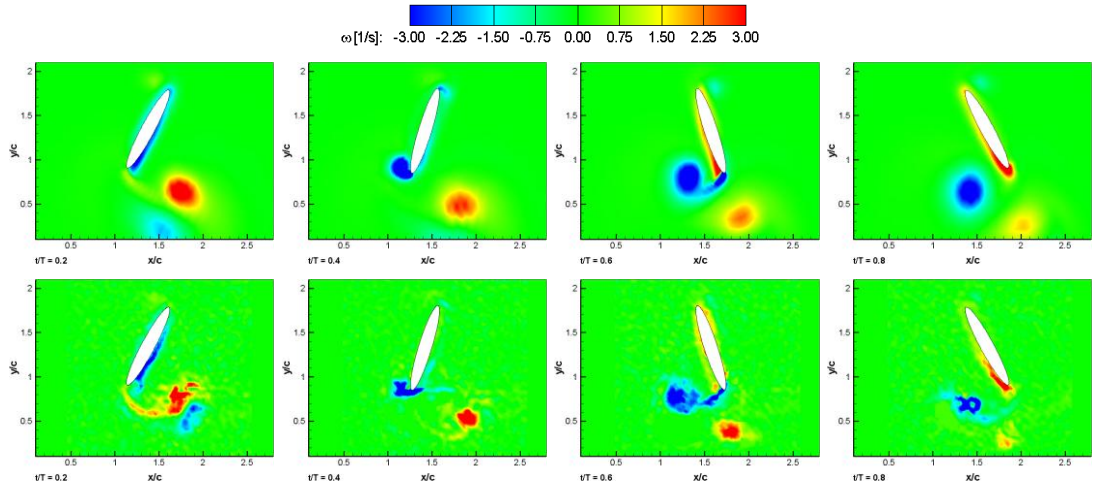

Figure A.1.3 Instantaneous vorticity contours for purely pitching ($\alpha_a=30^o$; $k=3.8$) 10% thick elliptical airfoil (2-D CFD: top row, PIV: bottom row).

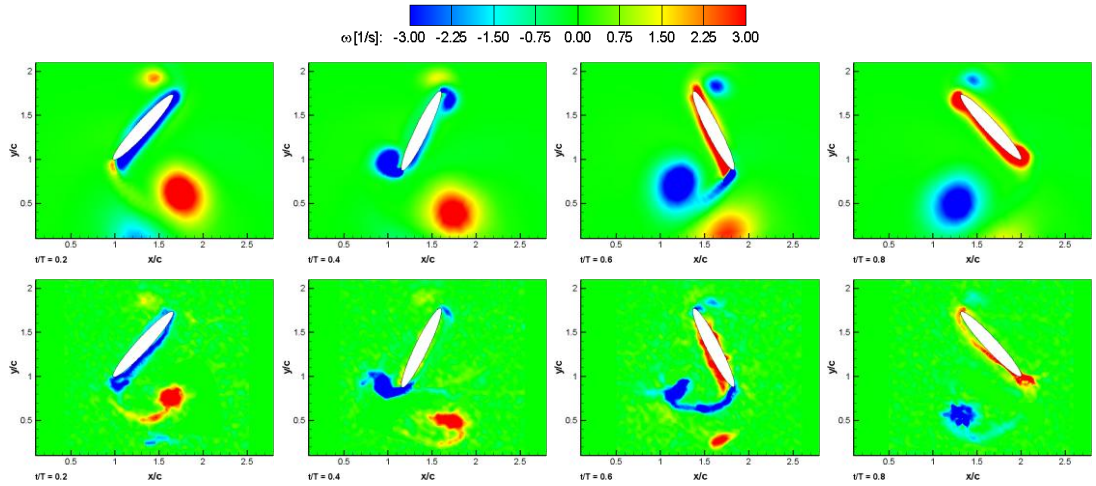

Figure A.1.4 Instantaneous vorticity contours for purely pitching ($\alpha_a=45^o$; $k=2.5$) 10% thick elliptical airfoil (2-D CFD: top row, PIV: bottom row).

A.1.4 10% Thick Flat Plate Airfoil Undergoing Pure Pitch Motion

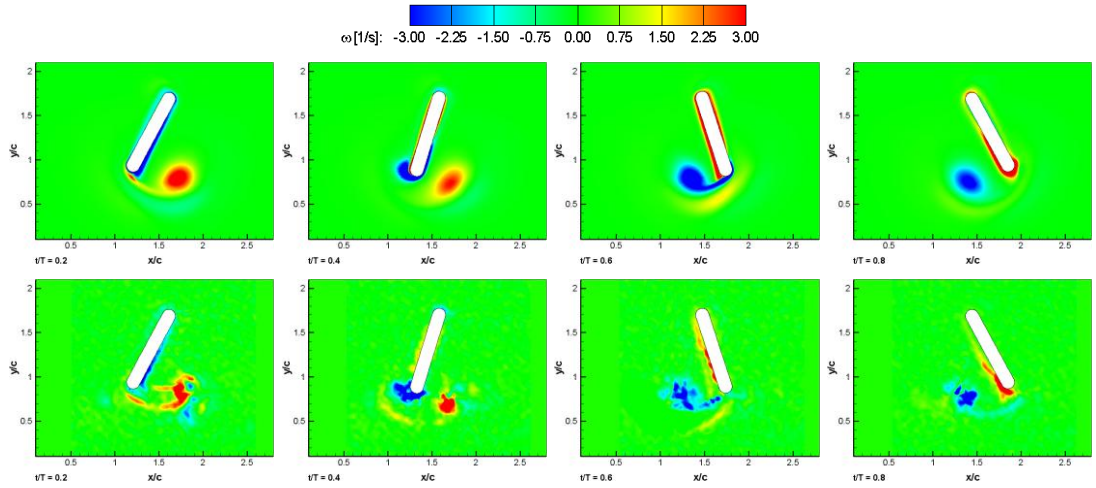

Figure A.1.5 Instantaneous vorticity contours for purely pitching ($\alpha_a=30^o$; $k=3.8$) 10% thick flat plate airfoil (2-D CFD: top row, PIV: bottom row).

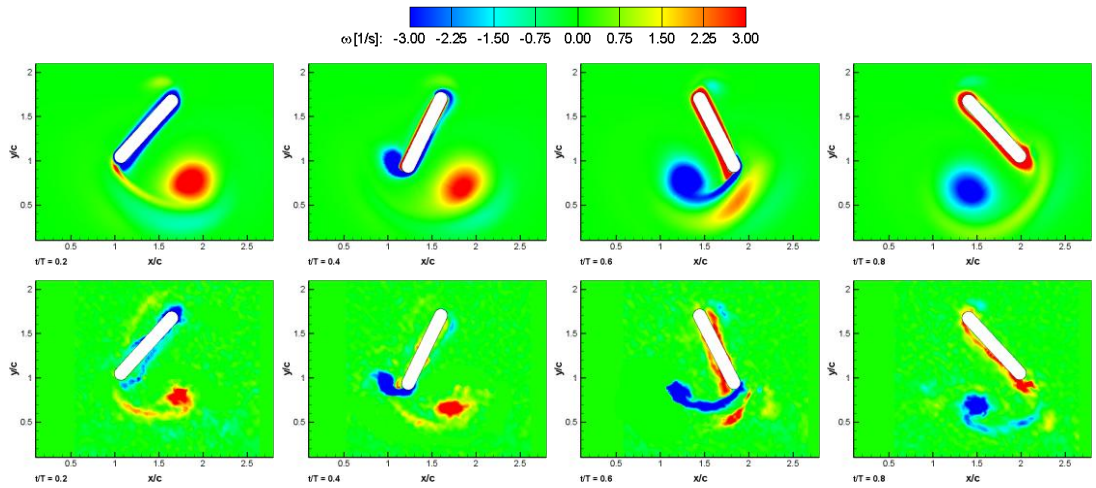

Figure A.1.6 Instantaneous vorticity contours for purely pitching ($\alpha_a=45^o$; $k=2.5$) 10% thick flat plate airfoil (2-D CFD: top row, PIV: bottom row).

A.2 Results of the Pure Plunge Motion

A.2.1 SD7003 Airfoil Undergoing Pure Plunge Motion

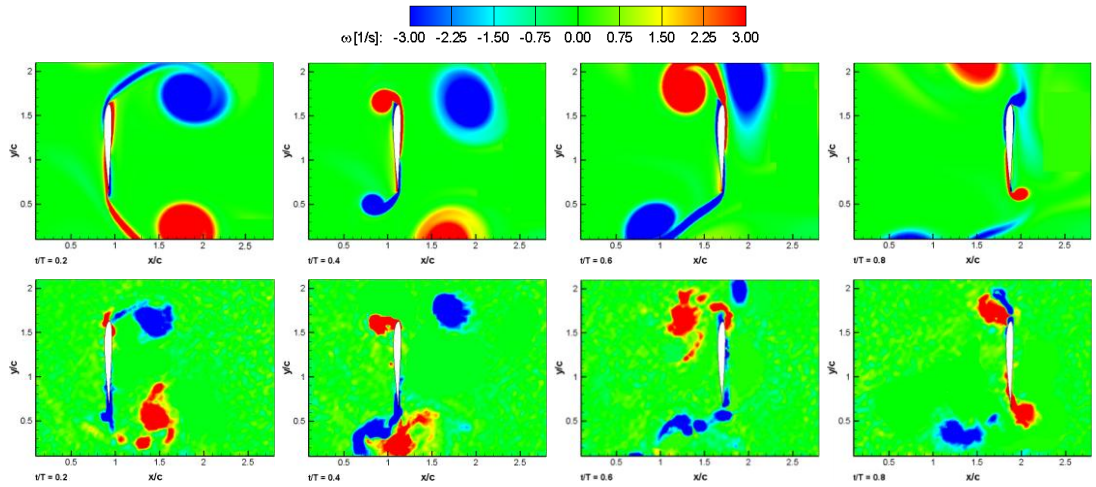

Figure A.2.1 Instantaneous vorticity contours for purely plunging (x_a=*0.03 m; k=1.0*) SD7003 airfoil (2-D CFD: top row, PIV: bottom row).

A.2.2 NACA0012 Airfoil Undergoing Pure Plunge Motion

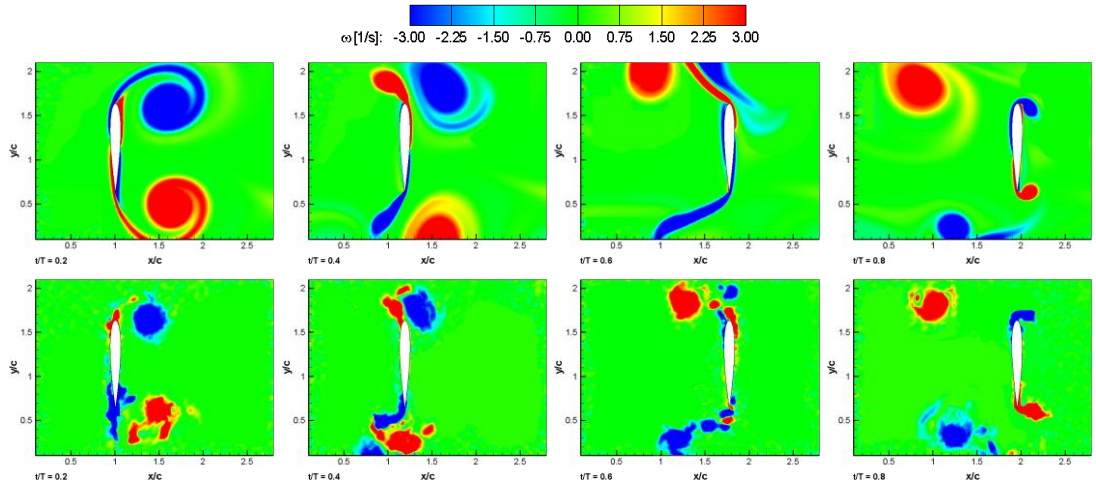

Figure A.2.2 Instantaneous vorticity contours for purely plunging (x_a=*0.03 m; k=1.0*) NACA0012 airfoil (2-D CFD: top row, PIV: bottom row).

A.2.3 10% Thick Elliptical Airfoil Undergoing Pure Plunge Motion

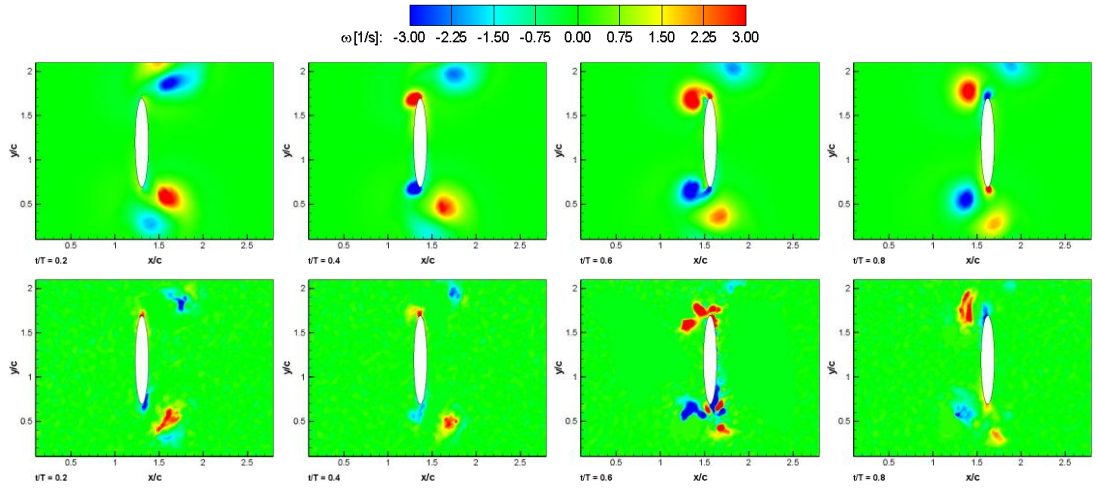

Figure A.2.3 Instantaneous vorticity contours for purely plunging (x_a=*0.01 m; k=3.0*) 10% thick elliptical airfoil (2-D CFD: top row, PIV: bottom row).

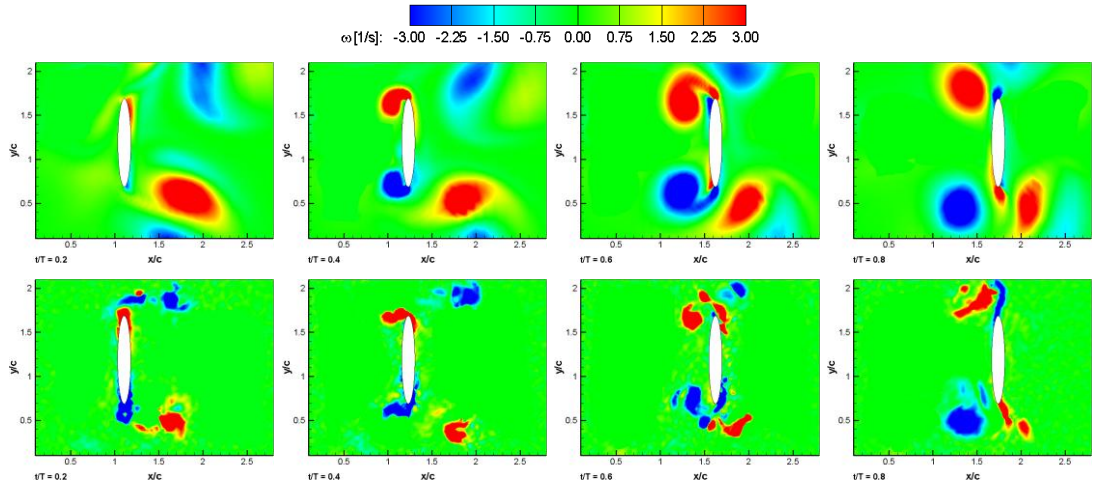

Figure A.2.4 Instantaneous vorticity contours for purely plunging (x_a=*0.02 m; k=1.5*) 10% thick elliptical airfoil (2-D CFD: top row, PIV: bottom row).

A.2.4 10% Thick Flat Plate Airfoil Undergoing Pure Plunge Motion

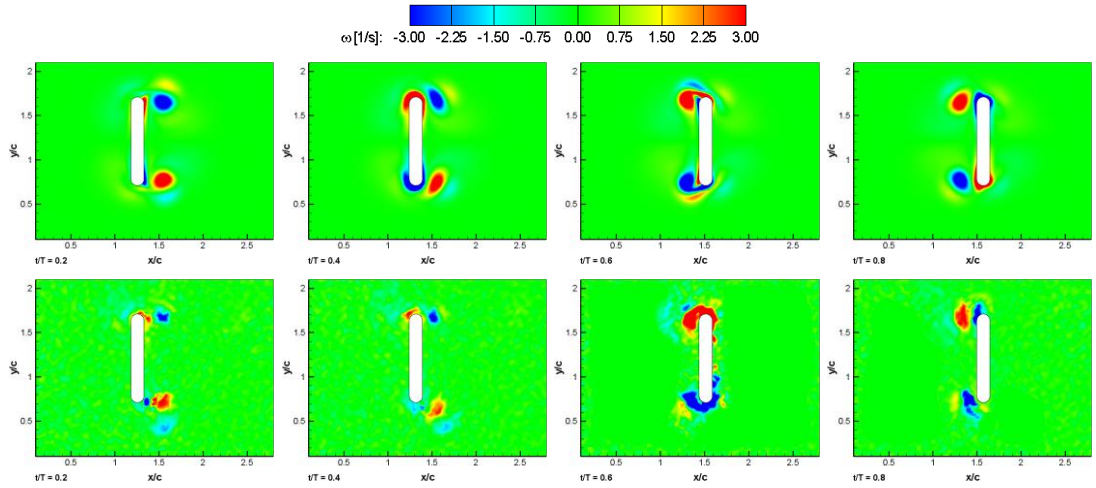

Figure A.2.5 Instantaneous vorticity contours for purely plunging (x_a=*0.01 m; k=3.0*) 10% thick flat plate airfoil (2-D CFD: top row, PIV: bottom row).

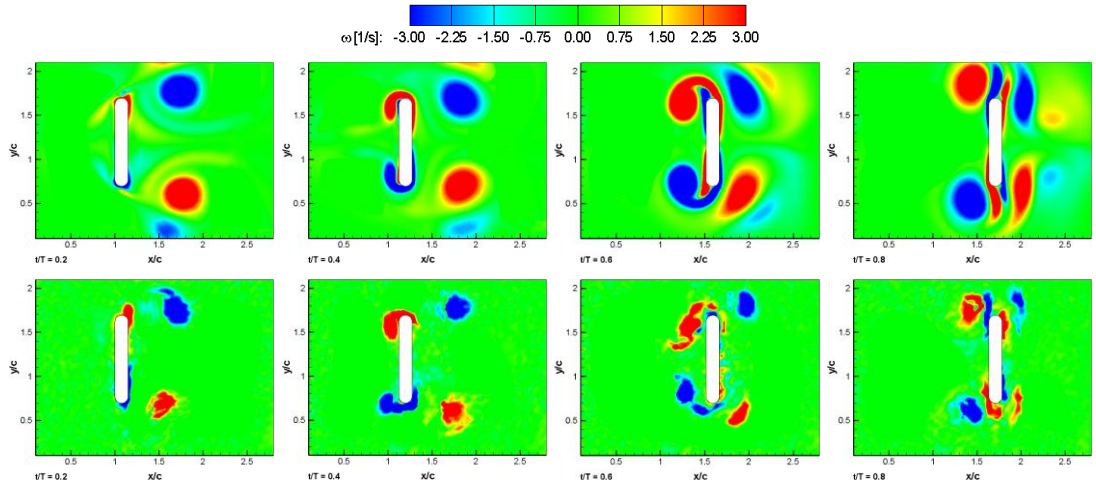

Figure A.2.6 Instantaneous vorticity contours for purely plunging (x_a=*0.02 m; k=1.5*) 10% thick flat plate airfoil (2-D CFD: top row, PIV: bottom row).

A.3 Results of the Combined Pitch-Plunge Motion

A.3.1 SD7003 Airfoil Undergoing Combined Pitch-Plunge Motion

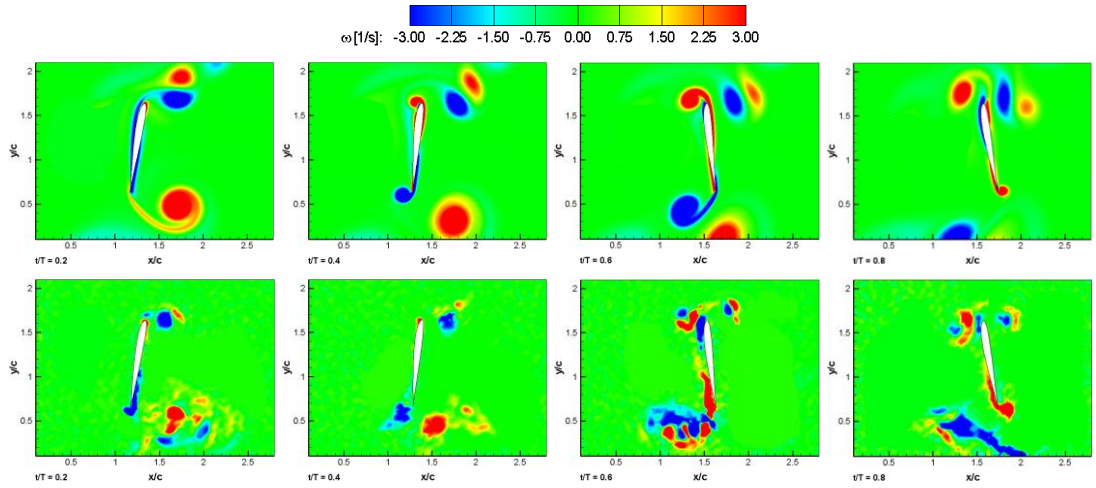

Figure A.3.1 Instantaneous vorticity contours for pitching-plunging ($\alpha_a=10^o$, $x_a=0.01$ *m;* $k=2.9$) SD7003 airfoil (2-D CFD: top row, PIV: bottom row).

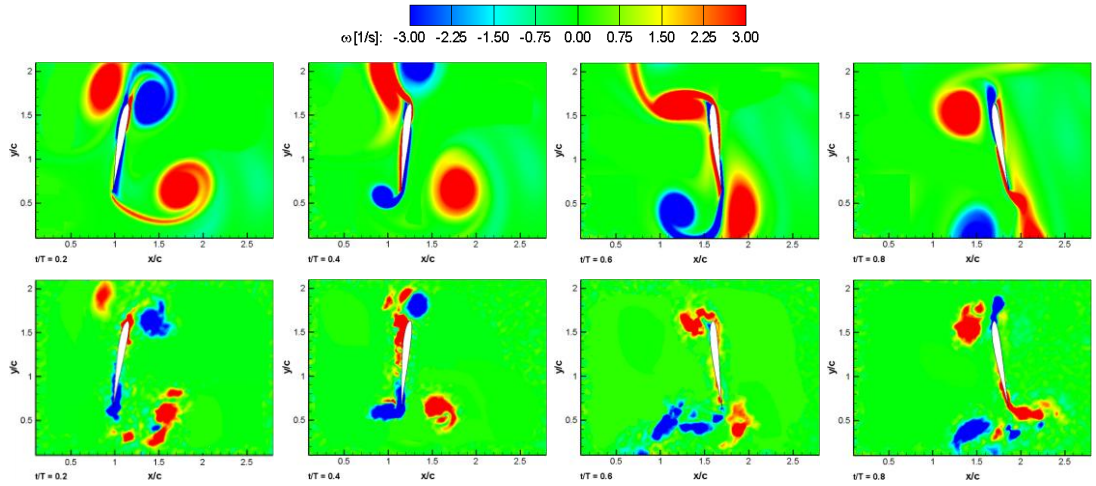

Figure A.3.2 Instantaneous vorticity contours for pitching-plunging ($\alpha_a=10^o$, $x_a=0.02$ *m;* $k=1.5$) SD7003 airfoil (2-D CFD: top row, PIV: bottom row).

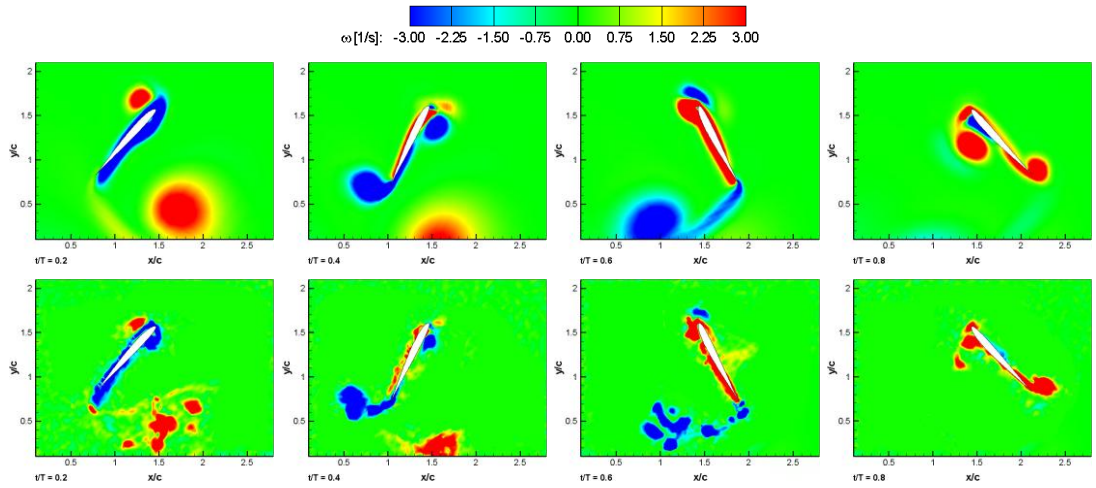

Figure A.3.3 Instantaneous vorticity contours for pitching-plunging (α_a=45^o, x_a=*0.01 m; k=1.9*) SD7003 airfoil (2-D CFD: top row, PIV: bottom row).

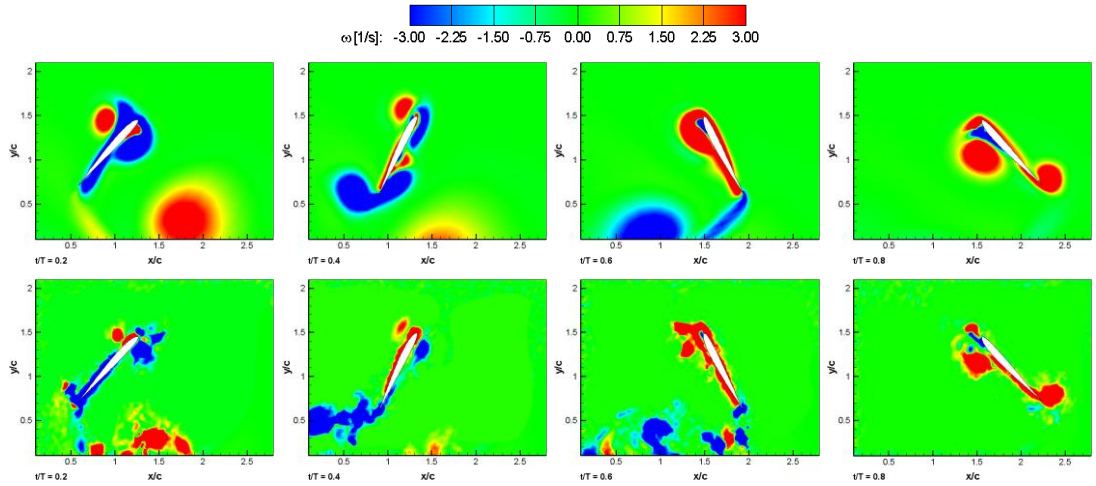

Figure A.3.4 Instantaneous vorticity contours for pitching-plunging (α_a=45^o, x_a=*0.02 m; k=1.3*) SD7003 airfoil (2-D CFD: top row, PIV: bottom row).

A.3.2 NACA0012 Airfoil Undergoing Combined Pitch-Plunge Motion

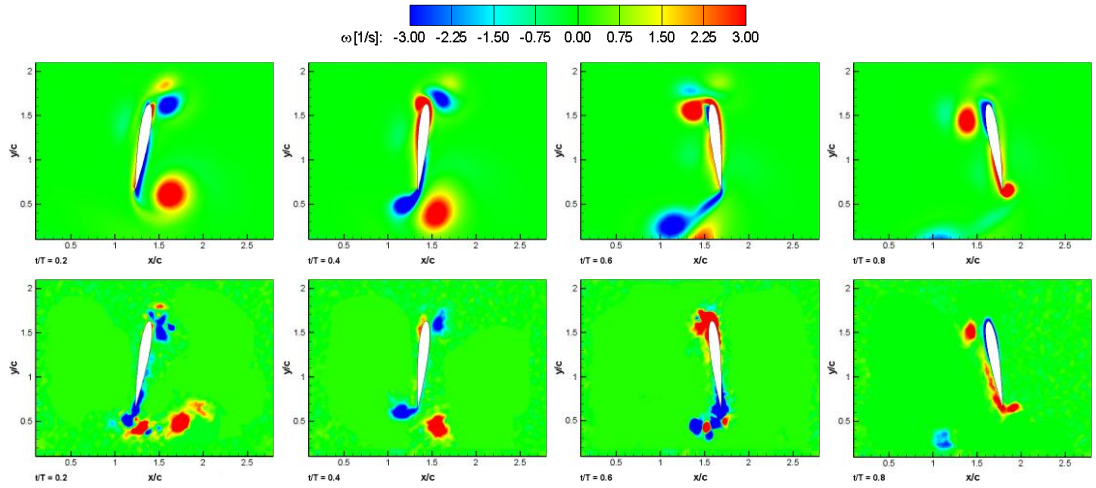

Figure A.3.5 Instantaneous vorticity contours for pitching-plunging ($\alpha_a=10^o$, $x_a=0.01$ *m;* $k=2.9$) NACA0012 airfoil (2-D CFD: top row, PIV: bottom row).

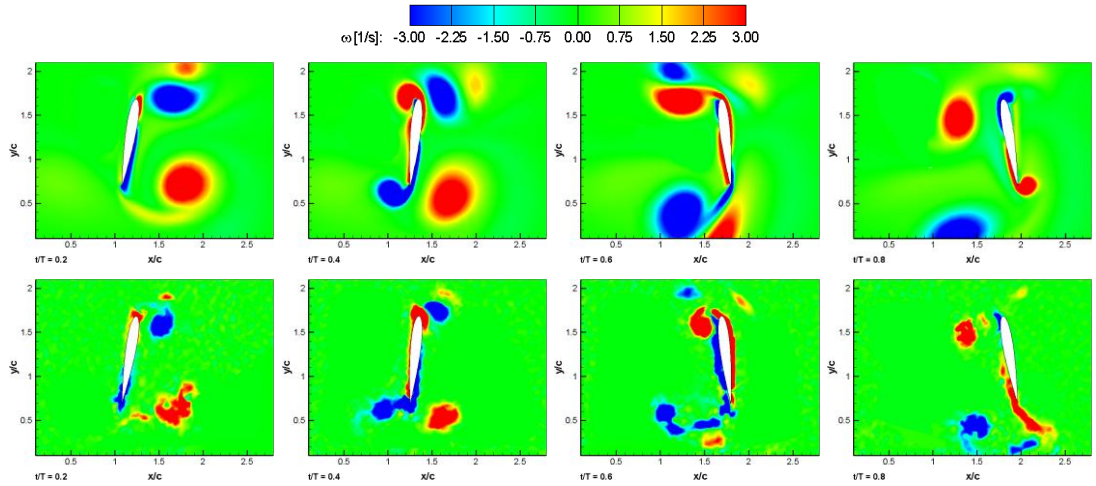

Figure A.3.6 Instantaneous vorticity contours for pitching-plunging ($\alpha_a=10^o$, $x_a=0.02$ *m;* $k=1.5$) NACA0012 airfoil (2-D CFD: top row, PIV: bottom row).

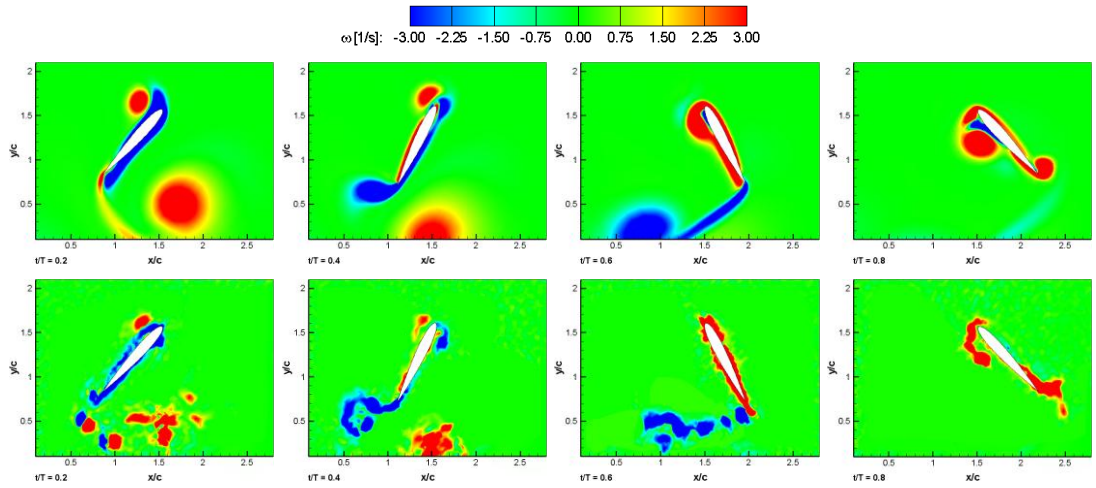

Figure A.3.7 Instantaneous vorticity contours for pitching-plunging (α_a=45^o, x_a=0.01 *m; k=1.9*) NACA0012 airfoil (2-D CFD: top row, PIV: bottom row).

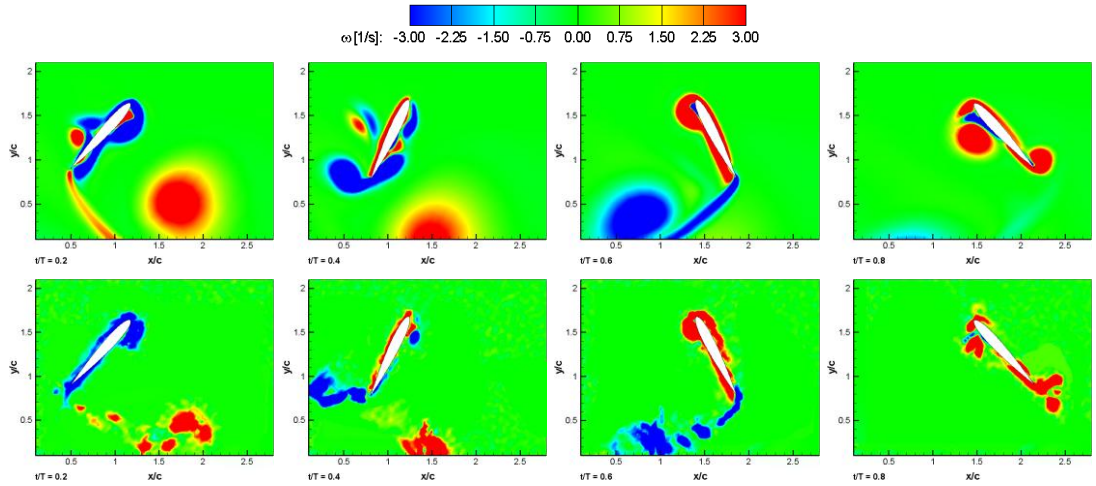

Figure A.3.8 Instantaneous vorticity contours for pitching-plunging (α_a=45^o, x_a=0.02 *m; k=1.3*) NACA0012 airfoil (2-D CFD: top row, PIV: bottom row).

A.3.3 10% Thick Elliptical Airfoil Undergoing Combined Pitch-Plunge Motion

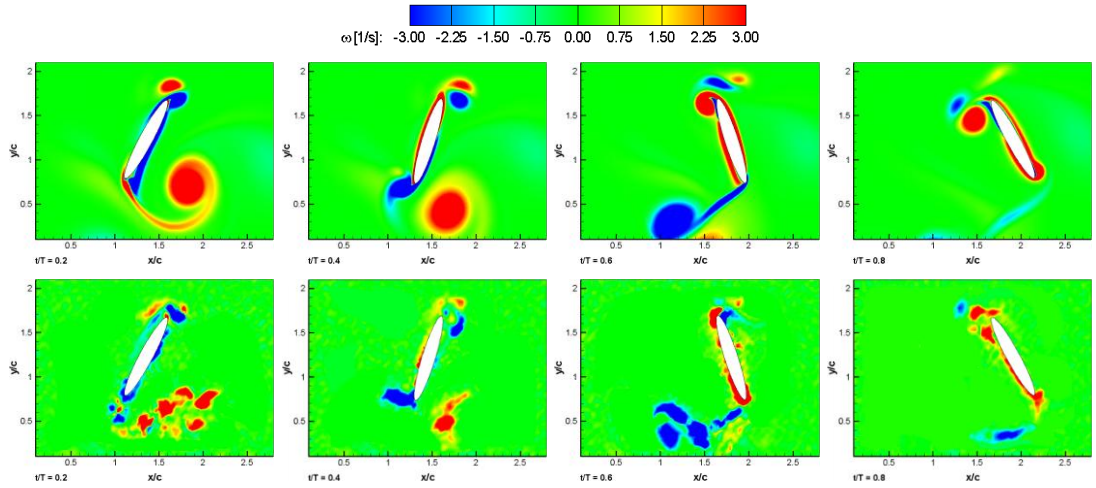

Figure A.3.9 Instantaneous vorticity contours for pitching-plunging ($\alpha_a=30^o$, $x_a=0.01$ *m;* $k=2.4$) 10% thick elliptical airfoil (2-D CFD: top row, PIV: bottom row)

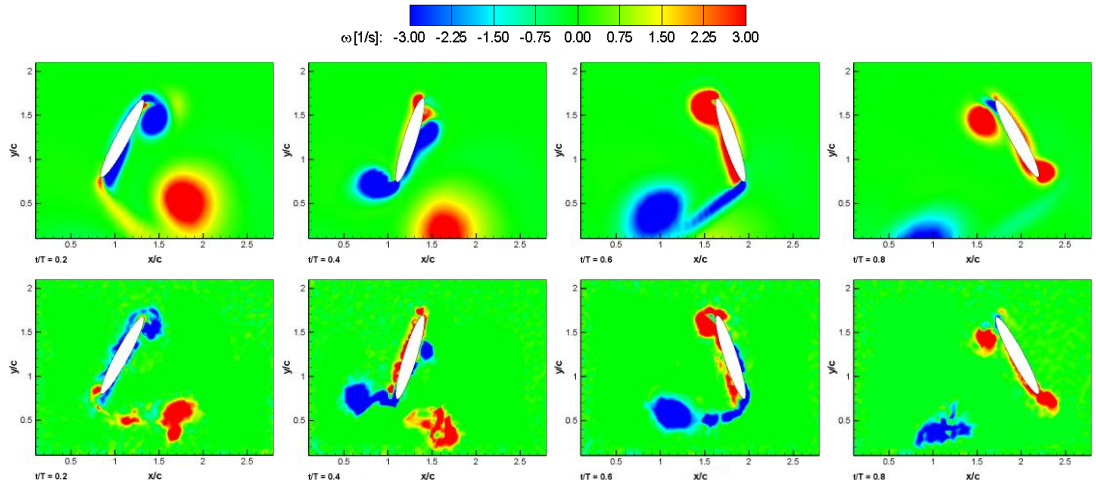

Figure A.3.10 Instantaneous vorticity contours for pitching-plunging ($\alpha_a=30^o$, $x_a=0.02$ *m;* $k=1.4$) 10% thick elliptical airfoil (2-D CFD: top row, PIV: bottom row).

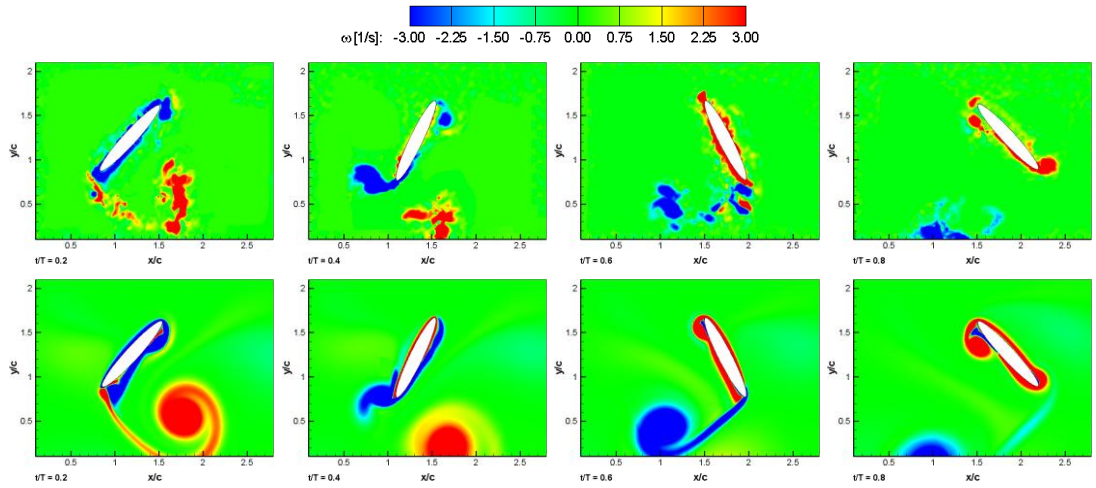

Figure A.3.11 Instantaneous vorticity contours for pitching-plunging (α_a=45^o, x_a=*0.01 m; k=1.9*) 10% thick elliptical airfoil (2-D CFD: top row, PIV: bottom row).

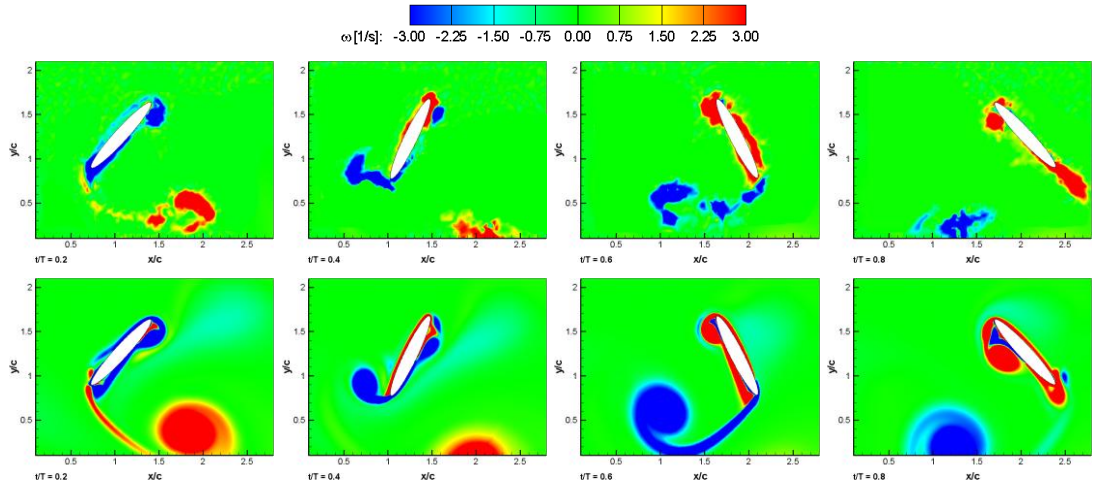

Figure A.3.12 Instantaneous vorticity contours for pitching-plunging (α_a=45^o, x_a=*0.02 m; k=1.3*) 10% thick elliptical airfoil (2-D CFD: top row, PIV: bottom row).

A.4 Comparison of the Aerodynamic Force and Moment Coefficients

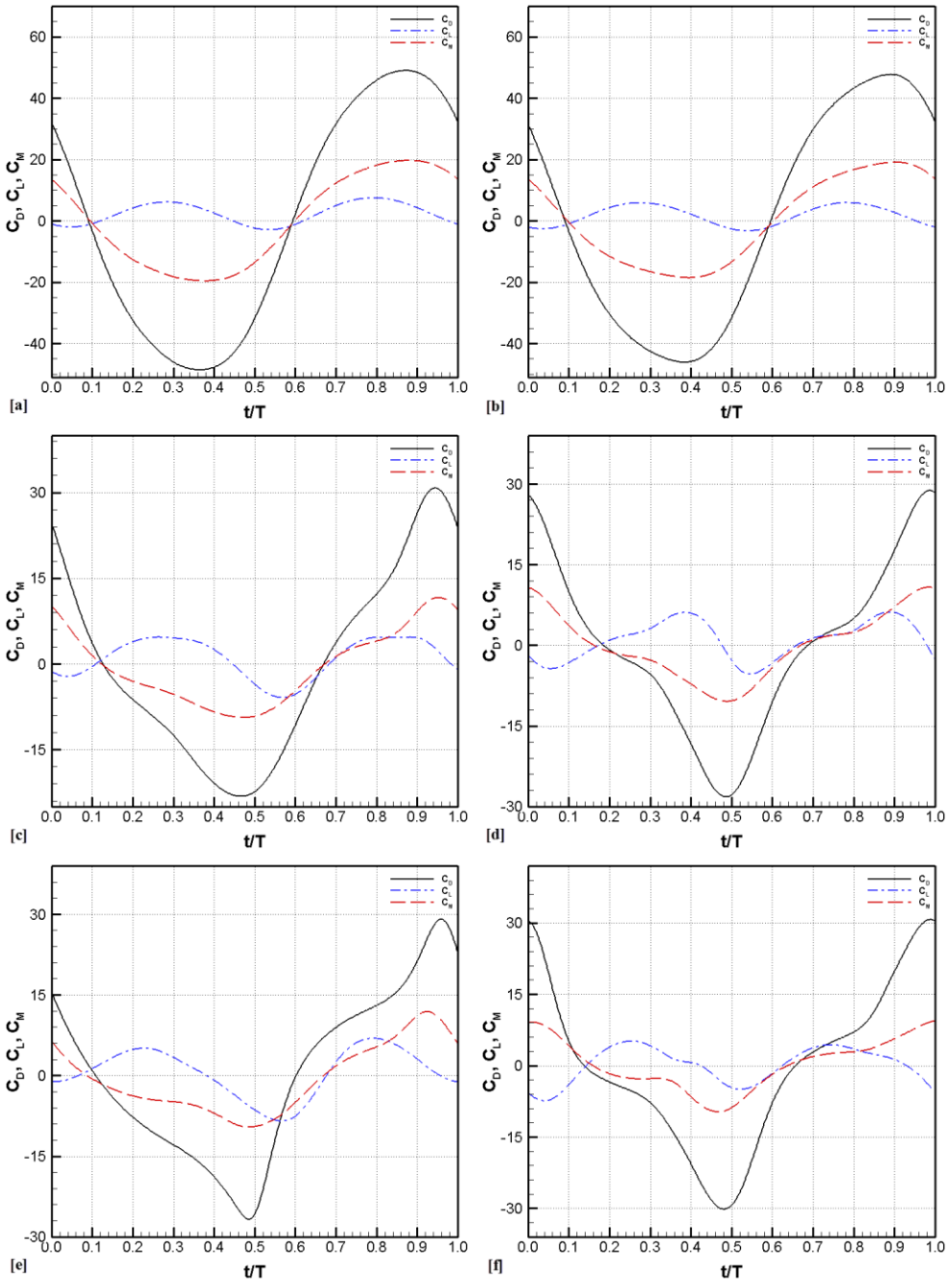

Figure A.4.1 Time histories of lift, drag and moment coefficients obtained from 2-D CFD for purely pitching: [a] SD7003 airfoil ($\alpha_a=10^o$; $k=11.5$), [b] NACA0012 airfoil ($\alpha_a=10^o$; $k=11.5$), [c] 10% thick elliptical airfoil ($\alpha_a=30^o$; $k=3.8$), [d] 10% thick elliptical airfoil ($\alpha_a=45^o$; $k=2.5$), [e] 10% thick flat plate airfoil ($\alpha_a=30^o$; $k=3.8$), [f] 10% thick flat plate airfoil ($\alpha_a=45^o$; $k=2.5$).

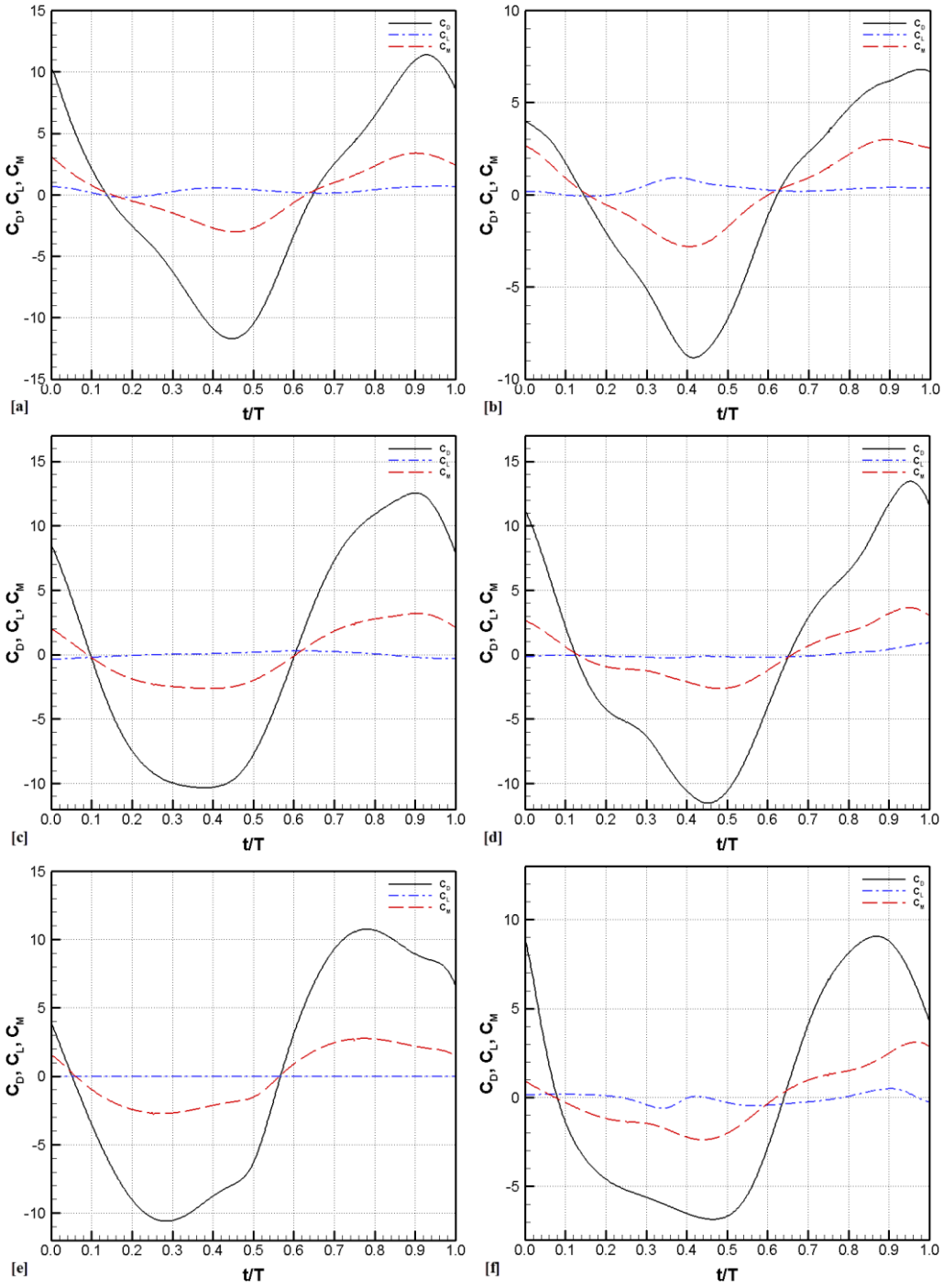

Figure A.4.2 Time histories of lift, drag and moment coefficients obtained from 2-D CFD for purely plunging: [a] SD7003 airfoil (x_a=*0.03 m; k=1.0*), [b] NACA0012 airfoil (x_a=*0.03 m; k=1.0*), [c] 10% thick elliptical airfoil (x_a=*0.01 m; k=3.0*), [d] 10% thick elliptical airfoil (x_a=*0.02 m; k=1.5*), [e] 10% thick flat plate airfoil (x_a=*0.01 m; k=3.0*), [f] 10% thick flat plate airfoil (x_a=*0.02 m; k=1.5*).

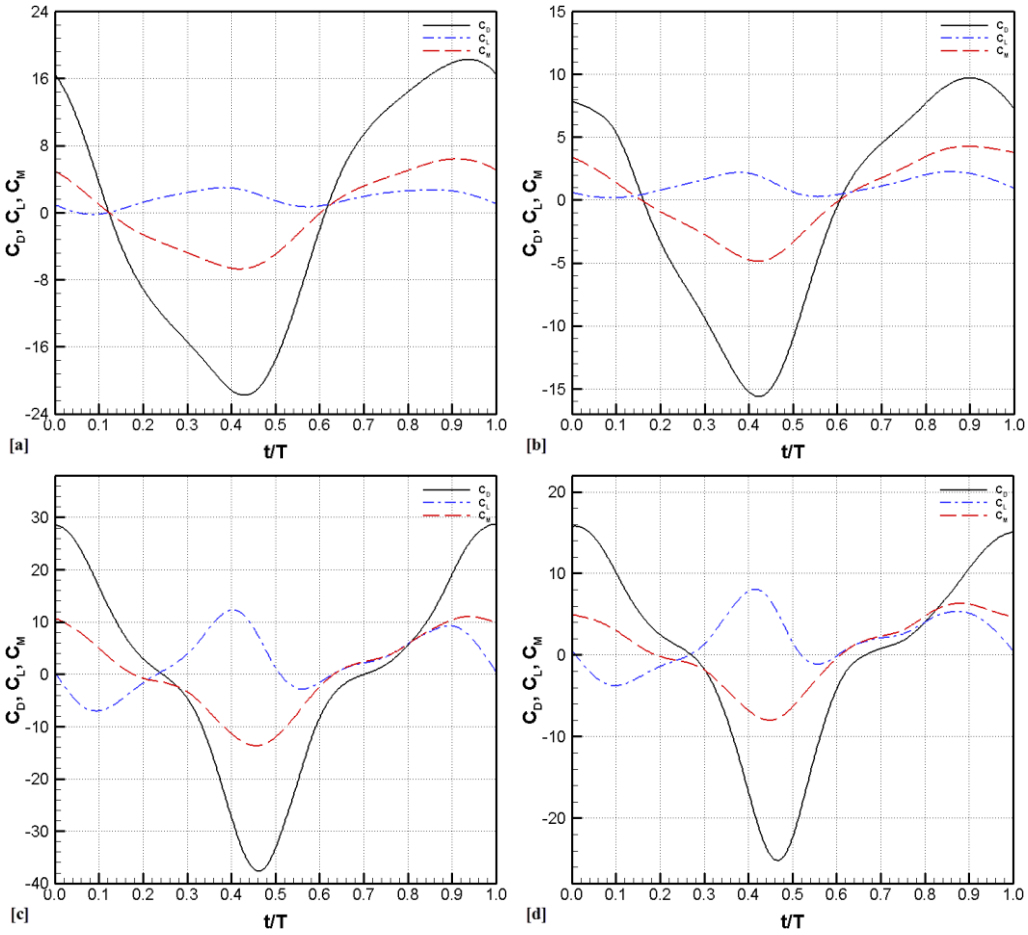

Figure A.4.3 Time histories of lift, drag and moment coefficients obtained from 2-D CFD for pitching-plunging SD7003 airfoil: [a] $\alpha_a=10^o$, $x_a=0.01$ *m; k=2.9* case, [b] $\alpha_a=10^o$, $x_a=0.02$ *m; k=1.5* case, [c] $\alpha_a=45^o$, $x_a=0.01$ *m; k=1.9* case, [d] $\alpha_a=45^o$, $x_a=0.02$ *m; k=1.3* case.

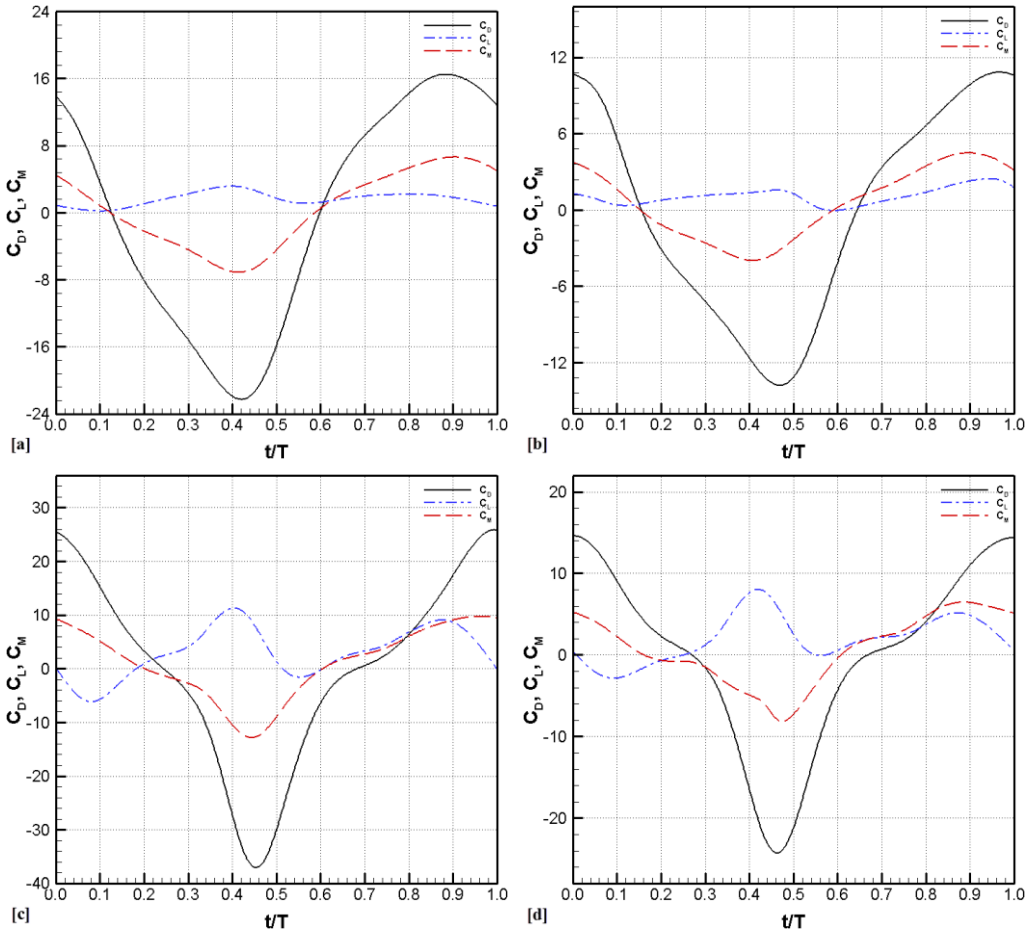

Figure A.4.4 Time histories of lift, drag and moment coefficients obtained from 2-D CFD for pitching-plunging NACA0012 airfoil: [a] $\alpha_a=10^o$, $x_a=0.01$ *m; k=2.9* case, [b] $\alpha_a=10^o$, $x_a=0.02$ *m; k=1.5* case, [c] $\alpha_a=45^o$, $x_a=0.01$ *m; k=1.9* case, [d] $\alpha_a=45^o$, $x_a=0.02$ *m; k=1.3* case.

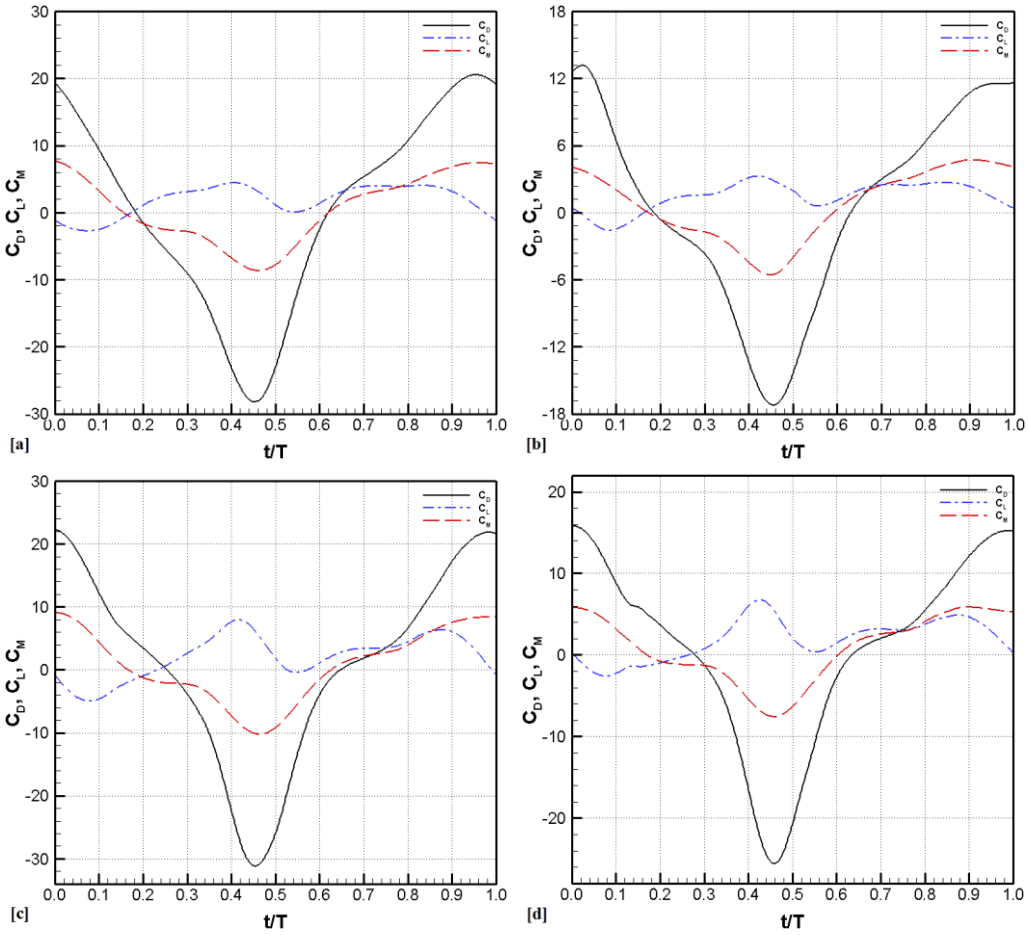

Figure A.4.5 Time histories of lift, drag and moment coefficients obtained from 2-D CFD for pitching-plunging 10% thick elliptical airfoil: [a] $\alpha_a=30^o$, $x_a=0.01$ *m; k=2.4* case, [b] $\alpha_a=30^o$, $x_a=0.02$ *m; k=1.4* case, [c] $\alpha_a=45^o$, $x_a=0.01$ *m; k=1.9* case, [d] $\alpha_a=45^o$, $x_a=0.02$ *m; k=1.3* case.

APPENDIX B

INITIAL CONDITION DEPENDENCY AND PERIODICITY ANALYSIS OF TWO TEST CASES

In order to study the effect of initial conditions, namely flapping motion kinematics, and periodicity of some test cases, mainly pure plunge cases, two test cases are chosen. Initial condition dependency analysis is carried out for purely pitching ($\alpha_a=45^o;\ k=2.5$) NACA0012 airfoil case by performing 2-D CFD simulations on the fine grid domain. To achieve the aim of this study, kinematics of the pure pitch motion are changed so that the motion is reversed by 180^o. In other words, the angular velocity is multiplied by minus one (-1). After that, the instantaneous vorticity contours and aerodynamic force coefficient variations of the original and reversed motion cases are compared and discussed.

For the periodicity analysis purely plunging ($x_a=0.02\ m;\ k=1.5$) NACA0012 airfoil case is chosen and again 2-D CFD simulations are performed on the fine grid domain. In order to achieve the aim of this study, the instantaneous vorticity contours and aerodynamic force coefficient variations obtained from the 5^{th}, 6^{th} and 7^{th} periods of motion are compared and discussed. It should be noted that a pure plunge motion case is chosen for periodicity analysis because a fully periodic motion could not be obtained for almost all pure plunge motion cases. 90^o oriented vertical motion of the airfoil towards the flow is thought to be one of the reasons causing this non-periodicity for pure plunge cases.

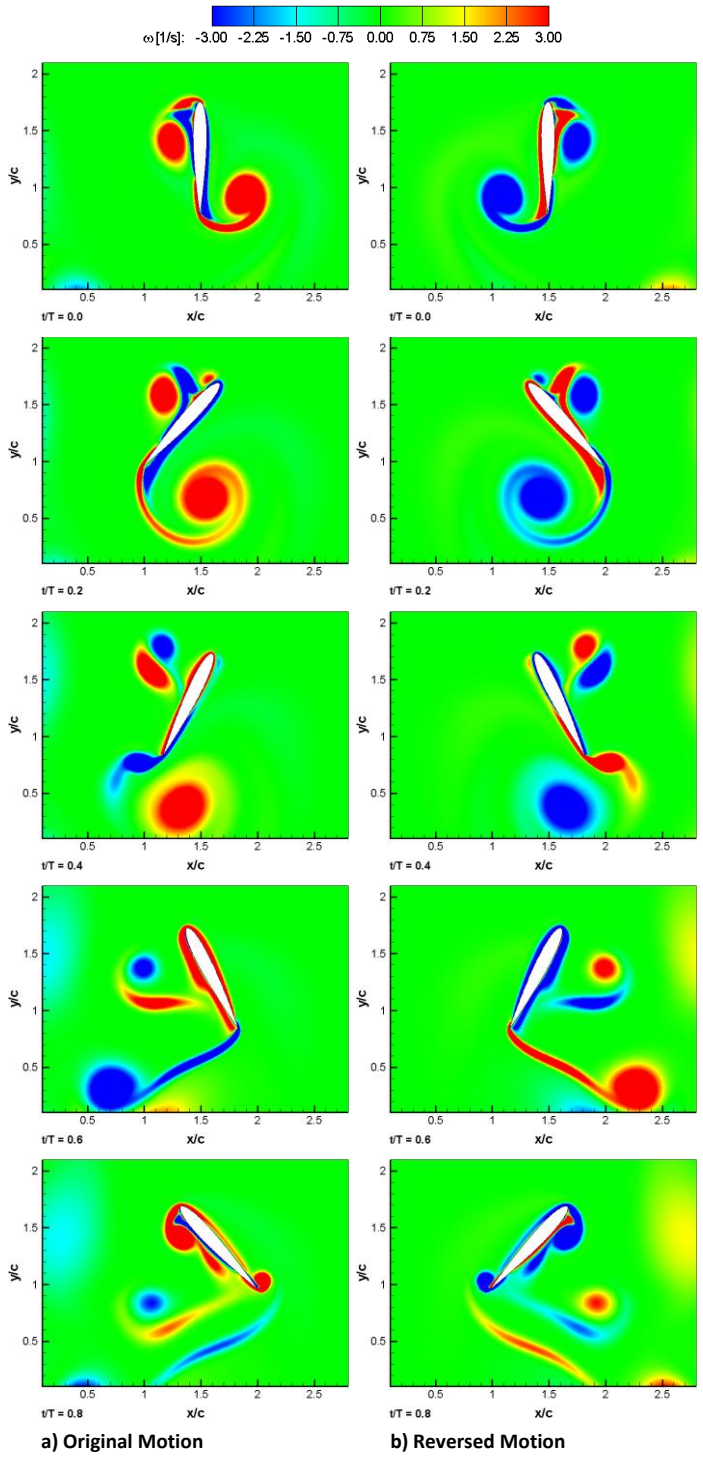

Figure B.1 Instantaneous vorticity contours obtained from 2-D CFD with fine grid simulations for purely pitching ($\alpha_a=45^o$; $k=2.5$) NACA0012 airfoil in terms of different motion kinematics.

Instantaneous vorticity contours obtained from the 2-D CFD simulations carried out on the fine grid domain for purely pitching ($\alpha_a=45^o$; $k=2.5$) NACA0012 airfoils in

terms of different motion kinematics are presented in Figure B.1. As it can be seen from this figure, changing the kinematics of the motion affects the vortices generated over the airfoil. Although the size and location of LEVs and TEVs with respect to the direction of the motion is not affected, their magnitudes changes sign. In other words, CCW rotating vortices becomes CW rotating and similarly CW rotating vortices becomes CCW rotating. The formation of the vortices around the airfoils undergoing original and reversed pure pitch motions can be said almost symmetrical. Hence, it can be concluded that the initial conditions applied affect the vortices around the airfoils by means of their magnitudes. Size and location of the vortices with respect to the direction of motion are affected slightly by the initial conditions.

Time histories of the aerodynamic force coefficients and the mean aerodynamic force coefficients obtained from the 2-D CFD simulations for purely pitching ($\alpha_a=45^o$; $k=2.5$) NACA0012 airfoils in terms of different motion kinematics are presented in Figure B.2 and Table B.1, respectively. Time histories of the aerodynamic force coefficients imply that lift coefficient histories of the airfoils undergoing original and reversed pure pitch motions are almost the same whereas drag coefficient histories are asymmetrical, i.e. drag coefficients of two studied cases have opposite signs at the same time instants.

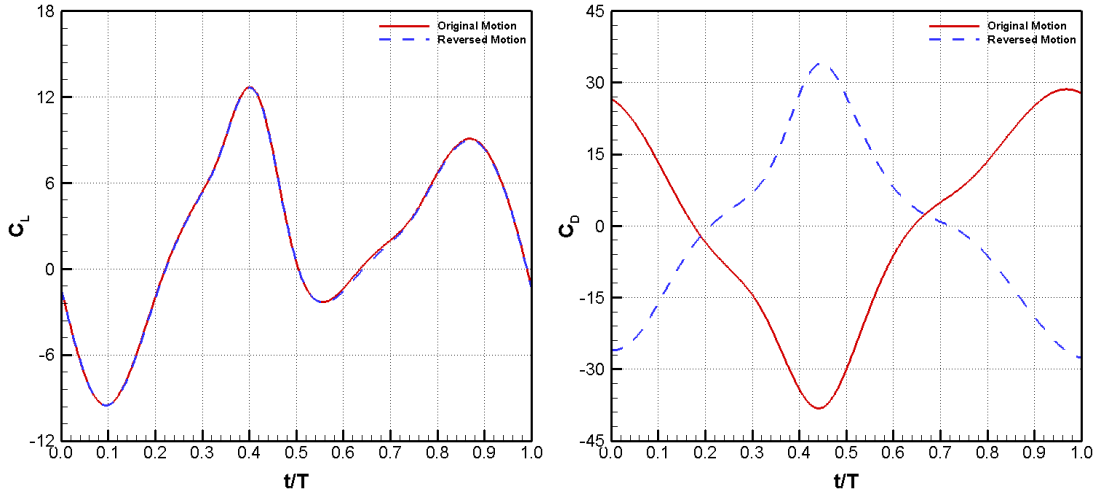

Figure B.2 Time histories of lift and drag coefficients obtained from 2-D CFD with fine grid simulations for purely pitching ($\alpha_a=45^o$; $k=2.5$) NACA0012 airfoil in terms of different motion kinematics.

The same phenomenon is also observed in the mean aerodynamic force coefficient comparisons. The mean lift coefficients of two cases are almost the same whereas a sign and magnitude difference exists in the mean drag coefficients. Hence, it can be concluded that the initial conditions applied affect the drag coefficient variations and as a result the mean drag coefficient. The lift coefficient variations, on the other hand, are affected slightly by the initial conditions.

Table B.1 The mean aerodynamic force coefficients obtained from 2-D CFD with fine grid simulations for purely pitching ($\alpha_a=45^o$; $k=2.5$) NACA0012 airfoil in terms of different motion kinematics.

	Original Motion	**Reversed Motion**
$\overline{C_L}$	2.1213	2.1096
$\overline{C_D}$	-0.1215	0.0942

Instantaneous vorticity contours obtained from the 2-D CFD simulations carried out on the fine grid domain for purely plunging ($x_a=0.02$ m; $k=1.5$) NACA0012 airfoil in terms of different periods of motion are presented in Figure B.3. As it can be seen from this figure, the size and location of the vortices generated over the airfoil differs from each other considering the different periods of the pure plunge motion investigated. These phenomena are signs of no-periodic motion. Since pure plunge motion case is a highly oscillatory flapping motion case, it is hard to obtain the periodicity. Due to the fact that pure plunge motions are not periodic at all, some discrepancies are observed in the instantaneous vorticity magnitude contours and aerodynamic force and moment coefficient variations.

Time histories of the aerodynamic force coefficients and the mean aerodynamic force coefficients obtained from the 2-D CFD simulations for purely plunging ($x_a=0.02$ m; $k=1.5$) NACA0012 airfoils in terms of different motion kinematics are presented in Figure B.4 and Table B.2, respectively. It is clear that lift coefficient and drag coefficient histories obtained from there different periods of the investigated pure plunge motion differs from each other too. The difference is bigger considering the

lift coefficient histories while there is a small difference between the drag coefficient histories of different periods of motion.

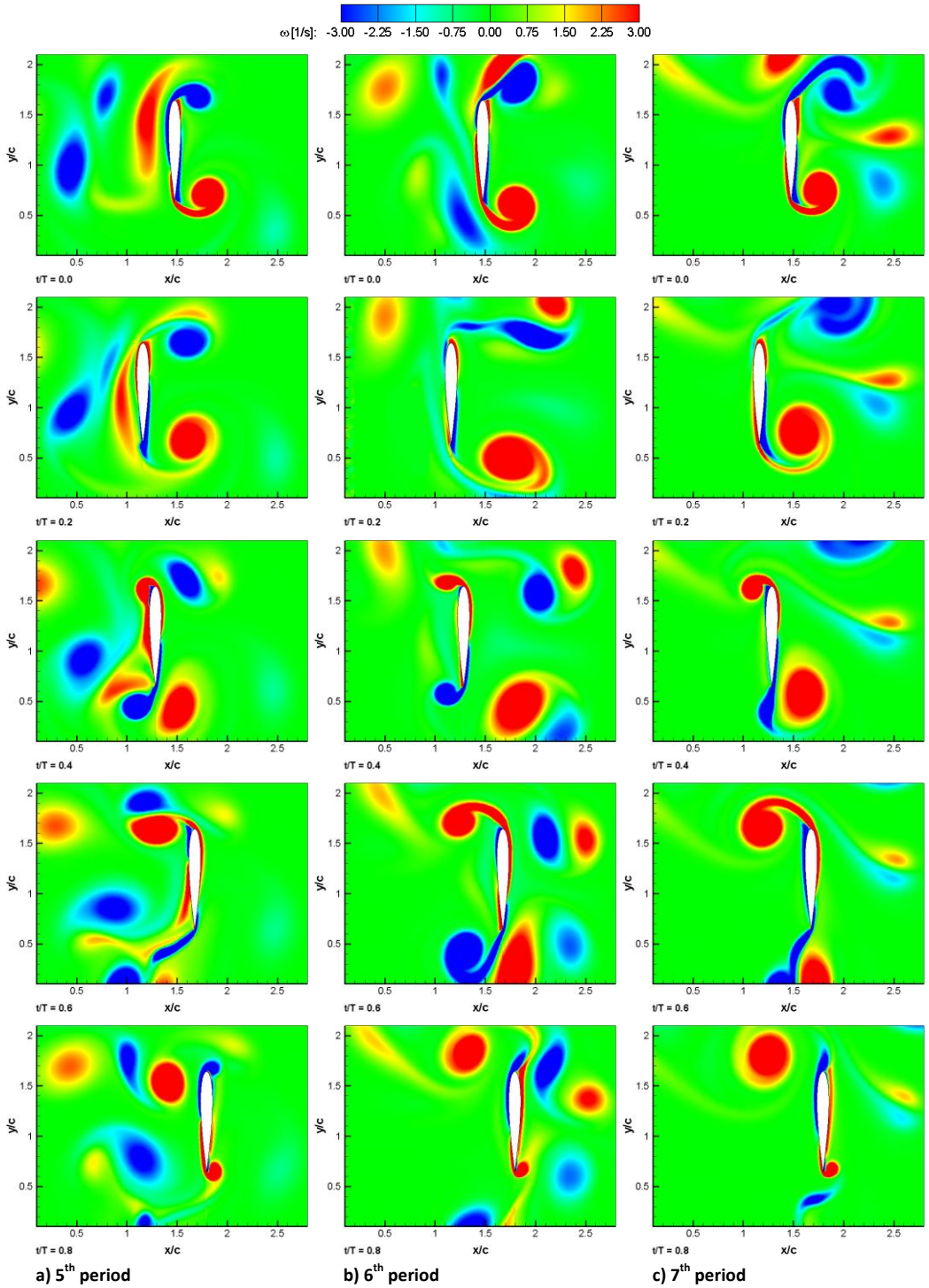

Figure B.3 Instantaneous vorticity contours obtained from 2-D CFD with fine grid simulations for purely plunging (x_a*=0.02 m; k=1.5*) NACA0012 airfoil in terms of different periods of motion.

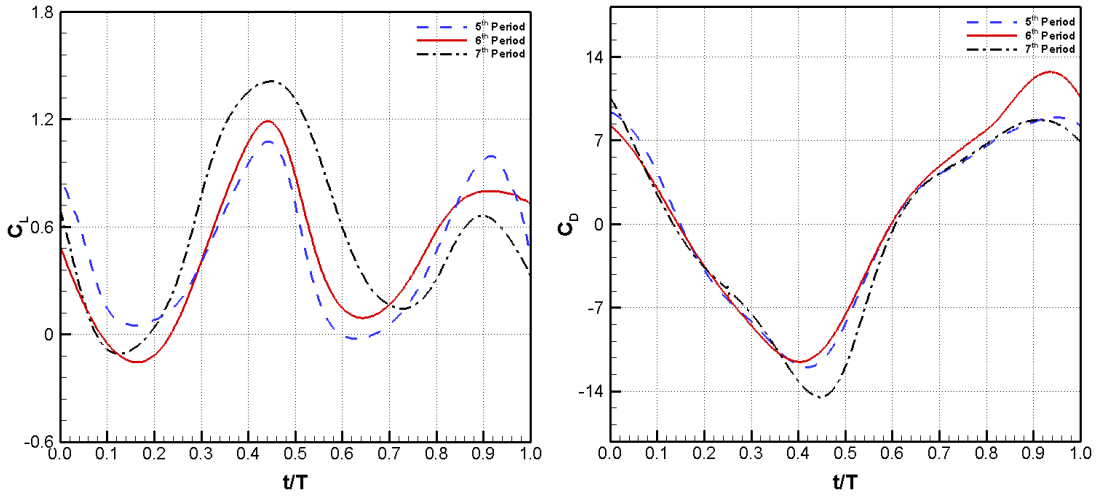

Figure B.4 Time histories of lift and drag coefficients obtained from 2-D CFD with fine grid simulations for purely plunging (x_a=*0.02 m; k=1.5*) NACA0012 airfoil in terms of different periods of motion.

The same phenomenon is also observed in the mean aerodynamic force coefficient comparisons. The mean lift and drag coefficients obtained from the three different periods of the motion differs from each other too. Again, the difference is bigger considering the mean lift coefficients whereas it is smaller considering the mean drag coefficients obtained from different periods of motion.

Table B.2 The mean aerodynamic force coefficients obtained from 2-D CFD with fine grid simulations for purely plunging (x_a=*0.02 m; k=1.5*) NACA0012 airfoil in terms of different periods of motion.

	Period of Motion		
	5th	6th	7th
$\overline{C_L}$	0.3470	0.4439	0.5583
$\overline{C_D}$	-0.0824	0.0364	0.0145

APPENDIX C

PHYSICAL CHARACTERISTICS OF THE TEST CASES

The reference velocity, Reynolds number (*Re*) and reduced frequency (*k*) values calculated for each investigated test case are given in Table C.3 below.

Table C.3 The reference velocity, Reynolds number (*Re*) and reduced frequency (*k*) values of the investigated cases.

Motion	**Amplitude**		**Ref. Velocity [m/s]**	***Re***	***k***
Pure Pitch	10°		0.001645	98	11.46
	30°		0.004935	295	3.82
	45°		0.007402	442	2.55
Pure Plunge	0.01 m		0.006283	375	3.00
	0.02 m		0.012566	751	1.50
	0.03 m		0.018850	1126	1.00
Combined Pitch-Plunge	10°	0.01 m	0.006495	388	2.90
		0.02 m	0.012674	757	1.49
	30°	0.01 m	0.007989	477	2.36
		0.02 m	0.013501	807	1.40
	45°	0.01 m	0.009709	580	1.94
		0.02 m	0.014584	872	1.29